



## **Effects of Light Absorber on Micro Stereolithography Parts**

*A Thesis Submitted to The University of Birmingham for the  
Degree of Doctor of Philosophy*

**By**  
**Mohamed Mohamed Zabti**

Master in Mechanical Engineering

School of Mechanical Engineering  
The University of Birmingham  
Edgbaston, Birmingham, B15 2TT

**June, 2012**

UNIVERSITY OF  
BIRMINGHAM

**University of Birmingham Research Archive**

**e-theses repository**

This unpublished thesis/dissertation is copyright of the author and/or third parties. The intellectual property rights of the author or third parties in respect of this work are as defined by The Copyright Designs and Patents Act 1988 or as modified by any successor legislation.

Any use made of information contained in this thesis/dissertation must be in accordance with that legislation and must be properly acknowledged. Further distribution or reproduction in any format is prohibited without the permission of the copyright holder.

## DEDICATION

*To the souls of my father*

*To my mother,*

*To my beloved wife and beautiful daughter,*

*To my sons, brothers and sisters,*

*I dedicate this thesis...*

*With*

*Love and Respect*

## ABSTRACT

Recent research has shown that Tinuvin®327 when used as a light absorber significantly reduces cure depth in micro stereolithography processes. However, so far, there has been no detailed study of the consequence of such effects on the accuracy and mechanical properties of fabricated parts. This thesis reports the results of an investigation of the effects of adding Tinuvin®327 to PIC-100 acrylate resin on such important parameters as cure depth, critical energy, part density, dimension accuracy and surface quality.

Initially, an experimental investigation was carried out to characterise the cure depth of resin after the addition of Tinuvin®327 in five different concentrations using a white light microscope. The investigation has shown that increasing Tinuvin®327 concentration reduces cure depth thickness and increases critical energy; it also found that increasing Tinuvin®327 concentration increased the density of the fabricated parts but significantly reduced the tensile strength.

In an attempt to compensate for adverse effects of Tinuvin®327 on tensile strength, the exposure time was increased. Results show that increasing the exposure time could compensate for the loss of mechanical strength.

The influence of different concentrations of Tinuvin®327 in PIC-100 acrylate resin on the accuracy of the fabricated parts was investigated in terms of linear dimensions, form and position. A benchmark test piece was designed and produced with different Tinuvin®327 concentrations and it was shown that increasing the proportion of Tinuvin®327 from 0.1% to 1% (w/w) caused a significant increase in dimensional errors due to the increased shrinkage associated with adding Tinuvin® 327 to resin.

The accuracy of Jacobs' cure depth model in predicting cure depth after the addition of Tinuvin®327 was investigated by comparing measured cure depth and predicted results using Jacobs' model. The simulated results did not match the experimental observations. The results show that Jacobs' model does not keep pace with the changes that occur in the PIC-100 photo polymerisation process with changes in material characteristics due to the addition of Tinuvin®327. Jacobs' cure model was adapted using two empirically derived constants to accurately predict the cure depth with 1% Tinuvin®327 concentration and an irradiation level of 750 mW/dm<sup>2</sup>.

Finally, in an attempt to simultaneously optimise exposure time to minimise cure depth and surface roughness and maximise mechanical strength, a parametric optimisation process was performed using the multi objective optimisation function of Matlab 2010. For 1% Tinuvin®327 concentration and an irradiation level of 750mW/dm<sup>2</sup>, the optimum exposure time was found to be 10 seconds.

## ACKNOWLEDGEMENTS

First, I would like to give thanks to **Allah** (My Lord) the almighty, the all great without whom I could not have completed this educational endeavour. I wish to express my sincere thanks to Cardiff University, especially the Manufacturing Engineering Centre (MEC) for the use of the facilities to pursue this research. I would like to extend special thanks and gratitude to my supervisor Professor D. T. Pham. Thanks for all the inspiring and wonderful discussions, encouragement and patience he provided throughout my stay at Cardiff University and Birmingham University. In addition, I would like to express my gratitude to Dr A Alkaseer. I am deeply grateful to him for his consistent encouragement, invaluable guidance and strong support during the course of this study. Also, I am highly indebted to Dr. Minev. I must appreciate his ever-ready helping attitude, However, the support provided by my senior colleagues Mr Minev, Dr Ji, Mr Parich from the MEC is more than appreciated. I am also very grateful to all the members of the Manufacturing Engineering Centre for their friendship and help. Grateful acknowledgement of my funding and support must be made to my home country Libya and the Libyan Ministry of Higher Education. Thanks are also due to all the members of staff of the Advanced Centre of technology Tripoli-Libya, who taught me and gave me the scientific base to continue my postgraduate studies. Special thanks go to Dr Mohamed Ateeg, Dr Housin Mesmary from Advanced Centre of technology for their support during my former study. My most sincere gratitude and appreciation go to my dear wife Mrs S. H. Toriki for her patience, continuous encouragement and support over the past difficult years. Thanks as well to Allah for his gifts; my beloved children “Malak”, “Abdulaziz”, and “Abdulmlik” I am deeply indebted to my parents and all the members of my family who gave me continuous support and encouragement throughout my life.

# TABLE OF CONTENTS

Abstract.....	I
Acknowledgements.....	II
Declaration.....	III
Contents.....	IV
List of Tables.....	IX
List of figures.....	X
Nomenclature.....	XV
<b>Chapter 1</b> Introduction.....	1
1.1 Background and Motivation.....	1
1.2 Research Hypothesis and Objectives.....	4
1.3 Thesis Organisation.....	5
<b>Chapter 2</b> Overview of Rapid Prototyping.....	7
2.1 Classification of Rapid Prototyping.....	7
2.1.1 Solid-based Rapid Prototyping.....	10
2.1.1.1 Fused Deposition Modelling (FDM).....	10
2.1.1.2 Laminated Object Manufacturing (LOM).....	11
2.1.2 Powder based Rapid Prototyping.....	13
2.1.2.1 Selective Laser sintering.....	13
2.1.2.2 3D Printing.....	15
2.1.3 Liquid based Prototyping.....	17
2.1.3.1 Stereolithography Apparatus (SLA).....	17

2.1.3.2 Micro stereolithography ( $\mu$ SLA).....	18
2.1.3.2 The Perfactory® .....	18
2.2 SLA Fundamentals.....	21
2.2.1 UV Exposure Energy and cure Depth.....	21
2.2.1.1 Penetration Depth, Critical Exposure and Cure Depth.....	22
2.2.1.2 Laser Exposure.....	22
2.2.2 Chemistry of photopolymers. ....	26
2.2.2.1 Properties of polymers.....	26
2.2.2.2 Cross-linking .....	28
2.2.2.3. Green strength.....	28
2.3 Light absorber and Stabilisers.....	29
2.3.1 Ultraviolet absorbers (UVA).....	29
2.3.2 Hindered amine light stabilisers (HALS).....	30
2.4. Related Research Work.....	31
2.4.1 Photocurable Resin.....	31
2.4.2 Cure Depth Model .....	38
2.4.3. Final Part Accuracy.....	44
2.4 Summary.....	48
<b>Chapter 3</b> Investigation of the influence of a light absorber on the mechanical properties of acrylate micro-stereo-lithography resin.....	49
3.1 Preliminaries.....	49
3.1.1 Definition of the problem.....	50

3.1.2 Critical energy and cure depth.....	51
3.2 Experimental work in defining and analysing the curing depth... ..	53
3.2.1 Materials.....	53
3.2.2 Tested Part Shape and Design.....	55
3.2.3 Fabrication of the U-shaped Part. ....	55
3.3 Results and discussion.....	57
3.3.1 Control of the Cure Depth.....	57
3.3.2 Determination of Critical Energy.....	60
3.3.3 Confirmation of obtained Critical Energy.....	62
3. 4 Experimental Investigation of Mechanical Properties.....	65
3.5 Effect of Tinuvin® 327 on Part Density.....	70
3.6 Enhancing the mechanical Strength.....	72
3.7 Summary.....	74
<b>Chapter 4</b> Effects of Light Absorber on Part Accuracy.....	75
<b>4.1</b> Preliminaries .....	75
4.1.1 Green Distortions.....	76
4.1.2 Cantilevers curl distortion.....	76
4.2 Experimental Work.....	78
4.2.1 Analysis of existing benchmarking parts.....	78
4.2.2 Objectives of Benchmarking. ....	78
4.2.3 Benchmark Design.....	79
4.2.3.1 Linear, Position and Geometric Dimensions Benchmark.....	79
4.2.3.2 Horizontal Slab Distortion test Part.....	83

4.2.3.3 Twin Cantilever Distortion test Part.....	83
4.2.4 Fabrication of The test part.....	83
4.2.5 Number of Specimens.....	85
4.2.6 Measurements.....	87
4.2.6.1 Measurement uncertainty.....	87
4.2.6.2 Linear dimension measurement.....	88
4.2.6.3 Measurement of Circularity Errors .....	90
4.2.6.4 Cantilever Curl distortion Measurement.....	90
4.2.6.5 Flatness Measurement.....	90
4.2.6.6 Surface Roughness Measurement.....	91
4.3 Results and Discussion.....	93
4.3.1 Linear Dimensions Error.....	93
4.3.2 Circularity and Position Error .....	96
4.3.3 Cantilever Curl Distortion.....	98
4.3.4 Horizontal Slab Distortion.....	100
4.3.5 Surface roughness.....	102
4.3.6 Test of Significant .....	102
4.4 Effect of Tinuvin® 327 on green Part Shrinkage.....	106
4.4.1 Shrinkage compensation factor and Christmas tree (SCF).....	106
4.4.2 Error and Measurement.....	108
4.4.3 Shrinkage Results.....	108
4.4.4 Shrinkage Compensation factor (SCF).....	112
4.5 Summary.....	115
<b>Chapter 5 Modified Cure model.....</b>	<b>116</b>

5.1 Preliminary .....	116
5.1.1 Jacobs Model.....	117
5.1.2 Limaye’s Model.....	117
5.2 Experimental Work.....	118
5.2.1 Light Intensity Measurement.....	119
5.2.2 Beam Intensity and Profile.....	119
5.3 Exposure time Model.....	121
5.3.1 Cure Depth Experiments.....	121
5.3.2 Adaptation of Cure Depth Model.....	125
5.4 Mechanical experiments.....	129
5.5 Surface Roughness Measurements.....	129
5.6 Results and Discussion.....	132
5.6.1 Mechanical Properties results.....	132
5.6.2 Surface roughness results.....	136
5.7 Optimisation.....	138
5.8 Summary .....	143
<b>Chapter 6 Conclusion.....</b>	<b>144</b>
6.1 Contributions.....	144
6.2 Conclusions.....	146
6.3 Future Work.....	150
<b>References.....</b>	<b>151</b>

## List of Tables

Table 3.1: $\mu$ SLA fabrication parameters.....	56
Table 3.2: Experimentally measured values of $E_c$ and $D_p$ .....	61
Table 3.3: Critical energy obtained from critical energy confirmations experiments.	64
Table 3.4: Results of measurements of tensile strength .....	69
Table 3.5: $\mu$ SL fabrication parameters.....	73
Table 4.1: Dimension Group.....	82
Table 4.2: Results of measurements uncertainty.....	89
Table 4.3: Results of two sample significant test for X, Y plane.....	105
Table 4.4: results of two sample significant test for Y, Z plane.....	105
Table 4.5: Results of shrinkage compensation.....	111
Table 5.1: Exposure time and corresponded cure depth used to calibrate the model.....	126
Table 5.2: Optimisation Boundary Conditions.....	140
Table 5.3: Results for 10s exposure time.....	141

## List of figures

Fig 2.1 Classifications of rapid prototyping according to material .....	9
Fig 2.2 The four types of .....	9
Fig 2.3 Fused Deposition Modelling .....	12
Fig 2.4 The laminated object manufacturing (LOM).....	12
Fig 2.5 SLS system Layout .....	16
Fig 2.6 The idea of 3D printing.....	16
Fig 2.7 The three layers of DMD .....	20
Fig 2.8 "on" or "off" in a digital signal .....	20
Fig 2.9 a)The Perfactory machine from EnvisionTEC .....	20
Fig 2.9 b) The Perfactory machine Layout.....	20
Fig 2.10 Stereo lithography system .....	24
Fig 2.11 The working curve .....	24
Fig 2.12 Laser profile shape .....	25
Fig 2.13 Effect of photo-initiator concentration on polymerisation rate .....	32
Fig 2.14 Effect UV light intensity on the polymerisation rate. ....	32
Fig 2.15 Effect of temperature on the polymerisation rate of TPG.....	32
Fig 2.16 a) cure depth and b) cure width vs Tinuvin Concentrations.. ....	35
Fig. 2.17 Successfully produced micro parts.....	35
Fig. 2.18 a) Irradiation map at the resin surface of arrow shaped bitmap.....	39
Fig 2.18 (-b) Irradiance 3D distribution at resin surface using the Limaye Model.....	39
Fig 2.19 Comparison of measured and predicted part heights .....	42
Fig 2.20 Comparison of measured and predicted part widths .....	42
Fig 2.21 Microscopic images of up-facing surfaces a) .....	47

Fig. 2.22 Discontinuous error resulted from the new approach.....	47
Fig 3.1 Cure Depth as a function of Exposure Energy.....	52
Fig 3.2 Tuivin® 327 absorption in Chloroform solution.....	54
Fig 3.3 Tinuvin 327 structure.....	54
Fig 3.4 Test Part Shape and Design.....	56
Fig 3.5 Test Part after fabrication .....	58
Fig 3.6 Cure depths for four different Tinuvin® 327 concentrations.....	58
Fig. 3.7 The effect of different Tinuvin®327 concentration on PIC-100.....	59
Fig 3.8 Shows position of glass slice on calibration plate.....	63
Fig 3.9 Gel spots for calculating the critical Energy.....	63
Fig 3.10 D 638-08 standard V type specimens.....	66
Fig 3.11 Testometric M500 machine.....	66
Fig 3.12 Stress strain curve for pure PIC-100 with different Tinuvin Concentrations.....	67
Fig 3.13 Influence of light absorber on part density.....	71
Fig 3.14 Stress strain curve for PIC-100 with 1% Tinuvin and different exposure time.....	73
Fig 4.1 Cantilever curl distortion Cf6.....	77
Fig 4.2 a: The Linear, Position and Geometric Dimensions Benchmark .....	81
Fig 4.2 b: Isometric view for the benchmark .....	81
Fig 4.3: The slab distortion test part .....	84
Fig 4.4: The twin cantilever test part shape and design.....	84
Fig 4.5: The error average for dimension accuracy.....	86
Fig 4.6 a: QuickVision® Coordinate Measuring Machine (CMM).....	89

Fig 4.6 b: Position of test part on QuickVision® (CMM) table.....	89
Fig 4.7 Circularity measurement.....	92
Fig 4.8 White light interferometer, Micro-XAM from Phase.....	92
Fig 4.9 The effect of Tinuvin®327 concentration on the linear.....	94
Fig 4.10 Comparison of the effect of Tinuvin®327 concentration on the linear dimensions.....	95
Fig 4.11 Results of Circularity measurement.....	97
Fig 4.12 Results of position measurement.....	97
Fig 4.13 Measured micro cylinders .....	97
Fig 4.14 Upwards curl of free end.....	99
Fig 4.15 Variation of the elevation $\Delta Z$ .....	99
Fig 4.16 Part flatness test .....	101
Fig 4.17 Flatness test results .....	101
Fig 4.18 Average surface roughness in X-Y Plane at 1% Tinuvin concentration.....	103
Fig 4.19 Average surface roughness in Y-Z Plane = 2.25 $\mu$ m at 0.0% Tinuvin concentration.....	104
Fig 4.20 Christmas Tree test part design .....	107
Fig 4.21 Christmas tree test part after fabrication .....	107
Fig 4.22 Effect of Tinuvin concentration on test part shrinkage in X direction .....	110
Fig4.23 Effect of Tinuvin concentration on test part shrinkage in Y direction .....	110
Fig 4.24 Results of shrinkage compensation factor in linear minensions.....	113
Fig 4.25 Results of shrinkage compensation factor in Circularity errors.....	114
Fig 4.26: Results for position errors after using SCF.....	114
Fig. 4.27: Test part built using Shrinkage Compensation Factor.....	114

Fig 5.1 M12 10-30VDC P86 photo sensor mounted on measuring slider .....	120
Fig 5.2 Beam Intensity and Profile.....	120
Fig 5.3 resin drops on the top of transparent glass.....	122
Fig 5.4 cured spots.....	122
Fig 5.5 average of six readings for each exposure time.....	124
Fig 5.6 comparison of results obtained by both experiments and simulation.....	124
Fig 5.7 values used to calibrate the model.....	126
Fig 5.8 the agreement between experimental and simulated results.....	128
Fig 5.9 downfacing feature test pare.....	131
Fig 5.10 stress strain curve for PIC-100 + 1% Tinuvin concentration with different exposure time.....	133
Fig 5.11 Young's modulus values vs exposure time for PIC-100 with 1% Tinuvin concentration.....	135
Fig 5.12 Surface roughness vs exposure time for PIC-100 with 1% Tinuvin concentration.....	137
Fig 5.13 Cure depth, Young's modulus and average surface roughness vs exposure time for PIC-100 with 1% Tinuvin concentration .....	140
Fig 5.14 Normalised graph to unify the ranges of all the three objectives for the optimisation process.....	141

## Nomenclature

$C$	photo initiator concentration
$C_d$	Cure depth
$Cf6$	Cantilever curl distortion factor
$CN$	light absorber concentration
$C_w$	Cure width
$DO2$	Oxygen diffusion coefficient
$D_p$	Depth of penetration
$D_{pL}$	Penetration depth of liquid resin
$D_{pS}$	Penetration depth of the cured layer
$E(z)$	Laser energy at z depth
$E_c$	Critical energy
$E_0$ or $E_{max}$	Laser energy at resin surface
$H$	Irradiance
$H(pri)$	Irradiance received by point $pri$ on the resin surface
$H_{av}$	Average irradiance across the resin surface
$H_0$	Irradiance at centre of laser beam
$I$	Photo initiator
$K_{toxy}$	Oxygen reaction rate
$LT$	Layer thickness
$M$	Monomer
$m^{H_2O}$	Weight of water that fills the empty pycnometer
$m^{H_2O}$	Weight of added water
$M0$	Supported base height is
$M6$	Length of the beam

$m_s$	Mass of the measured part
$n$	Number of measurements in the set
$P_L$	Laser power
$R$	Radicals
$Ra_{av}$	Average surface roughness
$R_a$	Surface roughness average
$R_q$	Root-mean-square surface roughness
$s$	Estimated standard deviation
$t$	Exposure time
$t_o$	Resin threshold time
$u$	standard uncertainty
$V_s$	Volume of solid part
$V$	Volume of water that fills the pycnometer
$v_s$	scan velocity
$V'_{H_2O}$	Volume of added water
$w_j$	weight equation for irradiance distribution
$y$	Young's modulus
$\rho_s$	Density of measured part
$w_o$	Laser beam radius
$\alpha\lambda$	Absorption coefficient of photo initiator
$\alpha\lambda N$	Absorption coefficient of light absorber
$\lambda$	Laser beam wavelength
$\rho_{H_2O}$	Temperature dependent value of water density
$\delta(\rho_j, vk, \rho_i)$	a function determines whether a ray from point $\rho_j$ in the direction vector $vk$ will strike an area centred on point $\rho_i$ on the resin.

# Chapter 1

## Introduction

### 1.1 Background and Motivation

Several terms are used to describe the technology which has created a revolution in the rapid production world; these include direct manufacturing, solid free-form production, and additive fabrication. Some authors consider rapid manufacturing (RM) as the collective term for all other rapid technologies developed in the last 20 years including rapid tooling (RT), and rapid prototyping (RP) (Pham *et al.*, 2003). However, rapid prototyping (RP) remains the most widespread term used to describe such technologies (Wohlers, 2008). A number of RP technologies are considered as being crucial in the design and/or development of parts, especially in the prototyping of micro parts and accurate parts. The idea behind RP is that any 3D model can be sliced into a set of separate 2D layers. The RP system then combines the layers to form one part. RP has slight or no technological constraints when compared to conventional technology. Almost any complex part can be fabricated in this way. This development could free designers from a number of manufacturing constraints, and encourage them to innovate more (Eyers *et al.*, 2010).

Stereolithography was the first RP system and is now the most developed of all RP technologies (Jacobs, 1993). 3D Systems introduced a stereolithography machine (SL) as the first commercial SFF (Solid Freeform Fabrication) system in 1988 (Chua, 2003; and Gebhardt, 2003). Stereolithography can produce accurate parts and is still widely used. The SL machine introduced by 3D Systems uses an optical system to focus ultraviolet laser beams onto a liquid resin surface and scans the relevant slice of the 3D model onto the top of the

resin surface, solidifying the scanned section of the surface to create a new part layer. SL systems could produce very accurate parts, when compared with other RP systems, but not to micrometer scale because the recoating system in SL systems could damage the micro-features.

In 1993, Ikuta *et al.* suggested an alternative micro stereolithography machine ( $\mu$ SL) system. The first  $\mu$ SLs were based on a line-scan method where a UV laser scanned the resin surface line by line, but in 1996 the first mask-based  $\mu$ SL system was developed by Nakamoto and Yamaguchi (Gebhardt, 2003). In this system the complete sliced layer is projected onto the resin surface instead of scanning line by line. There was a significant enhancement in resolution when Maruo *et al.* (1997) suggested the two-photon absorption method, where photo polymerisation is activated by focusing a near-Infra Red pulsed laser beam through an objective lens, and a 3D part is constructed by scanning the focused spot in three dimensions inside the resin (Maruo *et al.* 1997)

One year later, Bertsch *et al.* (1997) introduced the idea of using dynamic mask generators to project the required pattern onto the resin surface. First, they used a liquid crystal display (LCD) and then in 2001 proposed a digital micro-mirror device (DMD) (Bertsch *et al.*, 2001). Both the LCD and DMD are referred to as projection methods which are different from the vector scanning method. Many researchers have developed similar but more advanced and newer  $\mu$ SL techniques, and produced better-quality  $\mu$ SL systems for fabricating complex micro features (Bertsch *et al.*, 2003; Sun *et al.*, 2005).

To fabricate micro parts with  $\mu$ SLs, the 3D model has first to be sliced into several layers by the design software and saved as a STL (Standard Tessellation Language) file. To accurately fabricate the desired design, the cure depth  $Cd$ , the depth to which a 3-dimensional network is formed during polymerisation, must be exactly the same thickness as the sliced layer (Bertsch

*et al.*, 2004). In  $\mu$ SL systems, the layer thickness to be solidified is restricted by the depth of resin between the vat surface and the previous cured layer (Sun *et al.*, 2005). Any excess of radiation will increase the curing of the previous layer. However, if the part is designed to contain an overhang or bridge, the radiation penetrating into the resin vat will be such as to cause an increase of thickness of the overhanging layer which is determined by the vertical resolution. Thus, the vertical resolution has a substantial impact on the ability of  $\mu$ SLs to produce 3D microstructures and could mean undesired microstructures being ‘fabricated’ if the cure depth is greater than the slicing thickness. Thus, geometric and dimensional accuracy will be influenced by any over penetration.

To successfully fabricate 3D microstructures with down-facing surfaces, the cure depth must be precisely controlled by adjusting the curing characteristics to accurately fabricate and bond thin slices together. Several previous studies have attempted to reduce cure depth in  $\mu$ SLs, giving more precise part detail, using light absorption or polymerisation inhibition (Choi *et al.*, 2009). Zissi *et al.* (1996) theoretically derived the cure depth and cure width in proportion to light absorption percentage, and showed both theoretically and experimentally that cure width and depth could be reduced using a light absorber and these effects were presented as a function of the concentration of light absorber in solution. Choi *et al.*, (2009) used Tinuvin® 327 as a light absorber to control cure depth in an attempt to improve accuracy of fabrication of 3D parts with down-facing surfaces. Other researchers have performed similar work since Zissi *et al.*, (1996), for example, Choi. *et al.*, (2007), Choi *et al.*, (2009), but fundamental questions remain to be answered in order to successfully fabricate complex 3D micro structures with considerable feature detail and part overhangs. These questions include: What could be the effects on the mechanical properties of the part due to using light absorber? What is the effect on part accuracy of including light absorber in the polymer?

The aim of this research was to determine the effect of Tinuvin®327 on resin properties, mechanical properties and part accuracy. The research was to include an experimental investigation into the effects of different concentrations of Tinuvin®327 light absorber on mechanical properties (tensile strength and Young's modulus) of parts, accuracy of the parts produced (including surface roughness), critical energy (the irradiation energy at which the cure depth of the material is zero) and cure depth. The motivation for this work was the enormous improvement in production methods that could result from a better knowledge of the effects of the light absorber on the characteristics of the resin and thus on the production process and the properties of the final product.

## **1.2 Research Hypothesis and Objectives**

The hypothesis for this research is that, in micro stereolithography, the addition of light absorber has a significant influence on the resin properties and thus plays an important role in the mechanical properties, accuracy and surface roughness of the produced part. In this context, as mentioned above, the overall aim was to obtain a deeper understanding of the influence of the light absorber Tinuvin®327 on mechanical properties, accuracy and surface roughness when a micro part is fabricated, and thus to optimise the exposure time. To achieve the overall aim of the research, the following objectives were set:

1. To investigate experimentally the influence of Tinuvin®327 on cure depth in PIC-100 acrylate resin in order to address the relationship between cure depth and Tinuvin®327 concentration.
2. To investigate the effects of Tinuvin®327 concentration on part density.
3. To calibrate and validate Jacobs' cure depth model that considers the effect of Tinuvin®327 on exposure time and cure depth.

4 To study experimentally the influence of Tinuvin®327 on part accuracy in PIC-100 acrylate resin in order to address the relationship between part shrinkage and Tinuvin®327 concentration.

5 To conduct an optimisation process with the goal of improving the mechanical properties and reducing surface roughness.

### **1.3 Thesis Organisation**

The remainder of the thesis is organised as follows:

**Chapter 2** reviews the classification of SL processes and describes the fundamentals of stereolithography systems that are commercially available and finally discusses related research work.

**Chapter 3** investigates the effect of Tinuvin®327 concentration on mechanical properties in  $\mu$ SL in terms of tensile strength. First, a brief review of cure depth related research with respect to cure depth and critical energy is introduced. Then, the effect of Tinuvin®327 as a light absorber on cure depth reduction in PIC-100 acrylate resin is investigated. The effect of Tinuvin®327 concentration on mechanical properties and part density is next discussed. Finally, an investigation of enhancement of mechanical properties via exposure energy is carried out.

**Chapter 4** investigates the effect of Tinuvin®327 concentration on part accuracy in  $\mu$ SL. A benchmark part designed to evaluate the effect of Tinuvin®327 on linear position, and geometric dimensions is described. The results of horizontal slab and twin cantilever distortion tests to study the effect of Tinuvin®327 on part distortion are presented. Next, the effect of Tinuvin®327 concentration on surface roughness is discussed. Finally, the effect of

Tinuvin®327 concentration on green state (before post curing) shrinkage is presented and a new shrinkage compensation factor is introduced.

**Chapter 5** describes an experimental approach to calibrate Jacobs' cure depth model to predict the cured thickness for down facing and hanging features. First, Jacobs' and Limaye's models are briefly discussed. Then experimental work conducted to measure the light intensity for use in the model calibration. After that an exposure time model derived from Jacobs' model is used to study the relationship between exposure time and cure depth, then a comparison between results of cure depth obtained from simulation of Jacobs' model and experimental results is given. Next, a calibration method to calibrate Jacobs' model is described. The results of surface roughness experiments to study the effect of exposure time on surface roughness after the addition of Tinuvin®327 are provided. Finally, an optimisation process is discussed that was conducted to obtain the exposure time for the best mechanical properties, cure depth, and surface roughness.

**Chapter 6** summarises the contributions and conclusions of the thesis and proposes possible directions for further research.

## Chapter 2

### Overview of Rapid Prototyping

This chapter reviews the different types of RP with the intention of classifying the RP techniques. The first section commences with a classification of the RP technologies, this is followed by the history of stereolithography and how it works. Next stereolithography fundamentals are discussed and finally relevant research work is presented.

#### 2.1 Classification of Rapid Prototyping

There are various classifications of RP processes using such features as material, cost, speed and size, though up to now there is no agreed classification system (Grimm 2004). Kruth, (1991) has classified RP processes according to material addition or material removal (whether the process is adding material to build the part or removing material from an existing raw material). Material addition processes may be characterised according to the state of the building material before part formation, see Fig (2.1). In general, Chua *et al.*, (2003), classified RP into four categories as shown in Fig 2.2. The four categories of RP according to Chua *et al.*, (2003) are:

**Input;** The term *input* comes from the electronic data required to describe the 3D model to the machine. Two potential methods are possible to feed the data in to the machine, the 3D computer model created by a CAD system or a physical solid part through Coordinate Measurement Machine (CMM).

**Method;** According to the working method classification RP can be classified to following categories: cutting and gluing, melting and solidifying, joining or building and Photocuring.

Furthermore, Photocuring divided into single laser beam, double laser beam, and mask projection method.

***Materials:*** the RP can be classified according to form of material used to build the part, solid, liquid or powder state. These three states will be further divided according to material used, such as resins, paper, wax and ceramics.

***Applications:*** RP can also be classified according to usage. There are a variety of applications where RP can be used, and according to the application RP can be classified into; design, engineering analysis and planning, manufacturing and tooling.

In general, the most widespread classification for RP is by the form of the material used to build the part.

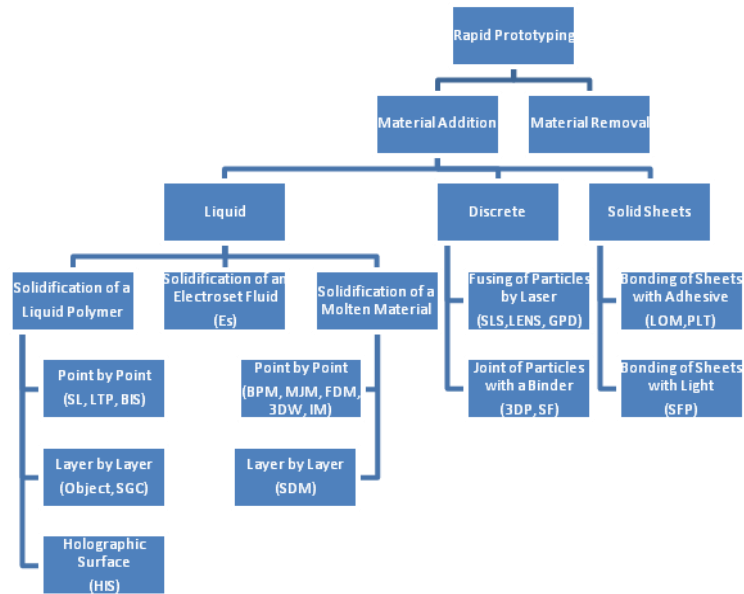


Fig. 2.1 Classification of RP according to material addition or removal (Kruth, 1991)

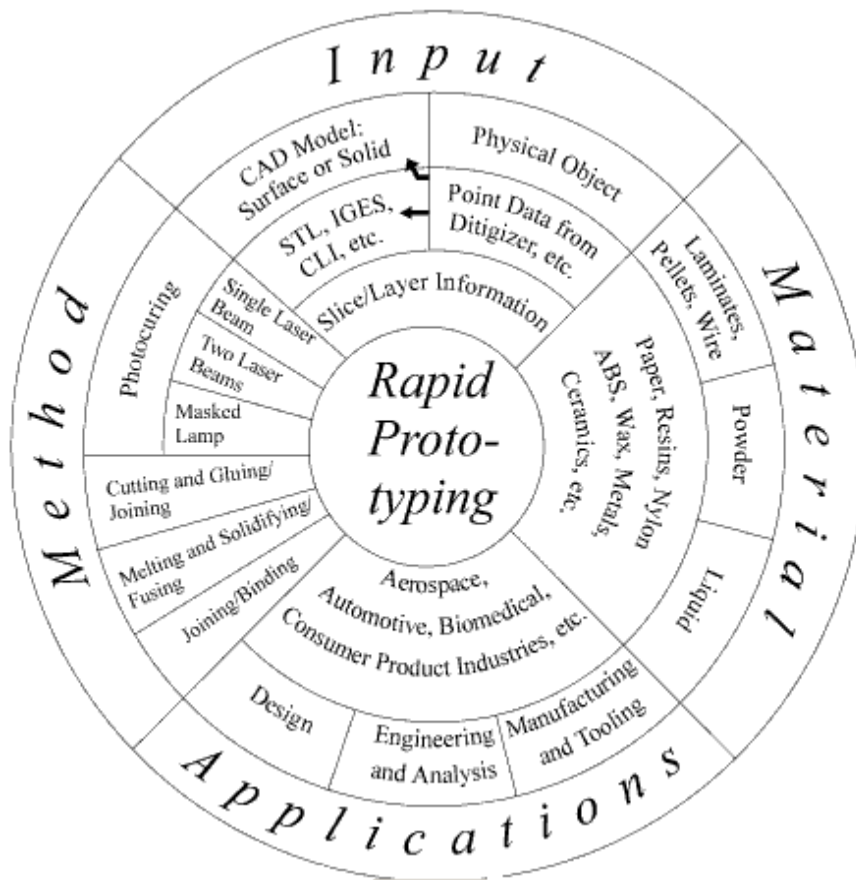


Fig. 2.2 The four types of RP classifications according to Chua *et al.*, (2003)

### **2.1.1 Solid-based Rapid Prototyping**

The common feature in these systems is that solids are used as the primary material to produce prototypes.

#### **2.1.1.1 Fused Deposition Modelling**

In Fused Deposition Modelling (FDM), see Fig 2.3, the thermoplastic material is pressed by a piston throughout a syringe with a nozzle onto a base-plate. FDM machines build each layer by drawing the cross-section of the shape with the nozzle while extruding the molten thermoplastic for that layer. The polymer solidifies on contact with the base-plate, then the base-plate is moved downward by the thickness of one layer and another layer is added. In this way the 3D part is build layer by layer. The first FDM machine was manufactured by Stratasys® Inc in 1992. There are now eight FDM systems on the market which range from small work volumes or envelopes of 203mm x 203mm x 305mm, to the largest work volume of 600mm x 500mm x 600mm (Stratasys 2011).

Two types of building materials are used in FDM, one is for the 3D part, and the other is for support. The support material acts as a scaffolding structure, allowing thermoplastic material to build up over it. These supports are necessary in case of parts with overhanging features. The different chemical properties of support materials and building materials prevent them bonding to each other; consequently, the separation of the part from the support material is relatively easy. One of the big advantages of FDM is the use of water-soluble supports which makes separation of supports from parts easier and reduces the time of post processing.

The layer thicknesses in FDM ranges from 0.178mm (0.007 inches) to 0.356mm (0.014 inches), and the width of the extruded material varies between 0.25mm (0.010 inches) to 0.965mm (0.038 inches) (Chua *et al.*, 2003). In addition to thermoplastic materials, wax can

also be used for investment casting models. FDM system is environment friendly, and since it does not use toxic materials it is capable of operating in an office environment. Once the supports are removed, the parts are ready to use. However, FDM systems have some disadvantages including slow processing, restricted accuracy and unpredictable shrinkage because each layer is dependent on the amount of solid area previously filled by build material. Also the nozzle size restricts the accuracy, excluding manufacture of small part or parts with detailed features.

### **2.1.1.2 Laminated Object Manufacturing**

Laminated Object Manufacturing (LOM) is one of the solid-based RP techniques, where a 3D part is built layer by layer using a roll of paper as the building material see Fig. 2.4 (Wang and Yan, 1993). In LOM the building process begins with the lamination of the disposable base. This disposable base consists of 20 layers of paper crosshatched. The paper is coated with a thermally activated adhesive on the back, the lamination process is completed using a heated stainless steel roller. The roller pressure releases any trapped air bubbles and brings the new layer into intimate contact with the previous layer to ensure bonding. After bonding, every layer is cut by a CO<sub>2</sub> laser beam as determined by the STL file. The excess material surrounding the part is cut by the laser in a cross-hatch pattern to facilitate the removal of unwanted material after part is finished, it and also to act as a support for subsequent layers, see Fig. 2.4. The sequence repeats itself until the final layer is completed. Once the part is complete, the build platform is moved up and the part freed. At the end of the process, the excess material, which was previously cross-hatched, is removed by hand (Chartoff *et al.*, 1996). LOM is widely used for RT and RM. LOM is capable of producing patterns and prototypes for sand casting, injection mould cavities, investment casting and thermal form tools (Park *et al.*, 2000).

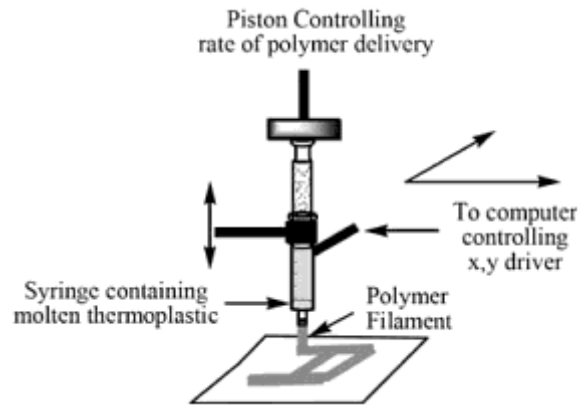
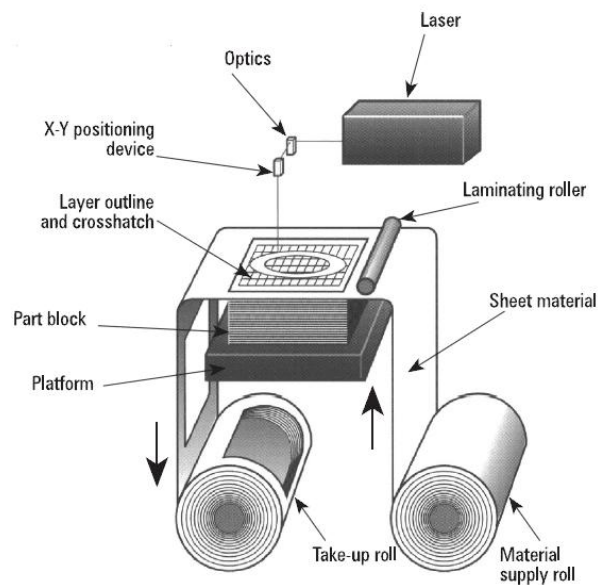


Fig. 2.3 Schematic of Fused Deposition Modelling



Source: Helisys Inc. (nd)

Fig. 2.4 Laminated Object Manufacturing

LOM has several advantages, including reduced product development cost, the variety of low-cost materials that can be used such as paper and plastic sheets, part size (the maximum part size of 813mm x 559mm x 508mm high), the dimensional accuracy of the part due to the positioning system accuracy of  $\pm 0.127$ mm in the X and Y-axes and virtually no internal stresses (Zyzalo, 2008).

Compared to other RP technologies, LOM has a fast build time because the laser does not scan the whole cross-section of a layer. It only cuts the boundary of the cross-sectional shape and crosshatches the outer area. On other hand LOM is inappropriate for thin walled parts because of the weakness of the part in the Z-axis to withstand post processing, so when removing supports, one must be aware of the delicate features of the part. Another disadvantage of LOM is that parts are not suitable for dynamic functional testing. Parts are usually layered with urethane, silicon or epoxy spray to prevent the absorption of water vapour (humidity) and this leads to expansion in part size and warping.

### **2.1.2 Powder Based Rapid Prototyping**

The common features in this type of systems that all raw materials used to produce prototypes are in powder condition, regardless whether the part made of plastic as in Selective Laser Sintering or starch as in 3D Printing.

#### **2.1.2.1 Selective Laser Sintering**

Selective Laser Sintering (SLS) is a powder-based RP developed by the DTM Corporation established in 1987 at the University of Texas. The first commercial SLS systems were presented in 1992 (Wan, 2007). Since then there have been continual improvements in part accuracy, production time, surface finish and fine resolution. With SLS, the building process

begins when the roller spreads a layer of powder, supplied by reservoirs on both sides of the machine, over the powder bed to the desired thickness; see Fig. 2.5 (Azari and Nikzad, 2009). Then an infrared heat-generating CO<sub>2</sub> laser scans the cross-section of the part. When the laser beam hits the powder surface, the temperature is raised to the melting point and the powder particles sinter together and form a solid mass. Succeeding layers also bond with previous layers in the same way. After the cross-section has been scanned, the powder bed is moved downward by the amount of one layer thickness and the process repeats until the part is completed.

Two SLS systems are supplied by 3D Systems: sHiQ and the sPro series (sPro60, sPro140 and sPro230). The sPro series claim to have the largest part size for SLS technology. With sPro230 the parts size could be up to 550mm x 550mm x 750mm high. Yet the sPro series is designed to produce only plastic parts. The HiQ can use a range of materials such as; thermoplastics, composites, metals and ceramics. Two layer thicknesses are available for either system; 0.1mm or 0.15mm. The resolution in XY plane is restricted by the laser beam diameter; the HiQ system uses a 0.4mm CO<sub>2</sub> laser beam and the sPro system uses a 0.5mm CO<sub>2</sub> laser beam (3D Systems, 2012).

SLS has two key advantages; firstly it can work with a wide range of materials, secondly no supports are required since the un-sintered powder acts as a support to the part. There are two disadvantages of SLS systems, high power consumption due to the high wattage laser used and it is the most expensive RP system. Nevertheless, SLS parts have high dimensional stability and a good surface finish which can be improved by sand blasting, if necessary. Generally post-curing of parts is not required, nevertheless, to improve the mechanical properties of a part it can be dipped in another material.

### 2.1.2.2 3D Printing

3D printing was developed at the Massachusetts Institute of Technology (MIT) in the mid-1990s and subsequently licensed to companies. 3D printing uses inkjet technology to build the cross-sectional slices of the part, layer by layer until the part is finished. The process begins by spreading a thin layer of starch powder on the substrate as shown in Fig. 2.6. The inkjet head injects droplets of adhesive liquid with diameter between 50  $\mu\text{m}$  to 100 $\mu\text{m}$  into the relevant region of the slice to act as glue binding the starch powder together. Next the substrate is moved downwards a distance corresponding to the thickness of one layer, then the process is repeated (Gebhardt, 2000; Stopp, 2008). In the Z-Corp Spectrum Z510, for instance, the layer thickness can range from 0.089mm to 0.203mm and the part can be any size up to a maximum of 254mm x 356mm x 203mm high. The Z510 uses four print heads to provide an XY resolution of 600 x 540 dpi (Z Corporation, 2012). Starch and plaster are the most widely used materials so the parts produced are neither strong nor long-lasting and are not suitable for functional use which is a big disadvantage. However, parts can be strengthened by dipping them in wax or epoxy.

There remain several advantages to 3D printing the most important is the speed compared with other RP technologies. This is achieved by using multi-heads which cover a wide area of the layer. Another advantage is that multi coloured parts can be easily produced. Finally, the capital cost of a 3D printer machine is not high and they are cheap to run and maintain (Wohlers, 2005).

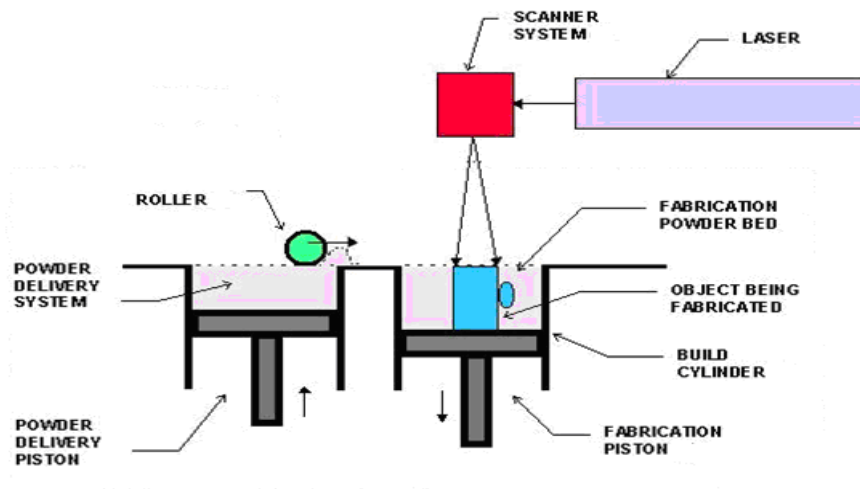


Fig. 2.5 Schematic of SLS system layout

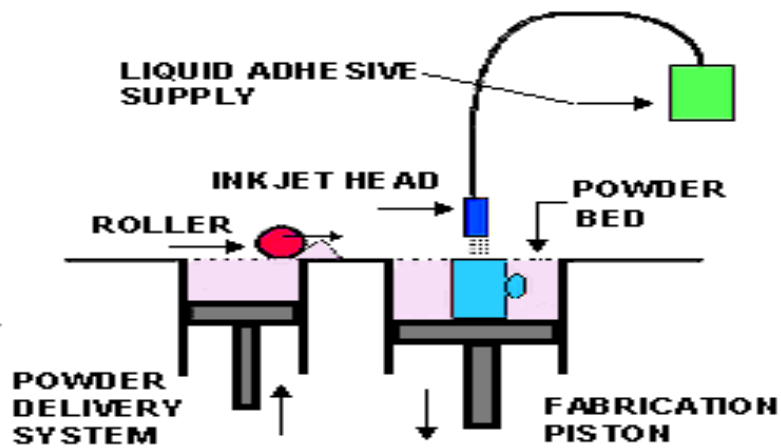


Fig. 2.6 The concept of 3D printing

### **2.1.3 Liquid Based Prototyping**

The common features in this type of systems that all raw materials used to produce prototypes are in liquid condition.

#### **2.1.3.1 Stereolithography**

Stereolithography is the RP technology most widely used in industry and technology to directly manufacture 3D models (Yang *et al.*, 2008). The process begins with the design of a 3D CAD model of the required part, followed by slicing of the 3D CAD model into very thin planes that which are the X-Y cross-sections of the 3D model. All the cross-sections are then saved as an STL build file and sent to the machine. The STL file is used to control the movement of an ultraviolet (UV) light scanner in X-Y directions and the substrate in the Z direction. The build material is a photocurable resin which is polymerised when hit by the UV light. The 3D model is then scanned onto the resin surface, layer by layer, until the complete part has been defined (Yang *et al.*, 2008). The basic elements of a SL system are; computer control and software, laser source, scanning system, recoater and elevator.

The machine computer and the controlling software are used to control the movement of the mirrors which reflect the laser beam onto the resin surface. The computer also directs the movement of recoater and elevator. The laser system consists of the laser source and the “beam shaping” optics which condition and focus the laser beam onto the resin surface to the required spot. The scanning system consists of a set of mirrors controlled by the STL file, which direct the laser beam so that the required cross-section is scanned. After the first layer is scanned, the elevator moves downward by the thickness of one layer. The recoater then pushes a fresh layer of resin onto the top of the previously cured layer. The next layer is then scanned and the process is repeated until the part is finished.

### **2.1.3.2 Micro stereolithography**

The principle behind of micro stereolithography ( $\mu$ SL) is the same as for stereolithography; nevertheless, the resolution of  $\mu$ SL is much higher. Again using UV light, two main exposure systems have been successfully used in  $\mu$ SL; scanning  $\mu$ SL and mask projection  $\mu$ SL systems, or integral  $\mu$ SL systems. It is assumed that, in conventional SL several optical elements are moving at the same time which often leads to focusing errors and low resolution. Additionally, the laser beam cross-section doesn't remain regular during the scanning process. Consequently, the X-Y resolution will be affected by the distance of the feature from the centre of the vat. These negative aspects can be eliminated by fixing the light beam and scanning the layer by moving the substrate under the UV spot.

The major drawback of conventional  $\mu$ SL is the limit on minimum layer thickness (several microns) due to viscous and surface tension effects. This problem was solved by the two-photon  $\mu$ SL process suggested by Maruo *et al.*, (1997), and this method has successfully enhanced fabrication resolution. In two-photon  $\mu$ SL process, the material does not need to be layered and micro and even nano features can be fabricated precisely (Wu *et al.*, 2006; Varadan, 2003).

### **2.1.3.3 The Perfactory® System**

The Perfactory® system from EnvisionTEC is the only system that builds parts upside down and gradually peels the part out of the vat. The Perfactory system uses a 250W UHP (ultra high pressure) lamp as its UV source to solidify the resin by projecting the UV light through a window underneath the resin vat (Perfactory, 2008). The base of the vat is coated with a silicon layer to prevent polymerised resin from sticking to the vat which is considered as a

disposable item. The lamp life is almost 500 hours, and the focus and light intensity have to be recalibrated before starting any process. The Perfactory system uses a DMD to reflect the UV light onto the resin surface. The DMD originated in entertainment media technology as digital light processing (DLP) using a 2D array of micromechanical mirrors developed by Texas Instruments in the 1980s. Then, in 1987, this concept was extended to the DMD by Texas Instruments (Texas Instruments Inc., 2005). The first  $\mu$ SL to use DMD was developed in 2001 by Bertsch (3D micro complex). Depending on the chip size, the DMD has from 800 to more than 1 million micro mirrors on it. Each single micro mirror is connected to support hinges and electrodes. The mirror size is  $13.7\mu\text{m} \times 13.7\mu\text{m}$  and consists of three layers separated by two gaps as shown in Fig. 2.7. The gap separating the three layers allows the mirror to tilt  $\pm 10^\circ$ . The two address electrodes connected to the SRAM are positioned diagonally opposite each other. Between them are the two torsion hinges connected to the yoke. As an electric current is applied to either of the address electrodes, the mirrors can tilt  $\pm 10^\circ$ , representing "on" or "off" in a digital signal Fig. 2.8. All  $\mu$ SL experimental work in this research was conducted using a Perfactory® Mini-Multi Lens Machine, Fig. 2.9.

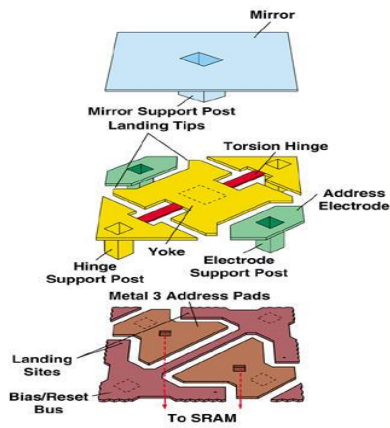


Fig. 2.7 Three layers of the Digital Micromirror Device (Texas Instruments Inc., 2005)

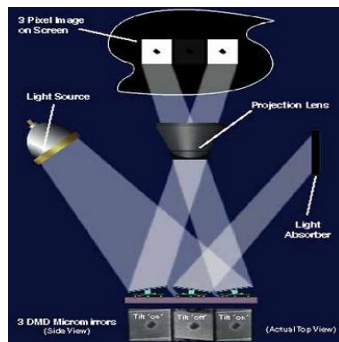


Fig. 2.8 "on" or "off" in a digital signal (Texas Instruments Inc., 2005)



Fig. 2.9 a) Perfactory machine

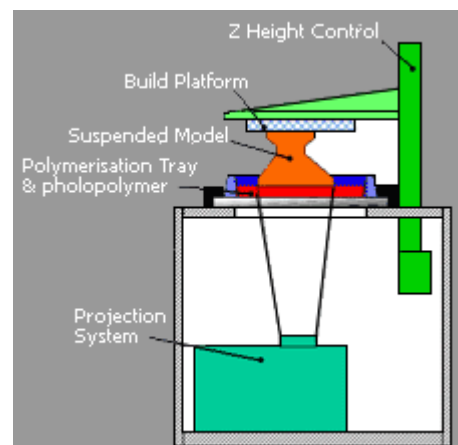


Fig. 2.9 b) Perfactory machine Layout

## 2.2 $\mu$ SL Fundamentals

This section describes the  $\mu$ SL Fundamentals such as UV Exposure Energy, cure Depth, Penetration Depth, Critical energy, Laser Exposure.

### 2.2.1 UV Exposure Energy and cure Depth

In stereolithography apparatus, cured layer thickness is controlled by the levelling system which consists of three essential elements; elevator, recoating blade and a liquid level sensor Fig 2.10. The thickness of the layer is controlled by the amount of resin recoated onto the top of the previous layer. When the laser beam scans the liquid layer surface, some radiation penetrates the previous layer and increases the cure in that layer. In case of a scanned layer with overhang, the radiation penetrates into the resin vat and is attenuated according to the Beer-Lambert law of absorption (Atkins and de Paula, 2005). According to the Beer-Lambert law, the exposure energy,  $E$  ( $\text{mJ}/\text{cm}^2$ ), decreases exponentially with the depth,  $z$ , as in Equation 2.1.

$$E_{(z)} = E_{(0)} e^{\frac{-z}{Dp}} \quad (2.1)$$

Where  $Dp$  is the penetration depth of the resin at the specified laser wavelength,  $E_{(0)}$  is the laser energy at the resin surface, and  $E_{(z)}$  is the laser energy at depth  $z$ .

### 2.2.1.1 Penetration Depth, Critical Exposure and Cure Depth

The three parameters that describe the behaviour of the photopolymer when it is exposed to UV light are; Penetration depth ( $D_p$ ), Critical exposure ( $E_c$ ) and Cure depth ( $C_d$ ). Penetration depth is the distance at which the intensity of the UV light is reduced to  $1/e$  times its value on the resin surface. The cure depth  $C_d$  is the distance to which the resin solidifies.  $E_c$  is the threshold value that is required to start polymerisation process of the resin. The three parameters are related as shown in the Cure Depth Equation 2.2 (Jacobs, 1992). If the magnitude of  $C_d$  is plotted against the exposure energy  $E$  ( $\text{mJ}/\text{cm}^2$ ) in a semi-log plot the result is a linear relationship known as the working curve Fig. 2.11.  $D_p$  and  $E_c$  can be easily found from the working curve, where  $D_p$  is the gradient of the line and the  $E_c$  is where the intercept on the x-axis.

$$C_d = D_p \ln\left(\frac{E_{\max}}{E_c}\right) \quad (2.2)$$

Where  $C_d$  is the cure depth and  $D_p$  is the penetration depth at the specified laser wavelength.  $E_{\max}$  is the laser energy at the resin surface, and  $E_c$  is the resin critical energy.

### 2.2.1.2 Laser Exposure

There are several sources of exposure energy that can be used to induce photo polymerisation (e.g. lasers, incandescent or arc lamps), however, laser sources are preferred because the exposure time required to achieve photo polymerisation is in milliseconds rather than many seconds as with arc lamps. Many suitable types of laser devices are available in the market including solid, liquid, and gas and are offered in a range of configurations to suit the needs of the desired application. The short exposure time for the polymerisation process achieved when using a laser source is because the highly collimated light beam of the laser delivers

high irradiance. In conventional SL systems as well as in DMD systems the laser profile used to solidify the resin is typically Gaussian (Zhou, 2009). The Gaussian half width is defined by laser spot size, at the radius of the laser beam spot, where the intensity drops to 1/e of the intensity at the beam axis. In a conventional SL system, the beam diameter  $2W_0$  is about 0.25mm, see Fig. 2.12. Jacobs derived the peak surface irradiance,  $H_0$ , by formulating the integral of the laser profile and solving for  $H_0$  at  $r = 0$  and  $z = 0$ , given the following result (Jacobs, 1992):

$$H_0 = 2P_L / (\pi w_0^2) \quad (2.3)$$

Where  $H_0$  is the peak surface irradiance,  $P_L$  is the laser power and  $W_0$  is the beam diameter. By dividing the laser power by the area of the laser spot on the resin surface, the average irradiance density is found. The laser power,  $P_L$ , and average irradiance density are specified at the wavelength of the laser. The exposure time  $t_e$ , that the laser spot remains on a certain area for a given scanning velocity,  $V_s$ , is derived by:

$$t_e = 2w_0 / v_s \quad (2.4)$$

$E_{max}$  is the maximum exposure incident on the resin surface is given by the relation:

$$E_{max} = \sqrt{\frac{2}{\pi}} [P_L / w_0 v_s] \quad (2.5)$$

For more details in laser power and exposure time derivations refer to (Jacobs, 1992).

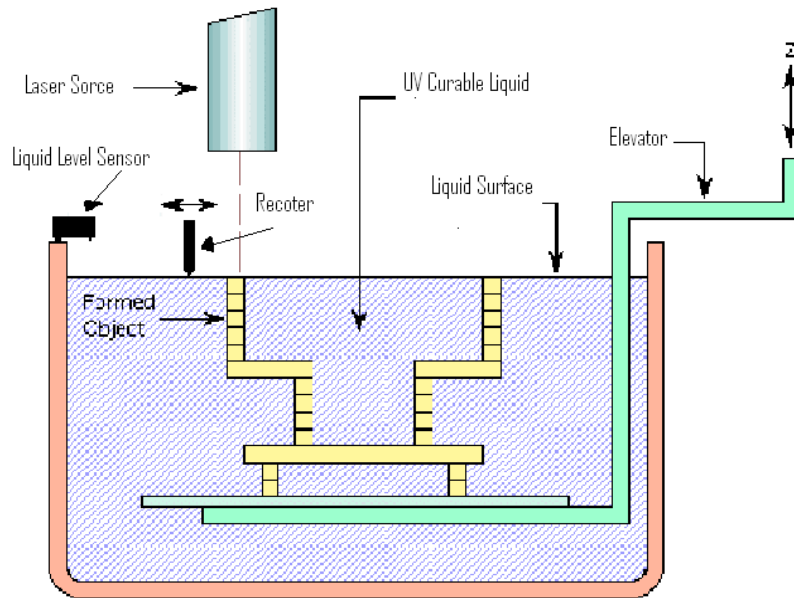


Fig 2.10 Stereo lithography system

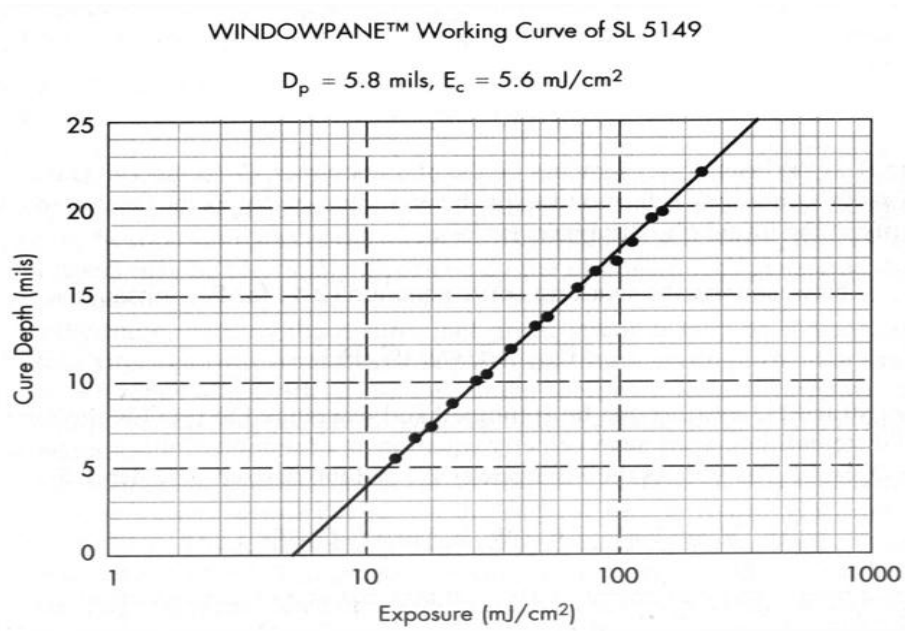


Fig 2.11 The working curve

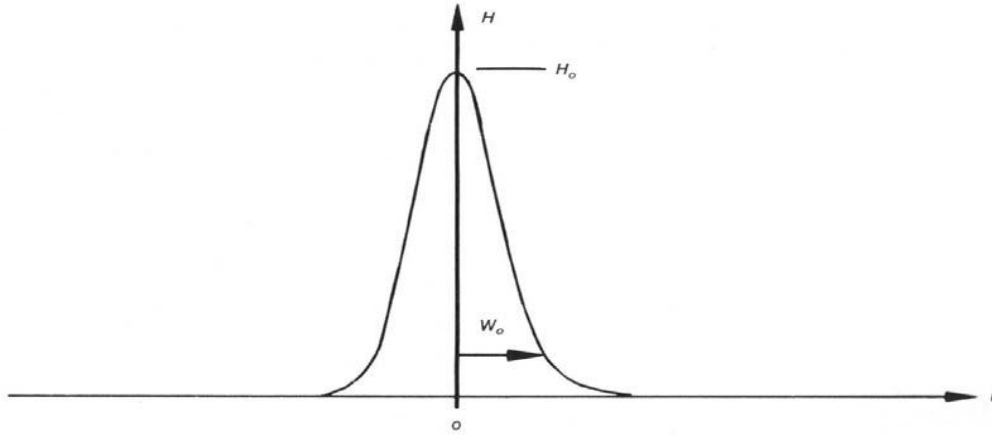


Figure 2.12 Laser profile shape and beam diameter.

## 2.2.2 Chemistry of Photopolymers

To gain a better understanding of resin properties and characteristics this section reviews the chemistry of photopolymer resins and focuses on acrylate photopolymers used for stereolithography machines. This section also examines the curing process. Cross-linking and green strength are two concepts of photopolymer resins that are explained in this section.

### 2.2.2.1 Properties of Polymers

Stereolithography involves resins that contain certain chemical properties. These photopolymers consist of several chemical molecules that solidify when exposed to UV light. Some rapid prototyping technology use EB (electron beam) radiation but the majority of RP systems use photopolymers that cure in the UV range (Jacobs, 1996). All photocurable resins can be classified under three types; epoxy, acrylate, or vinyl-ether, and all the three types contain fillers and other chemicals to give specified chemical and physical properties (Chua *et al.*, 2003).

In acrylate-based polymers (the polymer used in this research) the polymerisation process achieves photo polymerisation by using a free-radical. Ordinarily these resins consist of photo-initiators and liquid monomers. When the resin is exposed to UV light, the photo-initiators absorb some of the photons and are raised to an excited state and then the first step of the reaction starts where an initiator molecule is decomposed to produce two radicals, this is called the initiation process as in equation 2.6.





Then the initiation reaction of chain starts when the energised radicals react with the monomer molecules to form a polymerisation initiating molecule as in equation 2.7. The second step is the chain propagation, which starts when supplementary monomers react with polymerisation initiating molecules to form a large macroradical as in equation 2.8.



Where  $k_p$  is the reaction rate.

The final step is the termination process where the chain reaction terminates as a result of the inhibition process determined by the polymerisation reaction. The main reactions leading to termination of the chain reaction are; recombination, disproportionation, and occlusion. Recombination occurs when two radicals join and form a nonreactive chain end, Equation 2.9. Disproportionation occurs when  $\beta$ -hydrogen transfers from a radical to generate two molecules one with a saturated end and other with an active end, Equation 2.10. In this case the reaction continues for one second or less when the light is cut. Occlusion (or frozen mobility) is when some of the remaining radicals could continue in very slow reaction up to several months, Equation 2.11(Jacobs, 1993).



$$\{M_{m\bullet}\} + \{M_{n\bullet}\} \quad (2.11) \text{ (Occlusion)}$$

The reaction time ranges from fraction of a second to some hours depending on the photo-initiator concentration in the resin. In SL the reaction time is almost of the order of milliseconds. The longer the UV exposure time, the longer the chains, the greater the polymer's molecular weight (Chua *et al.*, 2003).

#### **2.2.2.2 Cross-linking**

Cross-linking is one of the most important parts of the photo polymerisation process because it generates an unbreakable, continuous network of molecules, in particular in resins including monomers with more than one reactive chemical group. Parts that are made from such resins have a strong chemical covalent bonds that provide structurally strong parts. Because the bonds are so strong substantial heat is necessary to split them and the parts do not melt when heat is applied, they generally thermally decompose (Jacobs, 1996).

#### **2.2.2.3 Green Strength**

As soon as the building process is finished the part is in what is known as the “green state”. The green state is when the photopolymer has been sufficiently cured to have enough mechanical strength to support itself. The mechanical strength of the cured part is measured in terms of the elastic (Young's) modulus and tensile strength.

The gel point is the state just prior to the green state and the amount of exposure energy required to reach the gel point is the critical energy,  $E_c$  (Jacobs, 1996).

## **2.3 Light Absorbers and Stabilisers**

When plastic parts are exposed to sunlight or artificial light, this can adversely affect part life. Ultraviolet light can cause collapse of the chemical bonds in polymers, a process called photodegradation. This process causes colour changes, part cracking and changes in mechanical properties such as tensile strength and impact strength. To overcome this degradation of polymers performance a wide range of UV stabilisers are used. UV stabilisers fall into two general categories, ultraviolet light absorbers (UVA) and hindered amine light stabilisers (HALS) ( Bolgar, 2008).

### **2.3.1 Ultraviolet Light Absorbers**

By using a UVA such as Tinuvin®327 the degradation process is delayed because the destructive ultraviolet light is absorbed and scattered as thermal energy. However, suitable concentrations of UVAs and adequate part thickness are necessary before the absorption process can successfully resist photodegradation. In some applications, mixtures of UVAs and HALS form a synergic relation that can improve light stability (Ciba, 2012; Bolgar, 2008 ).

### **2.3.2 Hindered Amine Light Stabilisers**

In polymers containing hydrocarbons, the existence of high levels of hydrogen atoms causes free radical formation in the polymer, eventually resulting in chain breakage or crosslinking that degrades performance. In contrast to UVAs, HALS do not absorb UV energy, they act to inhibit degradation of the polymer by oxygen inhibition and removing radical intermediates (Ciba, 2012; Bolgar, 2008 ).

## 2.4 Related Research Work

### 2.4.1 Photocurable Resin

Scherzer and Decker (1999) studied the kinetics of photo polymerisation by using FTIR (Fourier Transform Infrared) spectroscopy. Several elements were monitored including the photo-initiator concentration, light intensity, the layer thickness, polymerisation rate, and the degree of conversion. First they studied the effect of photo-initiator in the resin. By varying the photo-initiator weight from 0.1% to 3.0%, the maximum polymerisation rate was achieved as in Fig. 2.13. The results in Fig. 2.13 show the dependence of polymerisation rate on the photo-initiator concentrations. Next they investigated the effect of light intensity on polymerisation rates. Photo-initiator concentration was kept at 0.3% and the resin exposed to different light intensities: 48, 18, and 9mW/cm<sup>2</sup>. This increase in light intensity resulted in higher maximum polymerisation rates Fig. 2.14. Finally they investigated the effect of temperature on the polymerisation rate. The photo-initiator was kept at 0.1% concentration and irradiance at 48mW/cm<sup>2</sup> and different resin temperatures were used: 25, 40, 55, 70, 85 and 100°C. Contrary to the results reported by Broer *et al.*, (1991) where Arrhenius-like behaviour was observed at lower temperatures, Scherzer and Decker reported resin temperature has no effect on maximum polymerisation rate. Tryson and Shultz (1979) also investigated the effect of temperature on the polymerisation rate and found no temperature effect for conversion rates below 40%. Fig. 2.15 shows the results the effect of temperature on the polymerisation rate.

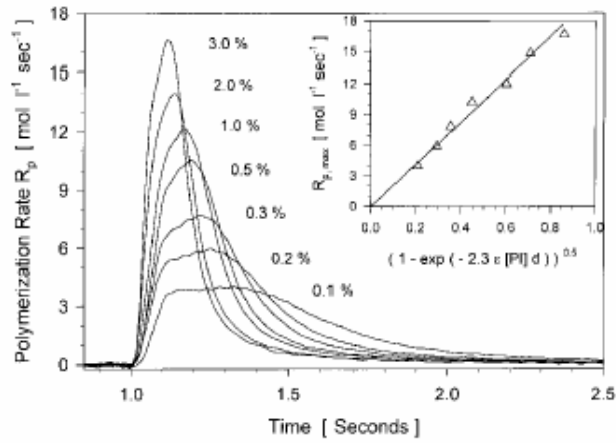


Fig. 2.13 Effect of photo-initiator concentration on polymerisation rate (Scherzer and Decker, 1999)

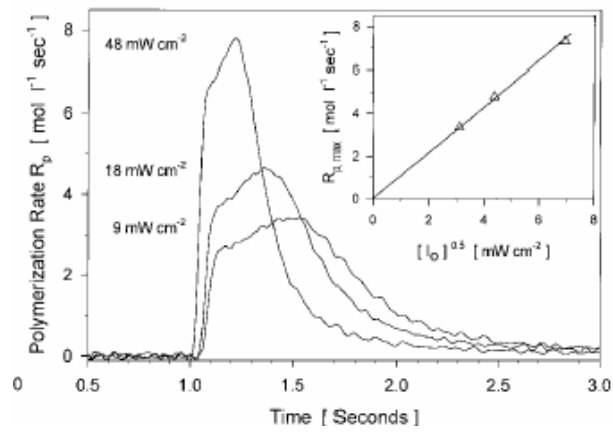


Fig. 2.14 Effect UV light intensity on the polymerisation rate (Scherzer and Decker, 1999).

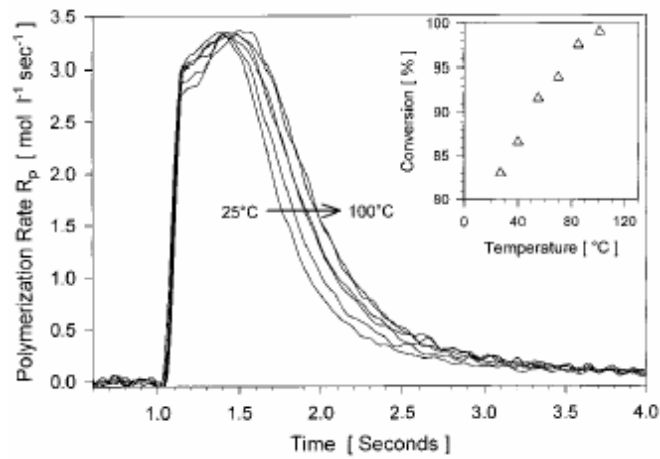


Fig. 2.15 Effect of temperature on the polymerisation rate of the acrylic double bonds of TPG (Scherzer and Decker, 1999)

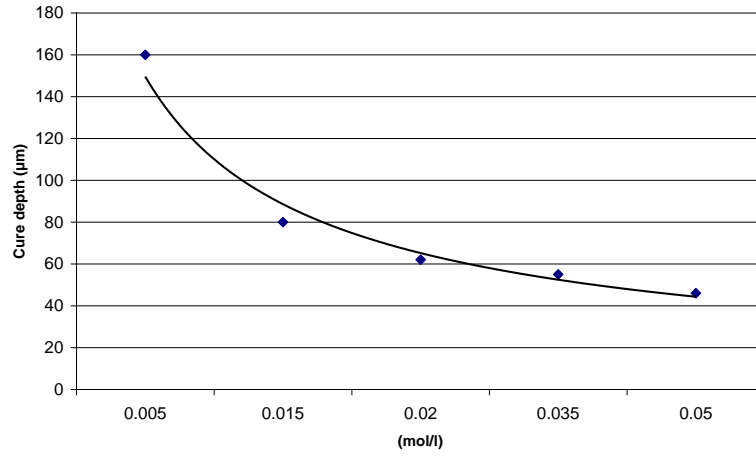
Several previous researchers reported using Tinuvin as a light absorber (Zissi *et al.*, (1996), Jae-Won *et al.*, (2009), Heller *et al.*, (2009)). Zissi *et al.*, (1996) studied the use of Tinuvin P as a light absorber or polymerisation inhibition to control cure depth in  $\mu$ SL Fig 2.16 , and the results in Fig 17 showed more accurate feature details. Zissi *et al.*, (1996) also theoretical studied the cure depth ( $C_d$ ) in relation to the light absorption concentration. Equation 2.12 shows the theoretical relationship between light absorption concentration and cure depth.

$$Cd = \frac{1}{\alpha_{\lambda} * c + \alpha_{\lambda N} * c_N} \ln\left[\frac{t}{t_0}\right] \quad (2.12)$$

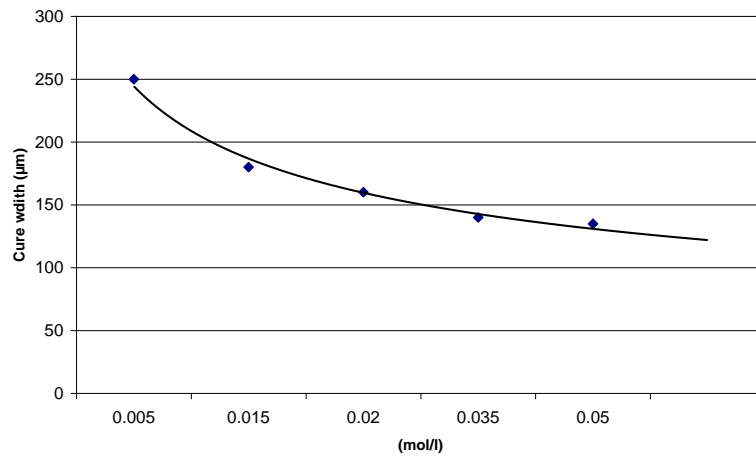
Where  $\alpha_{\lambda}$  is the absorption coefficient of the photo-initiator,  $c$  is the photo-initiator concentration,  $\alpha_{\lambda N}$  is absorption coefficient of light absorber,  $c_N$  is the light absorber concentration,  $t$  is exposure time, and  $t_0$  is the resin threshold time required to start the polymerisation process and  $t$  is the exposure time. Zissi *et al.*, (1996) successfully produced micro parts with layers of several micrometres thickness as shown in Figs 2.16 and 2.17.

Fuh *et al.*, (1999) used Raman spectroscopy, differential scanning calorimetry (DSC) and differential scanning photo-calorimetry (DSP), to study curing behaviour in an attempt to reduce post-cure distortion. Two groups of acrylic-based specimens were cured, one by heat and the other by UV light. The curing percentage of different areas on the cross-section of specimens was quantified. Also the curing percentages before and after post curing were

determined. Results showed that incompletely cured resin trapped within the photopolymer resulted in inhomogeneity of curing in the specimens causing shrinkage and distortion. It was also reported that it was difficult to determine a relationship between shrinkage and curing percentage of the examined resin (Fuh *et al.*, 1999).



a)



b)

Fig. 2.16 a) cure depth and b) cure width vs Tinuvin Concentrations (Zissi *et al.*, 1996)

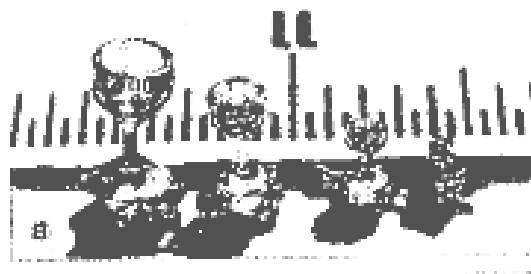


Fig. 2.17 Successfully produced micro parts (Zissi *et al.*, 1996)

Manias *et al.*, (2001), reported using Tinuvin P to control the cure depth in  $\mu$ SL to manufacture micro photocurable components with a tailored flexural modulus.

Apicella *et al.*, (2005) used a modified calorimetric analyzer (DSC 25) to determine the impact of exposure times and incremental increases in resin composite overlaying thickness on the cure kinetics of a light activated composite and a dentin adhesive at selected depths of a simulated restoration. The resin used was dental composite Z250 (3M ESPE) which is a blended dimethacrylate. The experiment was done in four stages. First a 0.3mm thick resin sample was placed on an aluminium pan and positioned in the DSC 25. While maintained at 37°C, the sample was exposed to light four times at 100sec. Another group of samples were exposed to 20sec irradiance four times and the other 60sec irradiance four times. The next step, a new thickness of resin was laid over the top. The experiment was then repeated to form a layer with 1mm total thickness. This composite wafer was used to act as the shield in the fourth step in which dentin adhesive (binds to tooth enamel) was exposed to irradiance. Apicella *et al.*, (2005) found that the shielding effect from already polymerised resin reduces the reaction rate. However, the degree of reaction was not influenced for sample sizes less than 1mm in thickness. The degree of reaction was shown to depend on the exposure.

Chockalingam *et al.*, (2006) investigated the effect of layer thickness on mechanical properties of stereolithography components. They used CIBA epoxy resin and different layer thicknesses to produce the specimens, then tensile, and impact tests were carried out. The analysis revealed that the smaller the layer thickness, the higher the strength of the part. This was attributed to resin behaviour, to residual stresses and strain relief rate which were assumed to decrease with an increase in layer thickness.

Jae-Won *et al.*, (2009) investigated the ability to fabricate micro-parts with down-facing surfaces utilising mask projection  $\mu$ SL. In order to accurately fabricate 3D parts with down-

facing surfaces, Tinuvin®327 as a light absorber was mixed in different concentrations into an acrylate-based photocurable resin to control the cure depth. The cure depth and the critical energy of the solutions were experimentally determined and then the ability of each solution to produce micro-parts with overhanging features was tested. In agreement with Zissi *et al.*, (1996), the results confirmed that higher light absorber concentrations could reduce penetration and cure depth. The ability to fabricate micro features using Tinuvin®327 was also investigated. Microstructures parts with overhanging features such as a micro-spring and a microfan were successfully fabricated. However, depending on the geometric shape of the microparts, different Tinuvin®327 concentrations for a given irradiance and exposure energy were required for successful fabrication.

Following a review of related work, the chemical composition of the resin being cured and the concentration of light absorber used to reduce the cure depth in  $\mu$ SL become important factors that have to be considered throughout the process. This is especially true when Tinuvin®327 is added to change the material properties. Thus there is a real need to further investigate the influence of Tinuvin concentration on photocurable resin to determine its influence on the mechanical properties of the fabricated parts, especially tensile strength and Young's modulus.

## 2.4.2 Cure Depth Model

Limaye (2004), designed a  $\mu$ SL system using a DMD with  $13.7\mu\text{m} \times 13.7\mu\text{m}$  pixel size. The maximum part size built by this system was  $2\text{mm} \times 2\text{mm}$ . The  $\mu$ SL system was designed to use a 50W mercury lamp as UV light source via a fibre optic light guide, and filtered by an optical filter to allow only a wavelength of 365nm to pass. Using this system Limaye characterised the curing properties ( $C_E$ ,  $D_P$ ) of DSM Somos 10120 resin. To conduct the experimental work to determine the cure depth, a U-shaped part was used to support a cured thread, as will be shown in Chapter Three. The last layer of U-shape part projected with a thread across the top of the U-shape. To obtain the working curve of the resin, the layer thickness was measured and plotted against exposure time. The  $\mu$ SL system successfully built a part of  $20\mu\text{m}$  thickness with  $6\mu\text{m}$  features in the lateral direction. Limaye (2004) also developed a mathematical model for cure depth prediction. The mathematical model for a single layer consisted of two parts: the irradiance model, Equation 2.13, and the time of exposure model, Equation 2.14. The model used ray tracing in association with the cure depth as given in Equation 2.2, to calculate cure depth for a given exposure time.

$$H(pr_i) = (H_{av} \times / \sum_{j=1}^n w_j m) \sum_{j=1}^n \sum_{k=1}^m \delta(p_j, v_k, pr_i) | \quad (2.13)$$

$$\text{TOE} = (E_c / H(pr_i)) e^{(LT/D_p)} \quad (2.14)$$

The model allows the time of exposure (TOE) to be calculated for a required layer thickness. Limaye (2004) illustrated his results by a MATLAB program as a bitmap of the irradiance matrix. To facilitate understanding the data from the irradiance map, the data is displayed as an arrow colour map Fig (2.18).

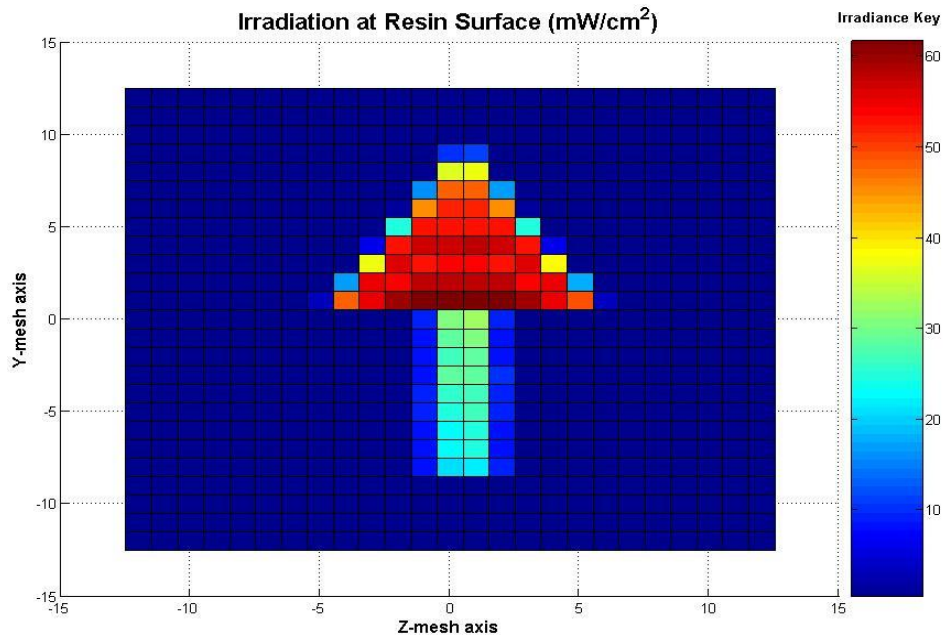


Fig. 2.18 a) Irradiation map at the resin surface of arrow shaped bitmap

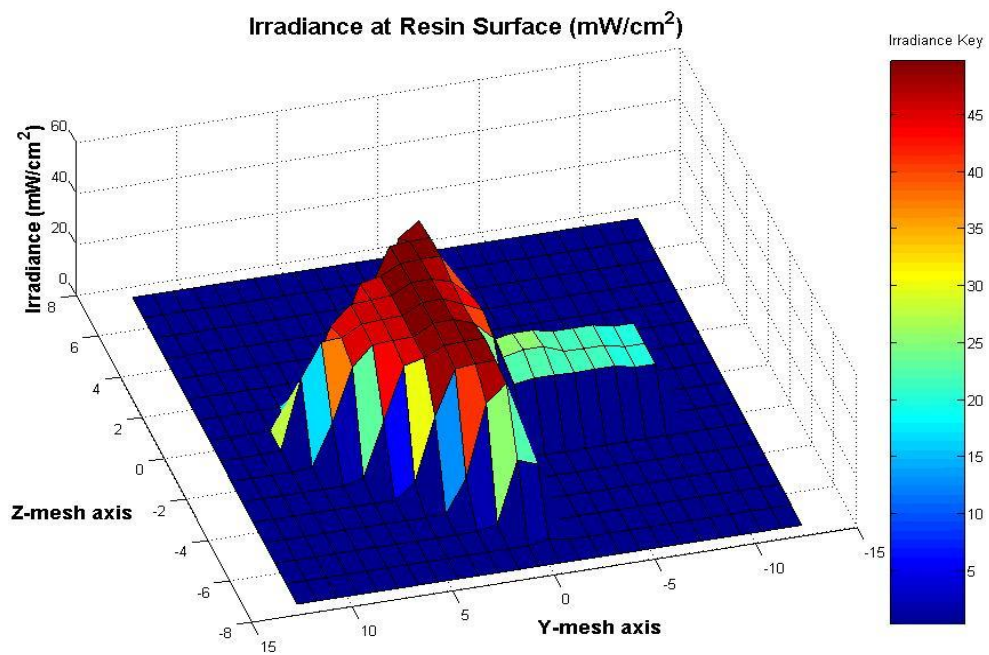


Fig. 2.18 b) Irradiance 3D distribution at resin surface using the Limaye Model.

Salmoria *et al.*, (2005) studied the thermal and mechanical behaviour of Somos 7110 SL resin. Tensile and impact tests were carried out on specimens constructed using UV radiation. The specimens were divided into two groups; the first group underwent thermal post curing, and the second group underwent UV post curing. After post curing, the mechanical properties of the specimens were assessed, followed by fractographic analysis. Salmoria *et al.*, (2005) observed that the UV post-cured specimens showed greater values for elastic modulus, tensile strength and ultimate strength than did the green samples, while the specimens subject to thermal post curing showed augmentation of mechanical properties and low defect inclination. These were attributed that to the increase in the degree of cure and cross-linking density induced by the thermal energy.

Using the finite element methods Bartolo (2006) proposed a modelling approach to study, simulate and optimise the curing processes in SL processes. The proposed model includes light and thermal initiation systems, and the effects of photo-initiator concentration, temperature and light intensity. It was reported that the model was experimentally verified and showed good agreement with experimental values (Bartolo, 2006).

Zyzalo (2008) proposed several improvements to Limaye's Layer Curing Model. To achieve more accurate predictions for the irradiance map Zyzalo first improved the irradiance map from which to calculate the whole arrow shaped bitmap. Second the MATLAB code was also improved to work with any bitmap image whilst still maintaining a realistic calculation time per layer. Finally, Zyzalo used an irradiance weighting equation to show the improvement in irradiance distributions on the map (Zyzalo, 2008).

Zhou *et al.*, 2009 presented an optimisation method for mask image planning, based on a light intensity blending technique. The pixel blending problem was mathematically defined and several optimisation models for solving the problem were presented, including a mixed-

integer programming model, a linear programming model, and a two-stage optimisation model. By controlling the gray scale values of the pixels, the SFF processes achieved a much higher X-Y resolution and part quality (Zhou *et al.*, 2009).

Jariwala. *et al.*, (2010) extended and enhanced the model developed by Boddabati (2010) to predict the height and shape of the cured part, and simulate cure depth and width. The model was originally developed by Boddabati (2010) using a 2D Ordinary Differential Equation 2.15(ODE) and enhanced by Jariwala *et al.*, (2010) to include oxygen diffusion and chemical kinetics as shown in Equation 2.16.

$$\frac{d[O_2]}{dt} = -k_{toxy}[O_2][R^*] - k_{toxy}[O_2][P^*] - D_{O_2} \left\{ \frac{\partial^2 [O_2]}{\partial z^2} \right\} \quad (2.15)$$

$$\begin{aligned} \frac{d[O_2]}{dt} = & -k_{toxy}[O_2][R^*] - k_{toxy}[O_2][P^*] \\ & - D_{O_2} \left\{ \frac{\partial^2 [O_2]}{\partial x^2} + \frac{\partial^2 [O_2]}{\partial z^2} \right\} \end{aligned} \quad (2.16)$$

The model successfully predicted the effect of oxygen inhibition and diffusion on cure depth. The simulated results were in a good agreement with the experimental observations for predicting part height when compared with COMSOL finite element simulation Fig. 2.19.

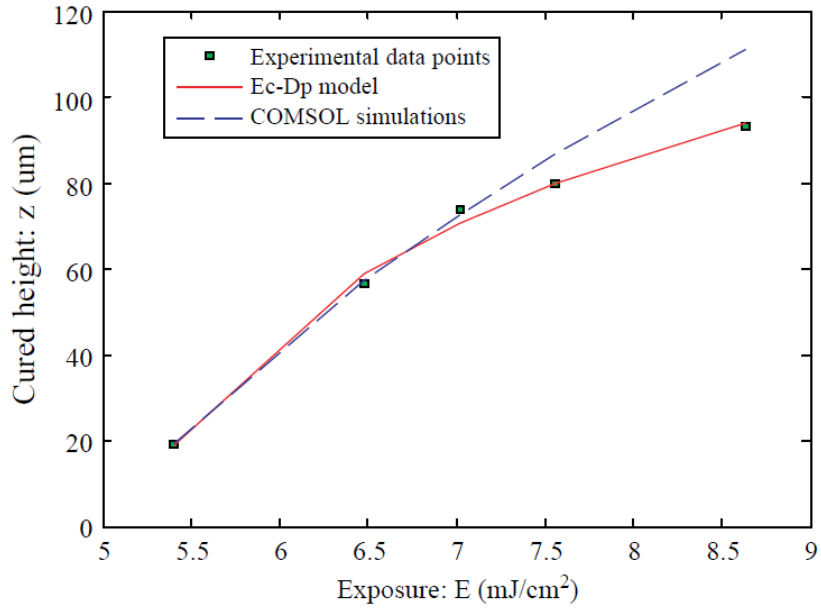


Fig. 2.19 Comparison of measured and predicted part heights (Jariwala. *et al.*, 2010)

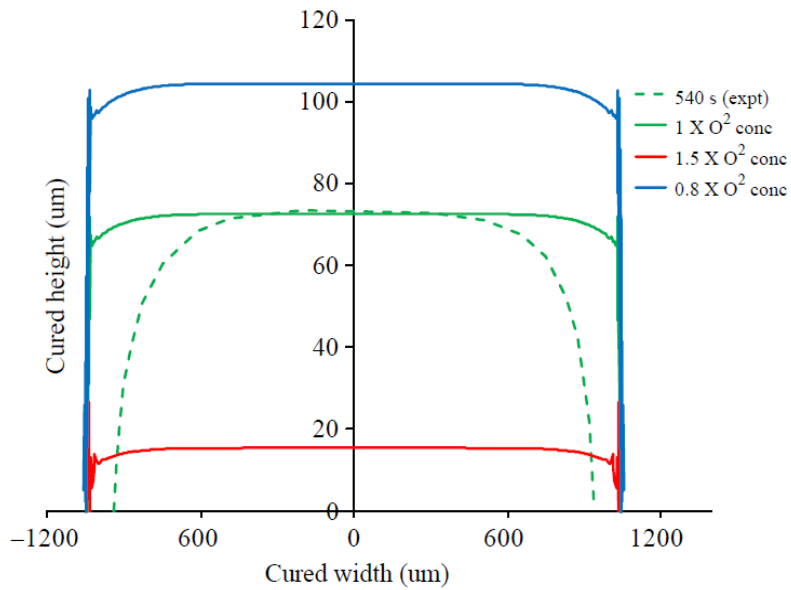


Fig. 2.20 Comparison of measured and predicted part widths (Jariwala. *et al.*, 2010)

However, the model was not so accurate in predicting cured part width and edge curvature Fig. 2.20. Jariwala's model needs to be further improved to explain the observed reduction of part width and the curvature. This might be done by optimising the chemical rate constants and incorporating the effects of shrinkage (Jariwala. *et al.*, 2010).

Boddapati *et al.*, (2011) presented a kinetics model for double-bond conversion and gel time prediction in the photo polymerisation of multifunctional acrylates. Boddapati *et al.*, used Fourier-transform infrared spectroscopy (FTIR) measurements to monitor double bond. Boddapati *et al.*, reported that the measured gel time correlated with both the calculated initial rate of radical generation and a constant value of the predicted double-bond conversion, over a broad range of conditions (Boddapati *et al.*, 2011).

In attempt to predict the curl deformation in stereolithography process, Vatani *et al.*, (2012) used the classical lamination theory to model the curl distortion in stereolithography parts. Classical lamination theory is utilised to model the mechanical properties, layers shrinkage and residual stress development during SL process. As a result curl distortion is will predicted based on the developed model. In agreement with (Kim & Lee 2005) results show that curl distortion is proportional to layer thickness and it increases exponentially as layer thickness decrease (Vatani *et al.*, 2012).

So far, an extensive research was reported in the area of cure depth model, but there has been no study considering the changes in cure depth behaviour after the addition of Tinuvin as a light absorber, and a question is raised up which is, Is there any changes occurred to the cure depth model proposed by Jacob 1992 due to the changes in material characteristics?. Therefore, there is a real need to study the relationship between the exposure energy and the cure depth again after the addition of Tinuvin.

### 2.4.3 Final Part Accuracy.

RP and tooling technologies allow complex parts to be produced in a few hours. These technologies require accurate knowledge of vertical resolution, spatial resolution, shrinkage compensation and surface finish.

To improve the final part accuracy Yan *et al.*, (1998) studied machine accuracy in RP and classified the most common sources of errors as mathematical, process-related or material-related.

Wang *et al.*, (1997) showed that there are significant correlations between process parameters and post-curing shrinkage in SL processes. Wang *et al* found that the line width and cure depth were logarithmic proportional to the laser power.

Gregorian, *et al.*, (2001) used benchmarking to calculate the optimal shrinkage compensation factor (SCF) in order to improve the accuracy in a RP machine (FDM-1650). Although Gregorian was very precise in calculating the most possible accurate shrinkage compensation factor, the shrinkage compensation factor did not take into account the differences in X and Y shrinkage due to limitations in machine software.

Tang *et al.*, (2004), studied the accuracy of RP in terms of defining error sources and analysing their contribution to the final part accuracy. The error sources were classified into those related to (i) the machine (hardware and software), (ii) the materials and (iii) the process. Special attention was paid to the errors caused by laser scanning and compensation software was developed to correct the errors resulting from galvano-mirrors and lenses. Also a compensation program was added to the slicing software to compensate for the errors caused by material shrinkage and beam offset and this minimised the error to  $\pm 0.2\text{mm}$ .

Zhou *et al.*, (2001) studied the build parameters that affect the quality and accuracy of the final SL parts, namely, the layer thickness, overcure, hatch space, blade gap, and part location. A benchmark of twenty different dimensional, geometrical, and surface features was used to evaluate the resulting errors. In attempt to reduce the number of experiments required, a Taguchi L27 orthogonal array was used. ANOVA analysis techniques and MINITAB software were used to identify the factors that were most significant in determining the quality and accuracy of part features and surface roughness. The analysis suggested the best setting of these control factors for each individual feature and an optimal setup of the build parameters for building a general part consisting of a mixture of various features with minimum laser scan time. The total laser scan time and the corresponding total recoating time were examined separately for each of the 27 cases studied. Design and manufacturing features such as overhangs and thin shells were not considered as these may not have responded in the same way as the features identified.

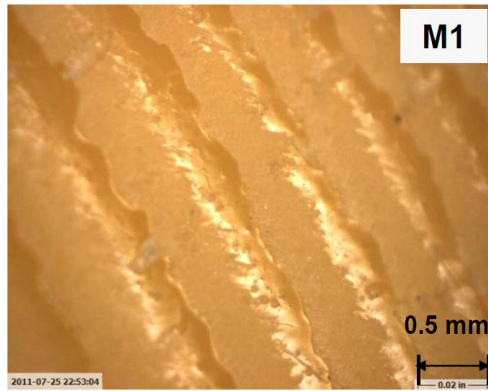
Hackney *et al.*, (2005) used Taguchi techniques and statistical tools to find the percentage contribution of process parameters on part hardness, strength, and accuracy. The process parameters involved in the investigation were layer thickness, peel velocity, pixel size, waiting time, exposure time and orientation. It was noted that layer thickness and part orientation have the most affected on part accuracy.

Chiu *et al.*, (2008) used image-processing technique to calibrate the photomask of a mask projection RP. In order to rescale the photomask image a set of optical lenses were positioned facing the DLP. Then the new scaled image was sent to a computer via a digital camera. Using this technique, the actual size of the photomask was calculated and the designed part dimensions were achieved with maximum error of 0.02mm by adjusting the locations of the lenses.

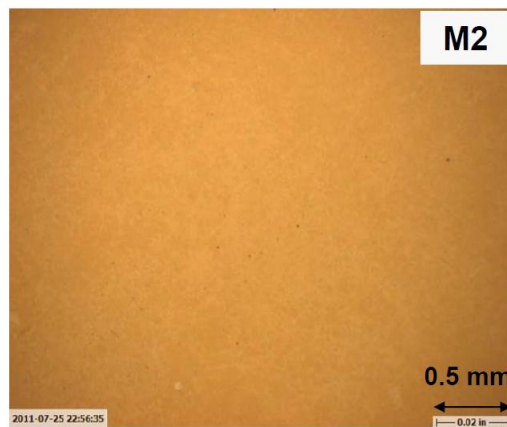
Pan *et al.*, (2011) have presented a new approach which constructs smooth curved surfaces for mask projection SL. The approach used had two steps; first a meniscus equilibrium method was developed for up-facing surfaces, and a process planning problem formulated for the up-facing surfaces based on the developed meniscus models. Then an algorithm was developed for the process planning problem. For down-facing surfaces a grey scale image method was developed based on the calibrated model between curing depth and gray scale value, then a process planning algorithm was developed for the down-facing surfaces. Results from comparison between these methods and the traditional method, see Fig. 2.21, show a significant improvement was achieved. Although the new approach achieved a better surface quality compared with the traditional approach a discontinuous error problem arose, see Fig. 2.22, which was similar to the trapped volume problem. To overcome this problem the designed part should have an outlet for excess liquid resin to flow away.

From the reviewed research, it can be concluded that the part accuracy in  $\mu$ SL is an important factor affecting the final part performance. It is a challenging research issue that needs addressing especially with the increased use of material additives such as light absorbers whose effects on accuracy have never been investigated. To carry out such an investigation it is necessary to find out the effects of, e.g., Tinuvin on part shrinkage, surface roughness and dimension accuracy.

The review of previous research shows that some essential questions remained to be answered. These include the effect of the light absorber on the mechanical properties. Does the use of light absorber effect dimension accuracy? Does the use of light absorber change surface roughness? This particular research is aiming at helping answering these questions. More particularly it is focused on the effects of different concentrations of light absorber on the part density, shrinkage and mechanical properties of the parts.



a)



b)

Fig. 2.21 Microscopic images of up-facing surfaces a) M1 traditional approach, b) M2 new approach (Pan *et al.*, 2011)

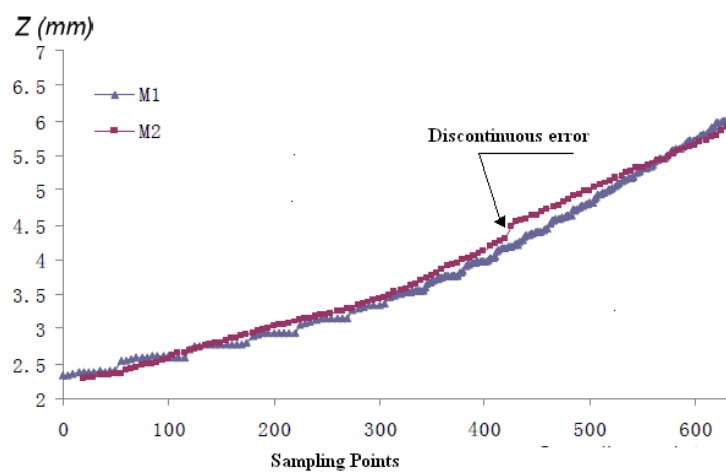


Fig. 2.22 Discontinuous error resulted from the new approach (Pan *et al.*, 2011)

## **2.5 Summary**

In this chapter different types of RP systems have been reviewed and classified. Then, the fundamentals of SL have been explained, including exposure energy, critical energy, cure depth and penetration depth. The two general categories of light stabiliser have been briefly described and reviewed in this chapter. Next the chapter discussed related research work: photo curable resin, the cure depth model and the final part accuracy. Finally the challenging research areas that need addressing were assessed and reported.

## Chapter 3

### **Investigation of the Influence of a Light Absorber on the Mechanical Properties of Acrylate Micro Stereolithography Part**

This chapter reports the experimental work conducted to investigate the effects of Tinuvin®327 as a light absorber on cure depth, critical energy, penetration depth, mechanical properties and part density. The chapter begins with a short presentation of preliminaries on  $\mu$ SL and its development following on from Chapters 1 and 2. At the end of this chapter a solution is proposed to the problem of reduction in mechanical properties caused by the addition of Tinuvin®327.

#### **3.1 Preliminaries**

The Perfactory® system  $\mu$ SL mask projection machine which, as described in Section 2.1.3.3 uses tilting micro-mirrors to direct light of a particular wavelength from side to side of the resin several times per second. The Perfactory® system can project a greyscale image. A light sensometer is attached to the machine for measuring and calibrating the light intensity over the base-plate. The sensometer measures 48 light spots on the baseplate and uses the measured values to adjust the light intensity of the grey mask. Subsequently the grey image is focussed by an optical system onto the resin surface to solidify the designed part.

The Perfactory® is provided with an electromechanical shutter which is used to expose the resin for the required duration for the resin to solidify. When the process begins the first polymerised layer between the baseplate and the vat surface is attached to the vertically movable base plate. To free the solidified layer from the vat, the vat tilts to the outside, then

the part peel out and no longer sticks to the vat. The baseplate then moves in the Z direction after solidification of each successive layer leaving 25-100  $\mu\text{m}$  of liquid resin between the previously cured layer, and the vat surface. By repeating this process the solidified 2D cross-sections are attached together to form 3D parts (Choi *et al.*, 2009).

### **3.1.1 Definition of the problem.**

In order to fabricate a microstructure part with  $\mu\text{SL}$ , the 3D design model has to be sliced to layers of the required thickness, and each cured layer must be bonded with the previous layer during solidification in order to make up the designed geometry. To correctly fabricate these thin slices the cure depth ( $C_d$ ) has to be similar to the sliced thickness (Lee *et al.*, 2001). The two parameters used to determine the exposure energy ( $E_x$ ) for fabricating the thin layers and bond them together are the penetration depth ( $D_p$ ) and the critical energy ( $E_c$ ) (Jacobs, 1993). In a  $\mu\text{SL}$  system the layer thickness to be polymerised is given by the amount of resin between the last cured layer and the vat surface (Zissi *et al.*, 1996). Excess radiation increases the curing of the previous layer so vertical resolution considerably impacts on the ability of  $\mu\text{SL}$  to reproduce 3D microstructures and means many undesired microstructures could be ‘fabricated’ if the cure depth is greater than the slicing thickness (Choi *et al.*, 2009). However, if the part is designed to contain overhangs or bridges the radiation which penetrates into the resin vat to increase the thickness of the hanged layer will affect the vertical resolution. Thus, geometric and dimensional accuracy will be influenced by this over-penetration. To successfully fabricate 3D microstructures with down-facing surfaces, the cure depth must be controlled by adjusting the curing characteristics, critical energy and cure depth.

### 3.1.2 Critical energy and cure depth.

As shown in Equation 2.2 Jacobs (1992) found the cure depth  $C_d$  is proportional to the logarithm of  $E_{max}/E_c$  so that when  $C_d$  is plotted against  $E_{max}$ , where  $E_{max}$  is the irradiance in mW/dm<sup>2</sup> multiplied by the exposure time in seconds, the result is a straight line with gradient equal to  $D_p$  see Fig. 2.11 and Equation 2.2.

The gradient and intercept of the line depend only on the resin constants  $E_c$  and  $D_p$ , and so is characteristic of the resin and the line is called the ‘working curve’ (Chua, 2003). Fig. 3.1 represents the working curve for HS 660 resin. In this investigation, working curves were obtained for different concentrations of Tinuvin® 327 in the acrylic resin. The results for  $E_c$  were obtained and analysed to determine the influence of the photo-absorber on the photopolymerisation behaviour of the resin.

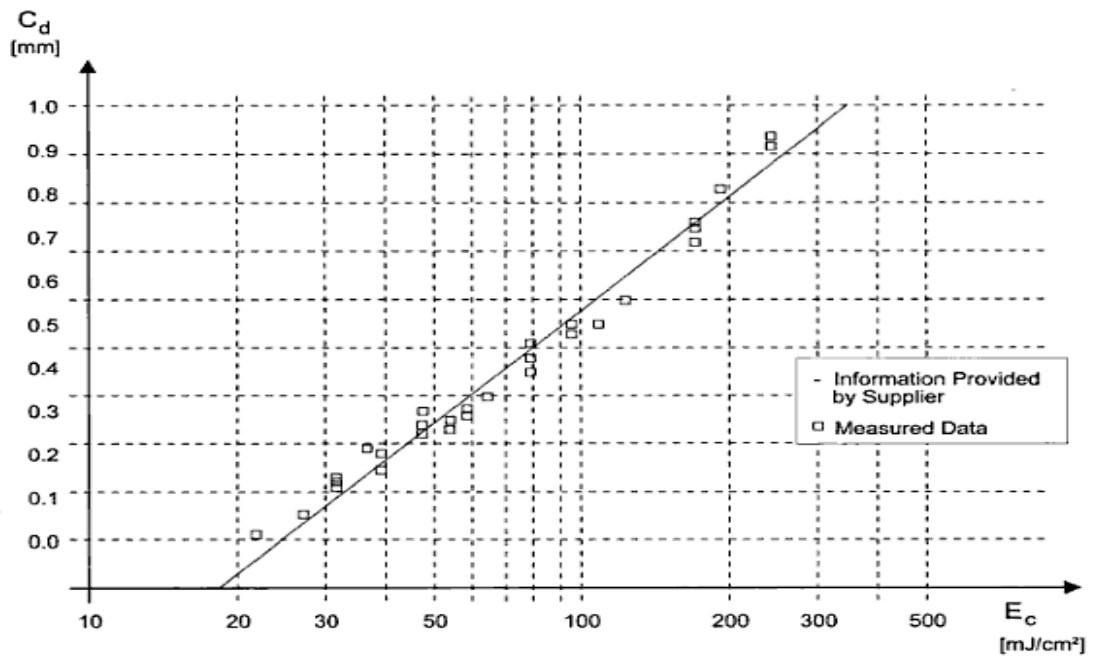


Fig. 3.1 Cure depth as a function of exposure energy  
working curve for HS 660 resin (Chua, 2003)

## 3.2 Experimental Work Defining and Analysing Curing Depth

This section reports the experimental work to investigate the effects of light absorbing Tinuvin®327 on cure depth, critical energy, and penetration depth. The section starts with the material preparation for this experimental work, followed by the design of the test part used to conduct the experiments. The remainder of the section reports the results with a discussion of the cure depth, critical energy and penetration depth experiments.

### 3.2.1 Materials

A commercially available 1,1,1 Trihydroxymethylpropyl-triacrylate resin (PIC-100) from EnvisionTEC® was chosen because of its wide use for functional prototyping and for production of sacrificial patterns in precision micro-investment casting. This material is also used as a pattern for electro-forming replication and Ni-shim masters (Minev *et al.*, 2010). All of the above applications require high mechanical strength and accuracy. Tinuvin® 327 (2,4-di-ter-butyl-6-5-chlorobenzotriazol-2-yl-phenol) Fig. 3.2 from (Ciba USA) was chosen as the light absorber. It was selected because of its high absorbance in the 300-400 nm regions with maximum rate at 353 nm as shown in Fig 3.3. Tinuvin® 327 is available in the form of a fine powder and can enhance light stability of commercial plastics when added to different organic substrates (Ciba, 2008). Five samples were prepared to investigate the curing depth of the resin, the resin without light absorber, and the resin with four different concentrations of Tinuvin® 327. 0.1, 0.25, 0.5 and 1.0 % (w/w) of Tinuvin® 327 was dissolved in chloroform (CHCl<sub>3</sub>) and then mixed with PIC-100 resin in a roller for 12 hours to obtain an homogenous distribution of the ingredients and allow the chloroform to evaporate.

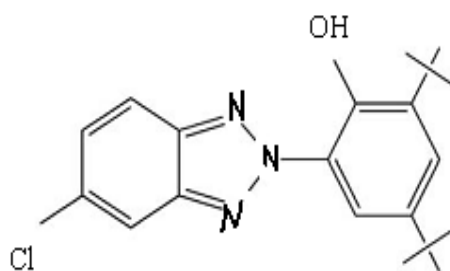


Fig 3.2 Tinuvin 327 structure (source Ciba 2008)

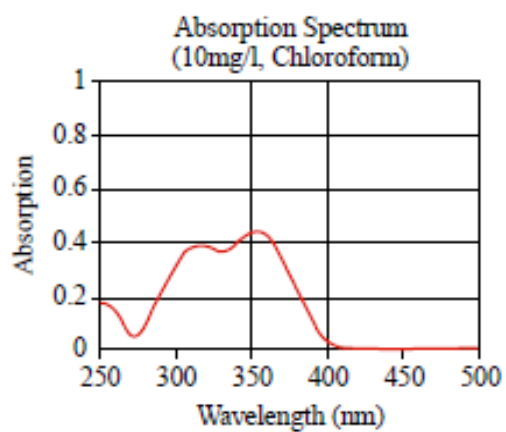


Fig 3.3 Tuivin® 327 absorption in Chloroform solution (source Ciba 2008)

### **3.2.2 Tested Part Shape and Design**

The specimen used to perform the cure depth experiments had a U-shaped form as shown in Fig. 3.4 which is similar to that used by Limaye (2004). The shape was designed with Solid Works® software and had dimension 3mm long x 1mm wide x 3mm high. The shape of the part offered easy handling. It was built with the last layer having a thread cured across the top of the U-shape with thickness of one layer. The thickness of the thread was measured as an indication of the cure depth.

### **3.2.3 Fabrication of the U-shaped Part**

The U-shape part shown in Fig. 3.4 was fabricated in the MEC laboratory in Cardiff University with the Perfatory® Mini Multi Lens machine (Perfactory 2008). Acrylate PIC-100 resin was polymerised with 12 different UV irradiance values from 300 to 1400 mW/dm<sup>2</sup> with wavelength of 325 nm to investigate the effect of Tinuvin®327 concentration on cure depth. The selection of the irradiation range was chosen to include values above and below those recommended by the resin supplier EnvisionTEC®, see Table 3.1. The irradiance was calibrated using the Prefactory® photosensor, and the average irradiation error was  $\pm 2.6$  mW/dm<sup>2</sup> which was considered acceptable since the maximum permissible error is recommended as  $\pm 10$  mW/dm<sup>2</sup> (Perfactory, 2008). All parts were fabricated using a layer thickness of 25  $\mu$ m and 7 s exposure time. After the building process was finished, the supports were removed and the part was cleaned with isopropyl alcohol, dried gently with compressed air and then placed in incubator at 37C° for 30 minutes for further drying. In order to minimise measurement error, eight parts were built from each irradiance level, a total of 96 parts.

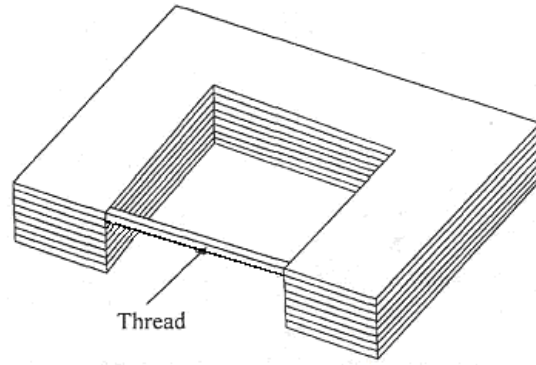


Fig. 3.4 Shape of test part (Lamaye, 2004)

Table 3.1  $\mu$ SLA fabrication parameters.

Trial No	Layer Thickness ( $\mu\text{m}$ )	Exposed time (s)	Irradiance ( $\text{mW}/\text{dm}^2$ )
1	25	7	300
2			400
3			500
4			600
5			700
6			800
7			900
8			1000
9			1100
10			1200
11			1300
12			1400

### 3.3 Results and Discussion

This section reports the results obtained from the experimental investigation conducted to address the effects of Tinuvin®327 as a light absorber on the cure depth, penetration depth and critical energy.

#### 3.3.1 Control of Cure Depth

Tinuvin®327 shows a significant effect on cure depth for PIC-100 acrylate resin. Fig. 3.5 shows the cure depth test part after fabrication, and Fig. 3.6 shows the effects of different Tinuvin®327 concentrations on cure depth as indicated by the thread thickness. The smallest cure depth achieved was 18  $\mu\text{m}$  (achieved using an irradiance of 300  $\text{mW}/\text{dm}^2$ ), as shown in Fig. 3.6 (e). This is smaller than the amount required where the nominal depth of the single layer was 25  $\mu\text{m}$  and a thickness of 18  $\mu\text{m}$  was considered a reasonable result for the cure depth. However, 18  $\mu\text{m}$  thickness is considered insufficient to provide adequate part strength. The minimum cure depth required for a full strength part was 60  $\mu\text{m}$  so it was decided to use the irradiance recommended by the supplier, 800  $\text{mW}/\text{dm}^2$ , which meant that all the Tinuvin concentrations used gave an acceptable part strength.

Fig. 3.6 shows that when using 1% Tinuvin concentration the cure depth was 60  $\mu\text{m}$  and the maximum cure depth was 116  $\mu\text{m}$  at 0.01% Tinuvin concentration. Although Tinuvin had a significant control over cure depth, however it cannot prevent penetration from excessive irradiance. The thickness of the thread was measured as indication of the cure depth using Leica white light microscope for different exposure energy. The results are shown on Fig 3.7. The figure shows that increase of light absorber concentration reduces the cure depth for a given exposure and reduces the sensitivity of the material to the curing energy input. This latter observation is indicated by the reduced steepness of the gradients (particularly visible in Fig. 3.7 (b) – semi-logarithmic representation) with increase in Tuvin concentration.

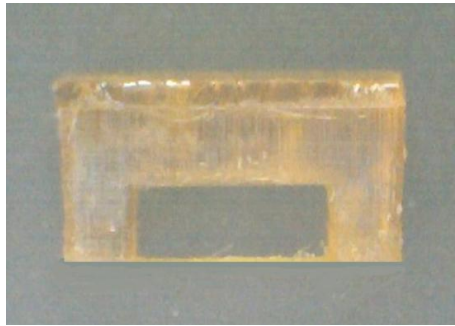
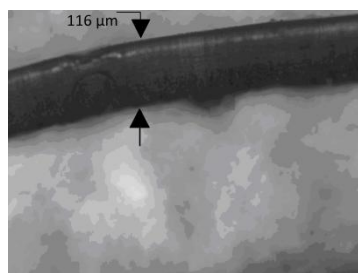
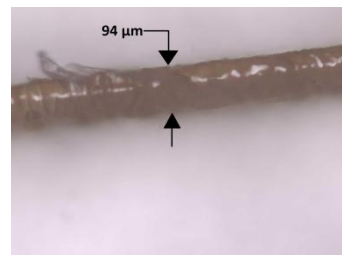


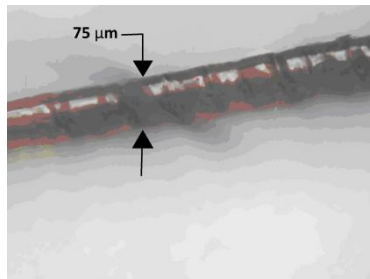
Fig. 3.5 Test Part after fabrication



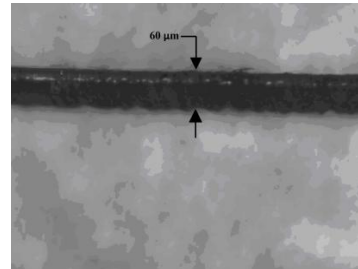
a)



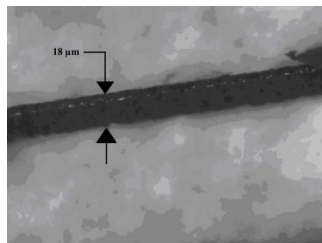
b)



c)

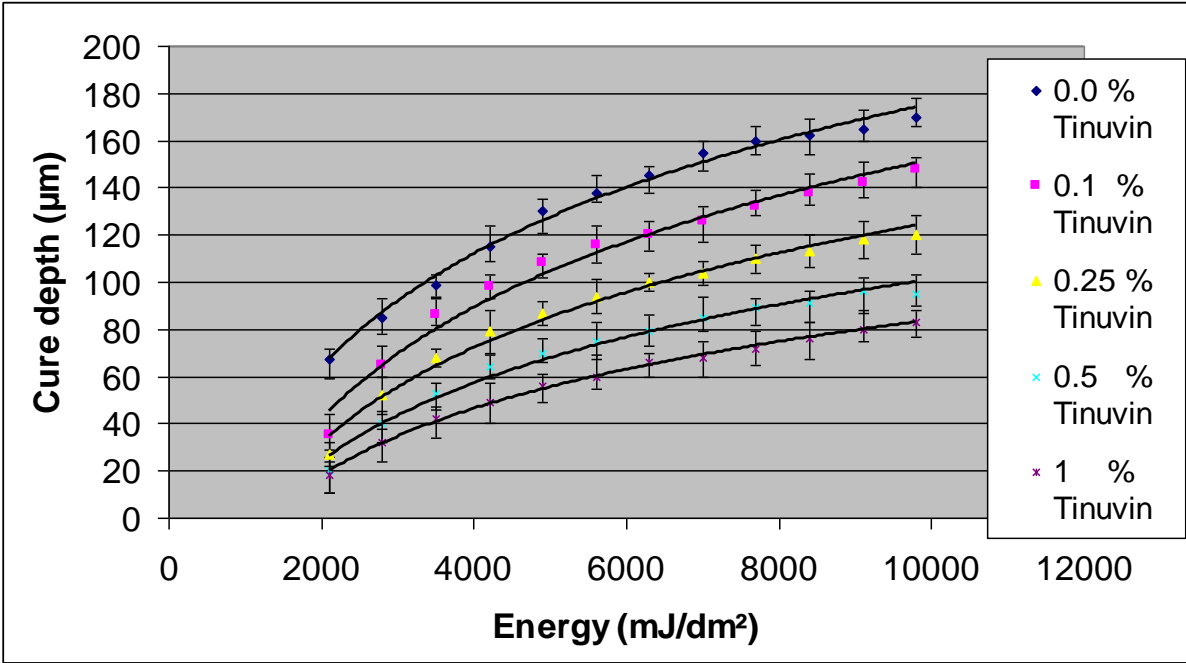


d)

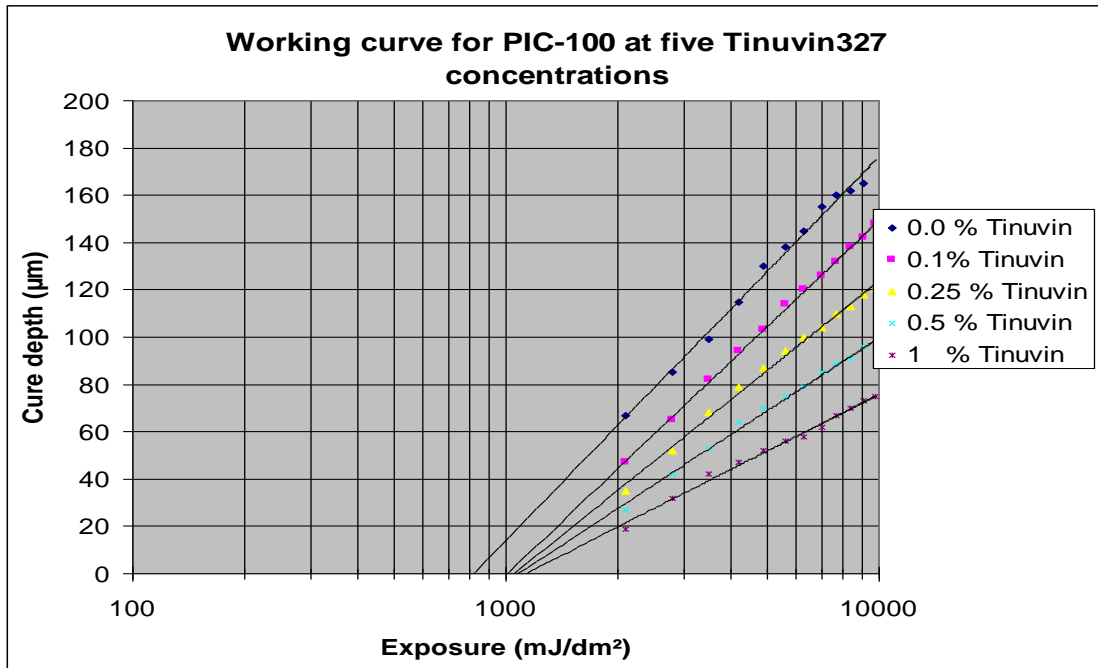


e)

Fig 3.6 Cure depths for irradiance level of  $800 \text{ mW/dm}^2$  for four different Tinuvin concentrations: (a) 0.1% ( $116 \mu\text{m}$ ), (b) 0.25% ( $94 \mu\text{m}$ ), (c) 0.5% ( $75 \mu\text{m}$ ), and (d) 1.0% ( $60 \mu\text{m}$ ). The smallest cure depth achieved is shown in (e)  $18 \mu\text{m}$  with 1% Tinuvin concentration 7 seconds exposure time and  $300 \text{ mW/dm}^2$ .



(a)



(b)

Fig. 3.7 The effect of different Tinuvin®327 concentrations on cure depth of PIC-100, (a) linear scales, (b) log-linear scales

### 3.3.2 Determination of Critical Energy.

Critical energy ( $E_c$ ) and depth of penetration ( $D_p$ ) were determined directly from the semi-logarithmic plot of cure depth versus  $\ln(\text{exposure})$ . Fig. 3.7 (b) shows the graphs of cure depth versus exposure energy for the resins with five different absorber concentrations.  $E_c$  is the intercept of the working curve with abscissa and  $D_p$  is the gradient of the line. The results from these calculations are presented in Table 3.2. These results are in agreement with the expected material behaviour and could be used to design an appropriate curing procedure for materials with different absorber concentrations. It is evident that the curing input energy could vary by nearly 30% when a significant amount of light absorber is added to the compound. The penetration depth of the light when absorber is added to maximum recommended level (e.g. 1%) (Ciba, 2008) could be reduced by more than 50% compared with the pure resin.

Table 3.2 Experimentally measured values of  $E_c$  and  $D_p$

Tinuvin® Concentration %	Critical Energy ( $E_c$ , mJ/dm <sup>2</sup> )	Penetration Depth ( $D_p$ , $\mu\text{m}$ )
0.0	820	70
0.1	1000	65
0.25	1052	55
0.5	1080	44
1.0	1132	34

### 3.3.3 Confirmation of Obtained Critical Energy

To confirm the results obtained from the experiments to determine curing depth, an additional dependent critical energy investigation was carried out. The same acrylate resin was used which was as received. Photo-initiation was induced using the same UV lamp with the same wavelength of 325 nm. In this experiment as in the previous one chloroform was used as a solvent (Tinuvin has its highest solubility in chloroform 19% w/w). Five different samples were prepared with different concentrations of Tinuvin®327 (0.0, 0.1, 0.25, 0.5 and 1.0 % w/w) in PIC-100 acrylate based resin. Each solution placed in a sealed bottle on a bench top roller and allowed to mix for a period of 24 h to ensure homogeneity. Excess solvent was removed by evaporation at room temperature. A Perfactory® mini multi lens SL apparatus was employed for the photopolymerisation. The purpose of these experiments was to obtain single cured layers. A rectangular glass slide (75mm long x 25mm wide x 1mm thick) was placed on the top of the calibration plate, see Fig. 3.8. Drops from each of the five samples were dropped onto the glass slide. Samples were cured by spreading the drop by small brush into an approximately circular shape of diameter 10 mm, see Fig. 3.9. Ten UV exposure levels were used; the levels were obtained from the working curve, five above the critical energy obtained from the curve in Fig 3.7b and five below. The exposure levels were controlled by varying the UV light irradiance via the SL software. After polymerisation, the glass slices with the polymerised gel layer still attached were lifted off. Isopropanol solution was used to remove uncured PIC-100 resin, and then the slide was dried in a ventilated incubator for 30 minutes at 37°C. The thicknesses of the dry cured gels were then measured with a digital micrometer. The experimental results obtained from the gel spots are presented in Table 3.3, and show good agreement with the critical energy values obtained from the cure depth experiments and critical energy calculations.

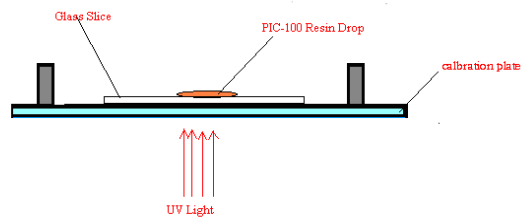
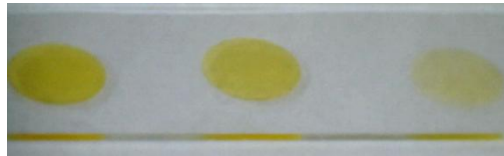


Fig. 3.8 Position of glass slice on calibration plate



(a) Different exposure energy results for different gel thicknesses



(b) Magnified picture for the minimum gel thickness obtained (18  $\mu\text{m}$ )

Fig. 3.9 Gel spots for calculating critical energy

Table 3.3 Critical energy obtained from critical energy confirmations experiments.

Tinuvin®327 Concentration %	Critical Energy from Gel spots  ( $E_c$ , mJ/dm <sup>2</sup> )	Critical Energy from working curve  ( $E_c$ , mJ/dm <sup>2</sup> )
0.0	826	820
0.1	1006	1000
0.25	1057	1052
0.5	1078	1080
1.0	1134	1132

### 3.4 Experimental Investigation of Mechanical Properties

This section investigates the influence of Tinuvin® 327 on the mechanical properties of the part being produced. Five samples with the same proportions of Tinuvin as described above were used. The tests were performed at room temperature using D638-08 standard V type specimens as shown in Fig. 3.10. The tensile specimens were designed using SolidWorks CAD software and fabricated using the Perfactory® Mini Multi Lens machine (Perfactory 2008). Acrylate PIC-100 resin was polymerised with 25µm layer thickness and 800 mW/dm<sup>2</sup> irradiance with wavelength of 325 nm to investigate the effect of Tinuvin®327 concentration on tensile strength. The tensile tests were carried out using a Testometric M500 machine, see Fig. 3.11. In the tensile tests, stretching of the specimens was performed at a constant speed rate equal to 10 mm/min. The experimental stress strain curves obtained for the five samples are shown in Fig. 3.12. The specimens show that the resin behaves similarly to a brittle solid; the stress rises linearly with strain followed by sudden fracture. The fracture occurred when the stress reached between 5-16 MPa, the greater the proportion of Tinuvin the weaker the material. The elastic modulus was estimated by measuring the slope of the linear stress-strain curves, which gave an elastic modulus of between 8 and 20 MPa, again the higher the proportion of Tinuvin the lower the elastic modulus.

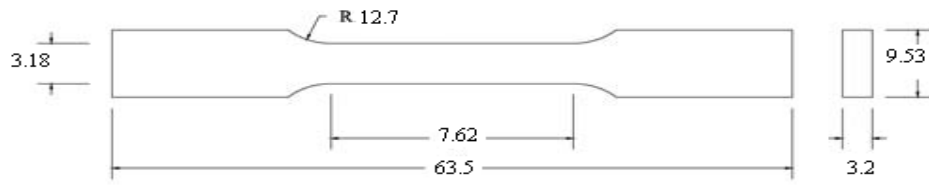


Fig 3.10. D 638-08 standard V type specimens.



Fig 3.11. Testometric M500 tensile test machine

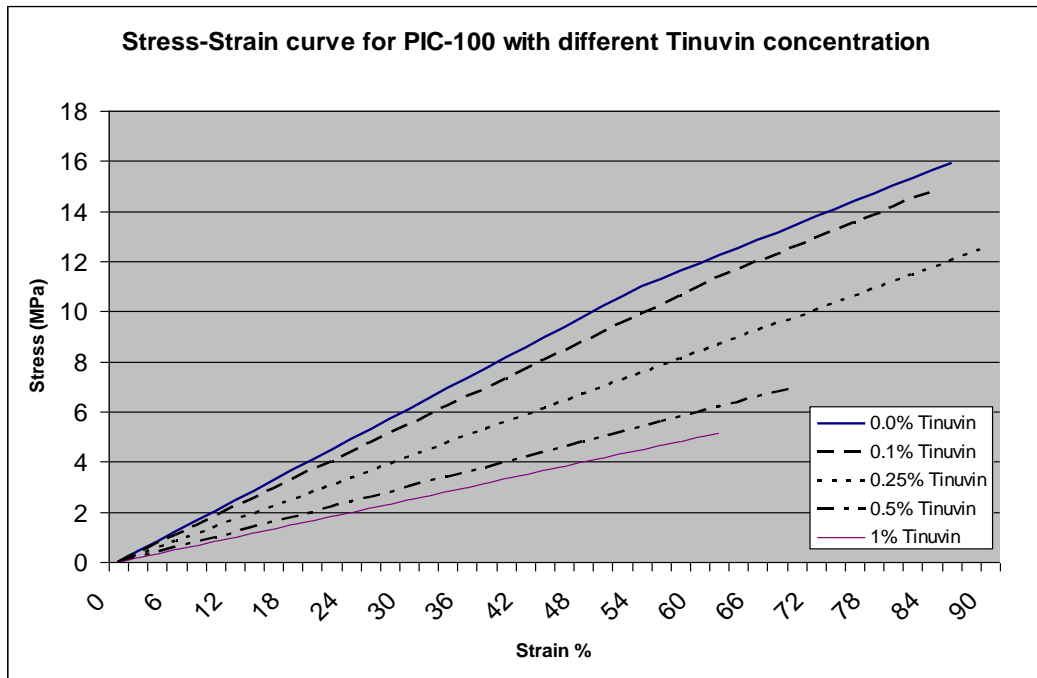


Figure 3.12 Stress-strain curves for pure PIC-100 and with different concentrations of Tinuvin (0.1, 0.25, 0.5 and 1.0 % w/w)

The results from the tensile test are summarised in Table 3.4. A well-defined trend is observed, the greater the proportion of light absorber the lower the value of tensile strength and Young's modulus. This demonstrates the importance of polymerisation for the behaviour of the compound and the consequent polymer structure for the mechanical properties of the material. The change in properties has to be considered when functional prototypes are produced or masters for micro electro-forming of Ni shims. In the latter case the peeling of the Ni replica may easily damage the master and its usage will be compromised.

As discussed in the previous paragraphs the properties of the resin-additive compound depends on the degree of polymerisation and (in the case of thermosets) the density of covalent cross-linking. The light absorber (in this case, Tinuvin) impedes the process of photo-polymerisation and affects the cross-linking density. Such deviation in structure will affect the density of the polymer and is usually detected by precise measurement of this parameter. With this motivation density measurement of the resin was performed with and without light absorber additive.

Table 3.4 Results of measurements of tensile strength and modulus of elasticity for pure PIC-100 and with different concentrations of Tinuvin (0.1, 0.25, 0.5 and 1.0 % w/w)

Tinuvin %	Tensile strength (MPa)	Young's modulus of elasticity (MPa)
0.0	16	20.3
0.1	15	18
0.25	12.2	11
0.5	7	10
1.0	5.5	8

### 3.5 Effect of Tinuvin®327 on Part Density.

The part density was determined using the pycnometer method (Lovell *et al.*, 2003). Distilled water was used, for which the density  $\rho_{H_2O}$  is 0.99978 g/cm<sup>3</sup> at 19°C – the temperature in the laboratory (Gupta, 2010). First, the pycnometer was weighed together with the part ( $m_0+m_p$ ). Then, distilled water was added and the weight  $m'_{H_2O}$  was measured (measured weight minus  $m_0+m_p$ ). Then the volume of added water  $V'_{H_2O}$  is:

$$V'_{H_2O} = \frac{m'_{H_2O}}{\rho_{H_2O}} \quad (3.2)$$

where  $m'_{H_2O}$  is the weight of added water and the volume of the measured solid part,  $V_s$  is the difference between the volume of water that fills the empty pycnometer  $V$  and volume of added water  $V'_{H_2O}$ .

$$V_s = V - V'_{H_2O} = \frac{m_{H_2O} - m'_{H_2O}}{\rho_{H_2O}} \quad (3.3)$$

Density of measured part  $\rho_s$  can be then calculated as:

$$\rho_s = \frac{m_s}{V_s} \quad (3.4)$$

Where  $m_s$  is the mass of the measured part. Three measurements were made for each sample and the maximum estimated error did not exceed 1% of the calculated value. The change in the density of the material, Fig 3.13, is in accordance with the change in the mechanical properties and confirms the hypothesis that the structural changes are induced by the photo absorber additive. More particularly the change in density of approximately 20% leads to decrease in strength and increase of resilience of more than 20% (Table 3.3). The % elongation is also significantly affected. This means that the properties of the photo-polymer

is shifted towards more 'elastomer-like' and are less appropriate for functional prototyping and micro-shims production.

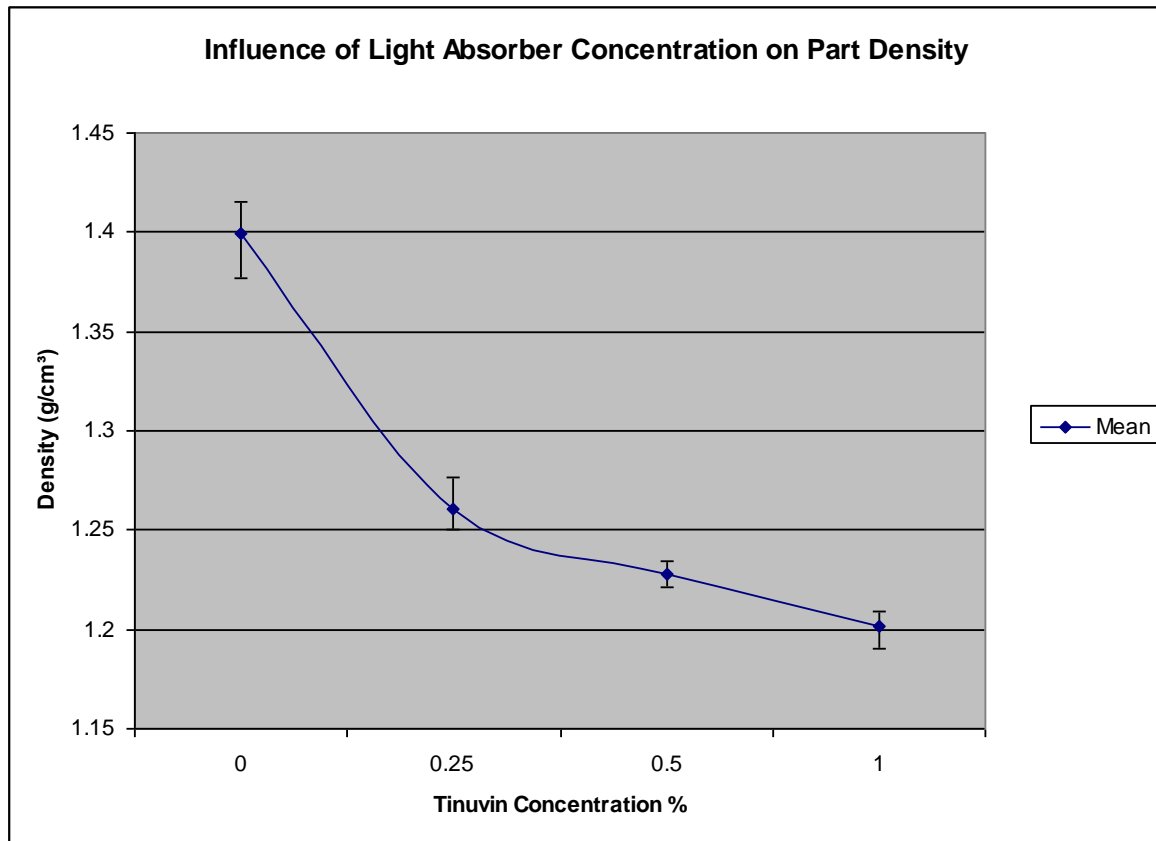


Fig. 3.13 Influence of light absorber on part density

### 3.6 Enhancing Mechanical Strength

Based on results of the cure depth investigation in Section 3.3.1, 1% Tinuvin concentration successfully reduced the cure depth of the PIC-100 resin at 6000 mJ/dm<sup>2</sup> from 140 μm to 60 μm which is an advantage in μSL because reducing cure depth helps control hanging features and helps produce more accurate parts. On the other hand, the mechanical properties strongly and adversely affected by adding 1% Tinuvin to the PIC-100 acrylate resin; the tensile strength was reduced from 16 MPa for zero Tinuvin to 5.5 MPa for the same resin with 1% Tinuvin concentration.

Jacobs (1993) has claimed that the main parameter responsible for strength is the exposure energy, and in these experiments the influence of exposure time on the mechanical properties of the part produced using PIC-100 acrylate resin with 1% Tinuvin concentration was investigated. To investigate the effect of exposure energy on the mechanical properties, tensile specimens were produced subject to different exposure times with constant irradiation of 800 mW/dm<sup>2</sup>, as shown in Table 3.4. Tensile tests were again carried out using Testometric M500 machine and D638-08 standard V type specimens at room temperature. As previously the tensile tests stretched the specimens at a constant rate of 10 mm/min.

The obtained stress strain curves, Fig 3.14, show that the tensile strength of the specimens increases as the exposure time increases which means that the tensile strength of resins containing light absorbers such as Tinuvin could be increased if subject to greater total irradiation energy. The logical reason for this behaviour is the increased degree of polymerisation and cross-linking density of the thermoset resin when extra energy is introduced to the compound. It is well-known that increasing the crosslinking density leads to an increase in the mechanical properties. However, it also moves the properties of the material from elastic towards viscoelastic (Lovell *et al.*, 2003; Pilkenton *et al.*, 2011).

Table 3.5  $\mu$ SL fabrication parameters.

Tinuvin Concentration	Exposure Time s	Irradiance $\text{mW}/\text{dm}^2$	Layer thickness $\mu\text{m}$	Tensile Strength MPa
1 %	6	800	25	4.8
	7			5.5
	8			6.2
	10			8.3

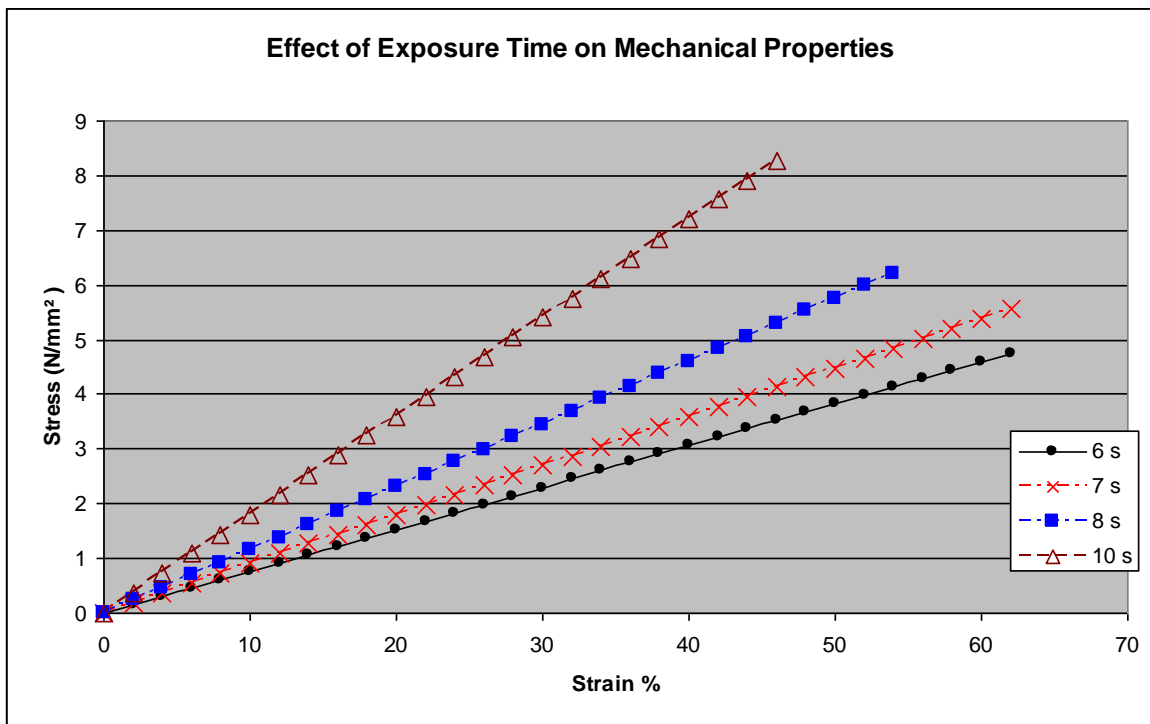


Fig. 3.14 Stress strain curves for PIC-100 with 1% Tinuvin concentration subject to different exposure times with irradiation intensity  $800 \text{ mW}/\text{dm}^2$ .

### 3.7 Summary

The results in this study categorically demonstrate the importance of even very small amounts of light absorber additive (such as Tinuvin® 327) for the structure and properties of the material. More particularly it has been shown that concentrations of 0.1-1.0 w/w% of Tinuvin® 327 change the density of the polymer by up to 20%. This indicates eventual cross-linking density reduction and leads to significant change in the mechanical properties of the material. Tensile strength was reduced and resilience was significantly increased as seen in Fig. 3.12. This has to be considered when specific functional applications of the material are envisaged. The effects of Tinuvin®327 on cure depth, critical energy, and penetration depth of green state  $\mu$ SL parts were investigated by testing five different concentrations (0.0, 0.1, 0.25, 0.5 and 1.0 % w/w) of Tinuvin®327 in PIC-100 resin, and then treated with UV light in incremental doses. The effect of variation in Tinuvin®327 concentration on cure depth and its effect on critical energy were measured. Results indicated that Tinuvin® 327 has a significant influence on cure depth, critical energy, the higher the Tinuvin concentration the lower the cure depth, and the higher the Tinuvin concentration the higher the critical energy and part shrinkage. It was found that higher Tinuvin concentrations raised the resin critical energy from 820 mJ/dm<sup>2</sup> (zero Tinuvin) to 1132 mJ/dm<sup>2</sup> (1% Tinuvin).

In an attempt to compensate for the loss in tensile strength, extra energy was introduced into the polymerisation process by incrementally increasing the exposure energy from 6s to 10s, and Fig 3.14 shows that for resin with 1% Tinuvin the strength was improved. The tests show that the resin with 1% Tinuvin concentration the tensile strength increased as the exposure time increased. The proposed reason for this behaviour is the increased degree of polymerisation and cross-linking density of the thermoset resin when additional energy was introduced to the compound.

## **Chapter 4**

### **Effects of Addition of Light Absorber on Part Accuracy**

This chapter reports the experimental work to investigate the effects of addition of Tinuvin®327 on part accuracy. The chapter starts with an introduction to green distortions and cantilever curl distortions as common accuracy problems in SL. The experimental work section starts with an investigation on the effects of addition of Tinuvin®327 on the dimensional accuracy of parts in terms of linear dimensions, form and position. After that the effect of Tinuvin on horizontal slap distortion, twin cantilever distortion, and surface roughness were investigated. At the end of the chapter, a solution is proposed to the problem of part accuracy; the introduction of a shrinkage compensation factor.

#### **4.1 Preliminaries**

Dimension accuracy is important in SL especially in  $\mu$ SL, the higher the accuracy the greater will be the demand in industry. The photopolymerisation process is the origin of the major problems with part accuracy. It is not easy to predict the final dimensions of a part after it has been exposed to UV light, because with photopolymerisation the part shrinks. The most important types of distortion are curl distortion and green creep distortion (Jacobs 1993).

Curl distortion occurs due to shrinkage of cured resin causing internal stresses. Objects that have not received adequate support are most exposed to curl distortion. If the curl distortion occurs over time it is known as creep distortion. This problem is common for acrylate-based resins. Thus far there has been no detailed investigation of the effects of addition of Tinuvin on curl distortion and dimension accuracy of the produced part.

To investigate the influence of Tinuvin®327 on the accuracy of parts in the green state this chapter examined part accuracy in terms of dimension accuracy, geometric accuracy, slab curl distortion and cantilever curl distortion. This study provides a reliable basis for the next step of reducing shrinkage and enhancing part accuracy.

#### **4.1.1 Green Distortions**

As soon as an object has been produced, but has not been post cured (subjected to additional UV energy) it is known as being in a green state and is dimensionally unstable. Green distortions are those errors that occur either during or after fabrication of the part but before the post curing process.

#### **4.1.2 Cantilever Curl Distortion**

Cantilever curl distortion factor  $C_{f6}$ , is the curl “elevation” per unit length along an unsupported beam – in this case 6 mm long, see Fig. 4.1. The cantilever curl distortion has been defined by Jacobs as:

$$C_{f6} = \frac{M_6 - M_0}{6} \times 100 \quad (4.1)$$

The curl factor,  $C_{f6}$ , is measured as a percentage, as shown in Equation 4.1, where  $M_6$  is the height of the beam measured from a specified base to the upper edge of the cantilever beam, and  $M_0$  is the corresponding undistorted height, and the “6” in the term  $C_{f6}$  refer to the 6 mm length.

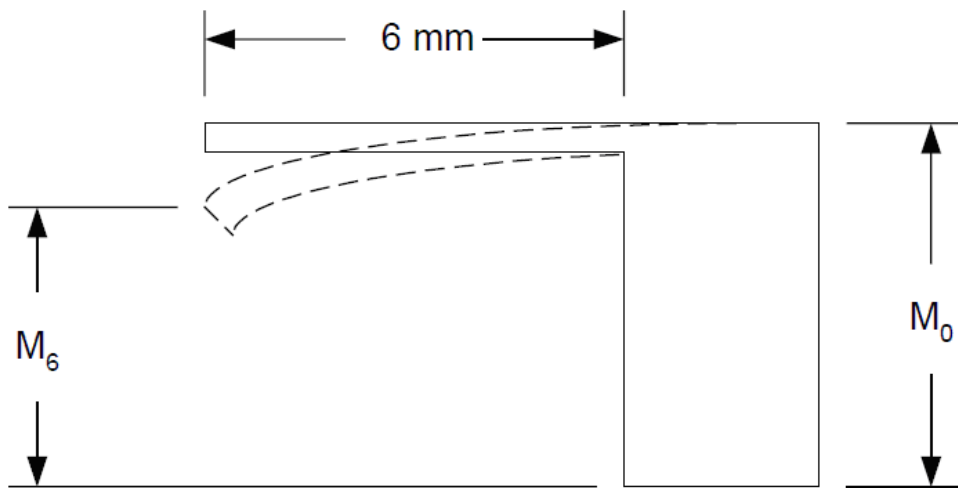


Fig 4.1 Cantilever curl distortion,  $C_{f6}$  (Jacobs, 1992)

## **4.2 Experimental Work**

The experimental work reported in this chapter used an EnvisionTEC® Mini Multi Lens machine. The pure PIC-100 resin was supplied from EnvisionTEC® and the light absorber Tinuvin®327 was supplied from Atlas Chemicals Ltd, as a fine yellow powder. This section starts with analysis of existing benchmarking parts, then a new test part was designed and fabricated and a thorough investigation conducted on the linear, form and position dimensions. Finally, the effects of Tinuvin on cantilever curl and horizontal slab distortion and part surface roughness were investigated.

### **4.2.1 Analysis of Existing Benchmarking Parts**

Several benchmarking geometries has been developed to evaluate accuracy in RP processes. Kruth (1991) and Jacobs (1992) suggested a list of characteristics for the ideal accuracy benchmark. Childs and Juster (1994) developed new benchmark geometries to replace the existing ones on the grounds that the existing benchmarks were unsuitable for micro scales accuracy investigations and that, with the exception of Jacobs (1992), all test parts were designed for evaluation of particular RP processes or machines. There is a real need for a new reliable benchmark for the  $\mu$ SL process.

### **4.2.2 Objectives of Benchmarking**

Benchmark testing is a traditional and essential way to test for all kinds of apparatus and production processes. The purpose of benchmarking can differ considerably according to the point of the study. Thus, three benchmarking procedures were introduced with the purpose of assessing the accuracy of micro part of PIC-100 acrylate resin after the addition of Tinuvin®327. These benchmarking procedures are described in following sections.

### **4.2.3 Benchmark Design**

From analysis of existing benchmarks previously mentioned, workshop experience, and to facilitate the measurement procedure, it was obvious that a single benchmark would not be capable of combining all the features being investigated. Thus, several benchmarks were used in each benchmarking procedure. In this manner the ability of the modified resin to construct microfeatures, such as holes, surfaces, cylinders and unsupported features could be assessed. Three different benchmarks were considered: Linear, Position and Geometric.

#### **4.2.3.1 Linear, Position and Geometric Dimensions Benchmarks**

Based on an extensive literature study as covered in previous section, and series of discussions with expertises in MEC lab, a conceptual design was proposed. The design of a 3D benchmark needs to characterise certain common dimensional and geometric features as well as surface roughness to evaluate  $\mu$ SL part accuracy after the addition of Tinuvin® 327.

Linear dimensions are classified according to small, medium and large distances (S, M, and L). The design benchmark, Fig 4.2, consists of a square base of  $10000\ \mu\text{m} \times 10000\ \mu\text{m} \times 2000\ \mu\text{m}$  thick. To assess accuracy of linear dimensions and ensure repeatability, four cube bosses  $2000\ \mu\text{m} \times 2000\ \mu\text{m} \times 2000\ \mu\text{m}$ , one on each corner, were added to the design. Two of these cubes were designed with positive portions and the other two cubes were designed with negative holes to assess the effect of addition of light absorber on the formation of positive and negative geometric features, and to assess the effect of Tinuvin®327 on position dimensions in terms of coaxiality. The top surface of the two portions (cube and cylinder) and the upper surface of the test part are used to measure surface roughness. In addition, the four cubes were used to assess distance measures. To structure the measurement process these

features were classified as: the Linear dimension group (XY dimensions), the Geometric (form) group, the Position group, and the surface roughness group, see Table 4.1. The dimensions assigned to individual features are all in  $\mu\text{m}$ .

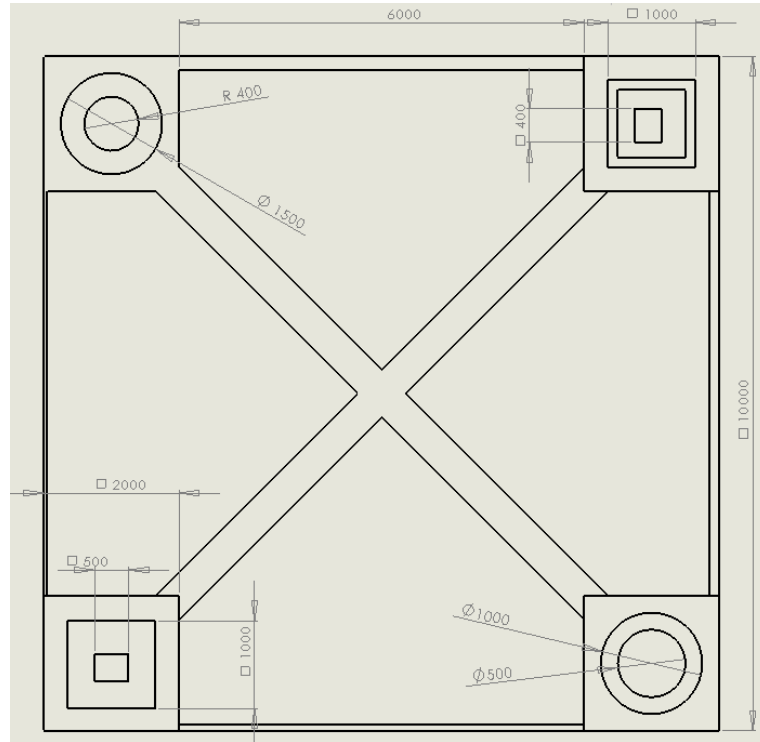


Fig. 4.2 a: The Linear, Position and Geometric Dimensions Benchmark  
(all dimensions in  $\mu\text{m}$ )

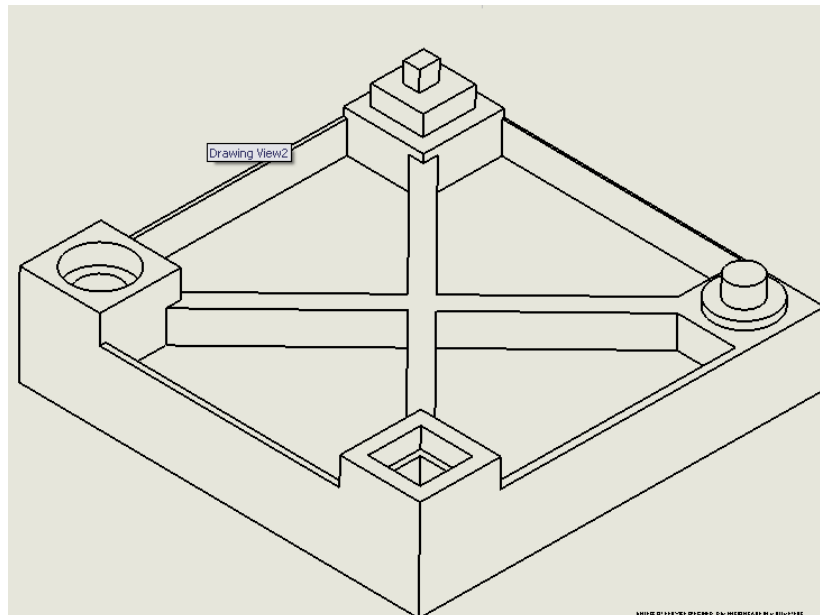


Fig. 4.2 b: Isometric view for the benchmark

Table 4.1 Dimension Groups

No	Measure	Class	Feature	Nominal Value ( $\mu\text{m}$ )
<b>Linear</b>				
1	X Dim	L	Outside X Distance	10000
2	Y Dim	L	Outside Y Distance	10000
3	X Dim	M	Distance Between cubes	6000
4	Y Dim	M	Distance Between cubes	6000
5	Y Dim	S	Large square boss length	2000
6	X Dim	S	Large square boss width	2000
7	Y Dim	S	Small square boss length	1000
8	X Dim	S	Small square boss width	1000
9	X Dim	S	Large square hole length	1000
10	Y Dim	S	Large square hole width	1000
11	X Dim	S	Small square hole length	500
12	Y Dim	S	Small square hole width	400
<b>Form</b>				
13	Circularity	Large cylinder portion		0
14	Circularity	Small cylinder portion		0
15	Circularity	Large cylinder hole		0
16	Circularity	Small cylinder hole		0
<b>Position</b>				
17	coaxiality	Centre of Large hole with small hole		0
28	coaxiality	Centre of Large cylinder with small cylinder		0
<b>Surface Roughness</b>				
29		<i>Ra</i>	top surface of the cube	0
30		<i>Ra</i>	top surface of the cylinder	0
31		<i>Ra</i>	upper surface of the test part	0

#### **4.2.3.2 Horizontal Slab Distortion Test Part**

The form of the part to be tested and its dimensions, as proposed by 3D Systems, is shown in Fig 4.3 (Jacobs 1992). The part has been modified so as to be fabricated with  $\mu$ SL for the horizontal slab distortion experiments, and so the new part is scaled to one tenth of the one proposed by 3D systems. Solid Works® software was used to model the test part with the new dimensions. The part shape offered easy handling and measuring.

#### **4.2.3.3 Twin Cantilever Distortion Test Part**

The twin cantilever test part is shown in Fig 4.4, the design was as recommended by 3D Systems and consists of a T shape of 3 mm thickness. The T test part was modelled with SolidWorks® software and the upper span was used for the cantilever distortion experiments to simulate cases where parts are designed with hanged features.

#### **4.2.4 Fabrication of Test Parts**

All test parts were fabricated by the Prefatory® machine shown in Fig. 2.9, and described in Section 2.1.3.3 (EnvisionTEC, 2008). Acrylate PIC-100 resin was polymerised with constant UV irradiance of 750 mW/dm<sup>2</sup> of 7 seconds exposure time, and 50  $\mu$ m thick layer to investigate the effect of Tinuvin®327 concentration on part accuracy. The selection of the irradiation parameters was as recommended by the resin supplier EnvisionTEC®.

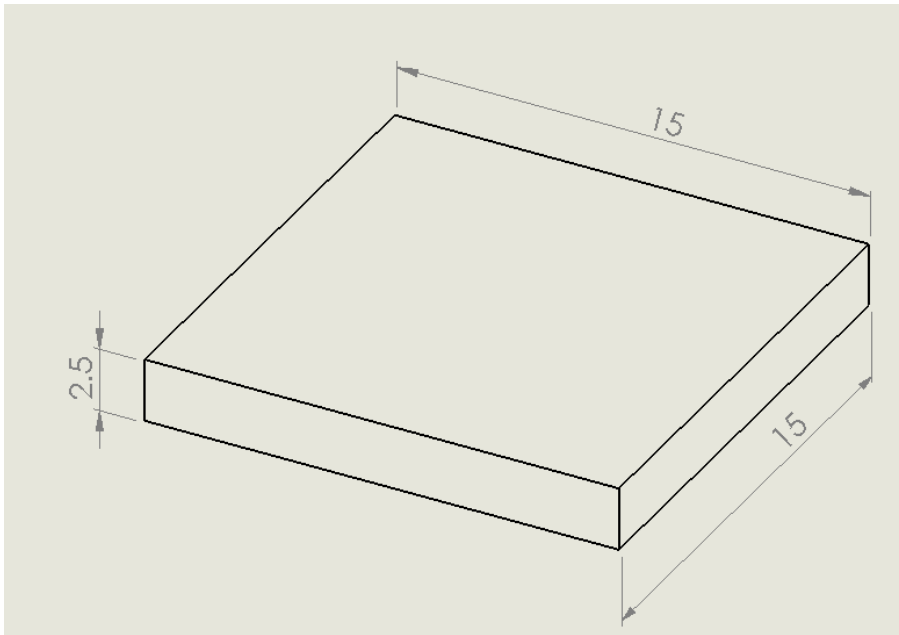


Fig. 4.3: The slab distortion test part (all dimensions in mm)

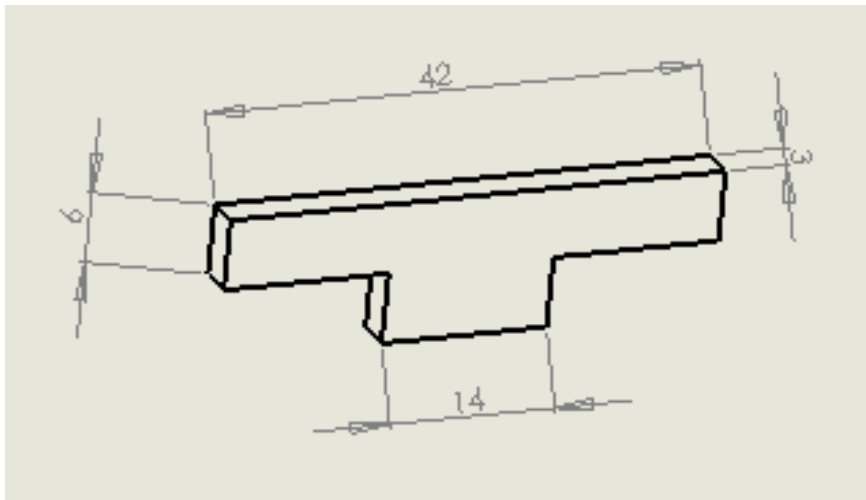


Fig. 4.4: The twin cantilever test part (all dimensions in mm)

#### 4.2.5 Number of Specimens

For an adequate sample size of test parts, fifteen samples of an evaluation box of 20mm x 15mm x 10mm were fabricated and evaluated using a QuickVision machine and measuring the differences between the CAD model and the actual part dimensions. Statistical analyses were carried out using MiniTab® version 16. The error was computed using the following equations:

$$\text{Error} = \text{Actual measurement} - \text{Specified length on 3D model} \quad (4.2)$$

The error average for dimension accuracy is shown in Fig 4.5. The figure shows that there is a number of samples where the average error becomes independent of sample size. It can be seen that after six samples the gradient of the average error curve becomes insignificant or zero. Hence, the sample size in all tests carried in this research was eight.

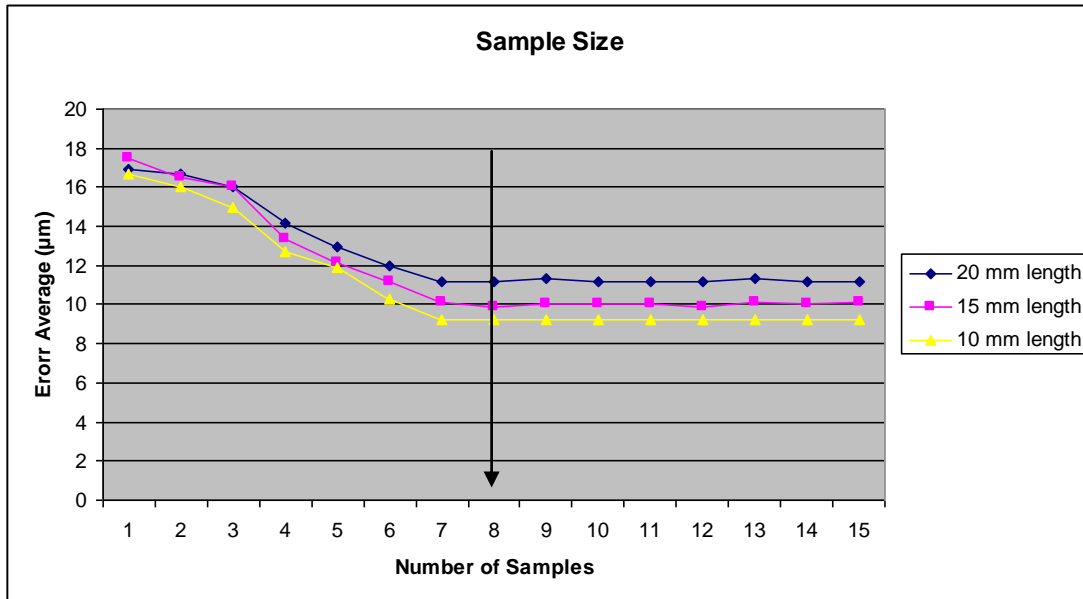


Fig. 4.5: The error average for dimension accuracy.

## 4.2.6 Measurements

To reduce human error associated with the measuring procedure and to better assure measurement precision, all linear, position and flatness measurements were made using the QuickVision® Machine, Fig 4.6, which is a dependable, high performance inspection device with high-speed control capabilities. The quoted accuracy of the QuickVision® machine system is  $\pm 2\mu\text{m}$  for the size of measurement used in this research (Mitutoyo, 2010).

### 4.2.6.1 Measurement Uncertainty

To minimise the measurement error, all the measurements were taken under the maximum magnification allowed by the QuickVison® (CMM) software. However, it was still necessary to calculate the measurement uncertainty associated with the measurement procedure used to inspect the microfeatures. This assessment was carried out using an existing method for calculating uncertainty (Kirkup and Frenkel, 2006). It was assumed that the sources of uncertainty in inspecting the microfeatures were the same for all measurements. The formula for calculating the standard uncertainty,  $u$ , is:

$$u = \frac{s}{\sqrt{n}} \quad (4.3)$$

Where  $s$  is the estimated standard deviation (see below) and  $n$  is the number of measurements in the set. To carry out this assessment and minimise the data used, only eight data points were taken for each dimension, the lowest ( $1000\mu\text{m}$ ), the highest ( $10000\mu\text{m}$ ), and one in between ( $2000\mu\text{m}$ ) from the benchmark features. Table 4.2 shows the results of these measurements. For the dimension with measured mean values of  $9976\mu\text{m}$ ,  $1987\mu\text{m}$  and  $975\mu\text{m}$ , the estimated standard deviations,  $s$ , were calculated to be  $9.1\mu\text{m}$ ,  $6.1\mu\text{m}$  and  $4.1\mu\text{m}$  respectively while the corresponding standard measurement uncertainties were  $3.7\mu\text{m}$ ,  $2.1$

$\mu\text{m}$  and  $1.6 \mu\text{m}$ . There was an inverse relationship between the measurement uncertainty and the nominal dimensions. It was determined that the maximum measurement uncertainty was  $3.7 \mu\text{m}$  for the  $10000 \mu\text{m}$  dimension and this was considered acceptable for this study.

#### **4.2.6.2 Linear Dimension Measurement**

In order to accurately measure distances in the X-Y dimension, eight specimens from each Tinuvin®327 concentration were used. The specimens were visually inspected carefully to ensure they were free from any deformation or damage. The specimens were then positioned individually on the CMM table so that X-Y plane was perpendicular to the CMM lens, see Fig 4.6. To minimise error, the maximum magnification of the machine was used. Twenty points were carefully selected on every measured edge and six linear measurements were made between edges for each of eight samples, and the mean, standard deviation and range were determined for the error.

Table 4.2: Results of measurement uncertainty.

Nominal Dimension <i>mm</i>	Measured Dimension <i>mm</i>	Std dev <i>mm</i>	u <i>mm</i>
10000	9976	9.1	3.7
2000	1987	6.1	2.1
1000	975	4.1	1.6



Fig. 4.6 a: QuickVision® Coordinate Measuring Machine (CMM)

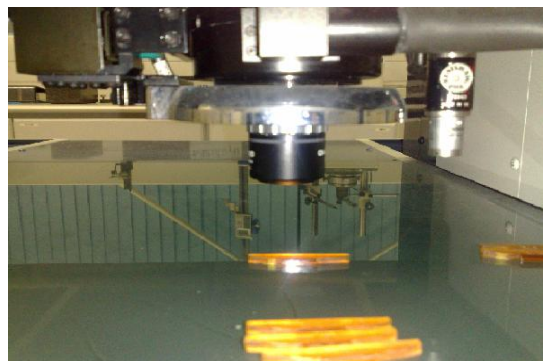


Fig. 4.6 b: Position of test part on QuickVision® (CMM) table

#### **4.2.6.3 Measurement of Circularity Errors**

Circularity errors are geometric tolerances that describe by how much a circular feature deviates from a perfect circle. According to ISO 1101 (ISO 1101, 1983) circularity error is the difference in radii between two concentric circles separated by the minimum possible distance and containing all the measurement points on the given profile, as illustrated in Fig 4.7 (Jensen, 2011). Circularity errors were measured by QuickVision CMM machine by touching the out side of the cylinder in at less three points while fixing the Z movement of the prop, then the software calculate the error in circularity.

#### **4.2.6.4 Cantilever Curl distortion Measurement**

To measure the curl distortion, eight sample twin cantilever parts were taken for every Tinuvin concentration with same layer thickness 25 $\mu$ m. The parts were measured in green state, using the QuickVision CMM. The measurements were repeated three times for every millimetre along the unsupported lengths of the cantilever from both sides. The average value of the three measurements at each point was taken and plotted as a function of distance along the cantilever. The curl factor,  $C_{f6}$ , was found using Equation 4.1. The results for the curl factor and the twin cantilever curl factor were plotted as a function of cantilever length and are presented below in Section 4.3, Results and Discussion.

#### **4.2.6.5 Flatness Measurement**

Using the QuickVision CMM machine, four measurements were taken for this diagnostic test: Green as-built distortion (attached), Green as soon as part removed from plate (Not-attached), one day creep distortion and one week creep distortion. First, the test part was

measured while still attached to the platform to measure as-built distortion. Second, the test part was removed from the platform and measured for any curl distortion accruing after removal from the platform. One day later the part was measured for a third time, and one week later was measured for a fourth time to measure the distortion occurred due gradually with.

The maximum distortion was assessed by taking measurements at 120 point evenly distributed over the top surface of the test part. The software then calculated the variation in the Z direction from the pre-defined X-Y plane. Here the flatness zone is the width of the zone defined by the two closest parallel planes that bound the data points (Puncochar. 1997).

#### **4.2.6.6 Surface Roughness Measurement**

To assess the influence of Tinuvin®327 on surface roughness of the test part, surface roughness was measured using a scanning white light interferometer, Micro-XAM from Phase Shift Inc., with a 12.5X optical magnification, see Fig. 4.8. The average surface roughness,  $R_a$ , was measured for each part. For surface roughness in Y-Z plane (building direction), the measuring direction was  $45^\circ$  in relation to the build direction of the test part, because conducting measurements in a direction parallel to the stair steps would result in too low roughness values whilst measurements in a direction perpendicular to the stair steps would result in too high roughness values.

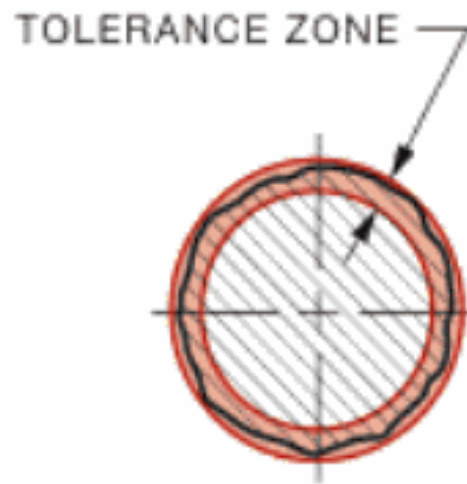


Fig. 4.7 Circularity error measurement (Jensen, 2011)



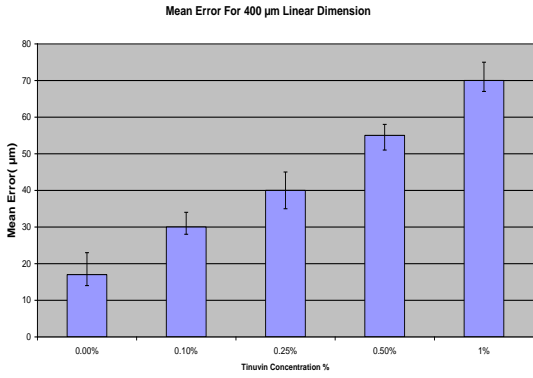
Fig. 4.8 White light interferometer, Micro-XAM from Phase.

## 4.3 Results and Discussion

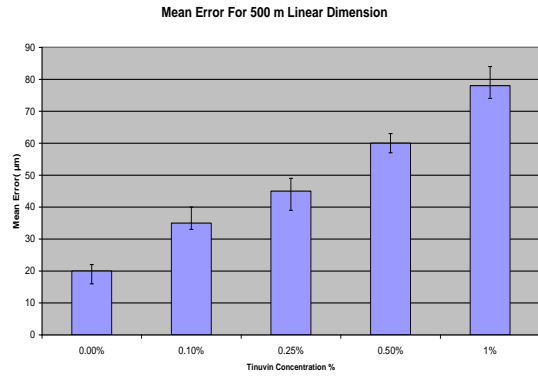
### 4.3.1 Linear Dimensions Error

Fig. 4.9 shows that addition of Tinuvin®327 has a significant effect on dimensional accuracy, for all the tests the greater the concentration of added Tinuvin®327, and the greater the length of the sample, the greater the error. For the 400 and 500  $\mu\text{m}$  linear dimensions the mean error ranged from 20  $\mu\text{m}$  or less for zero Tinuvin to 78  $\mu\text{m}$  with 1% Tinuvin concentration. For the 1000 and 2000  $\mu\text{m}$  linear dimensions the mean error ranged from 25  $\mu\text{m}$  for zero Tinuvin to 96  $\mu\text{m}$  with 1% Tinuvin concentration, and for the 6000 and 10000  $\mu\text{m}$  linear dimensions the mean error ranged from 30  $\mu\text{m}$  for zero Tinuvin to 180  $\mu\text{m}$  with 1% Tinuvin concentration.

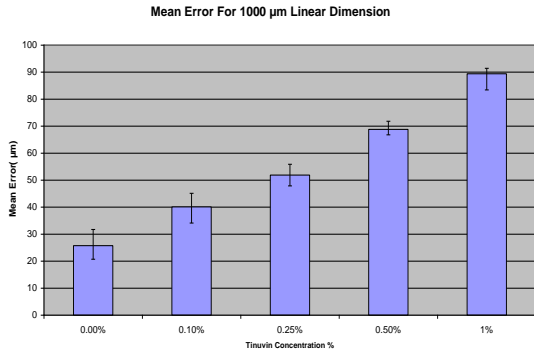
Fig. 4.10 presents the data in terms of % Tinuvin®327 concentration, and it is immediately obvious that increase in the added Tinuvin®327 increased the mean error due to the increased shrinkage associated with adding Tinuvin® 327 to the acrylate resin due to the reduction in the degree of polymerisation and cross-linking density of the thermoset resin when light absorber is introduced into the compound (Pilkenton 2011).



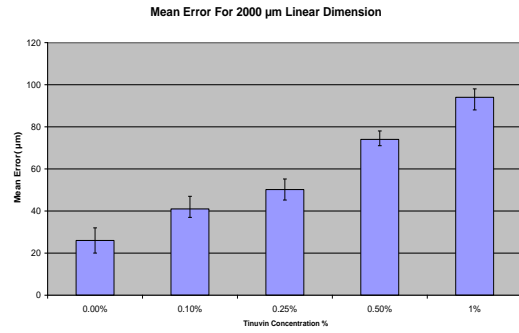
a) Mean error for 400 mm linear dimension.



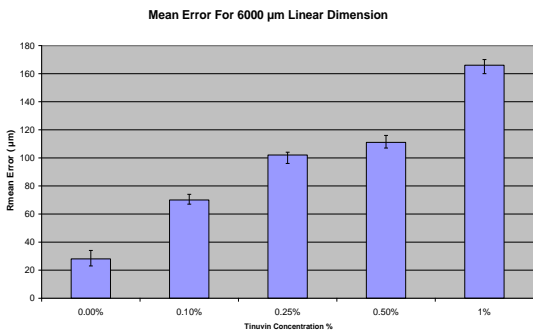
b) Mean error for 500 mm linear dimension.



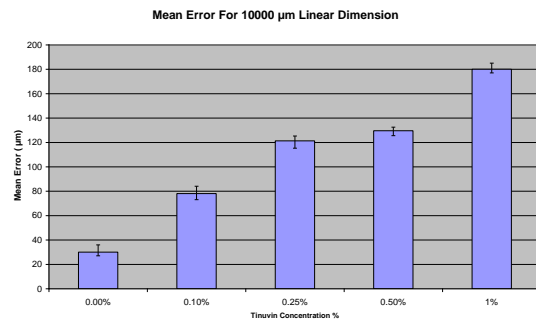
c) Mean error for 1000 mm linear dimension.



d) Mean error for 2000 mm linear dimension.



e) Mean error for 6000 mm linear dimension.



f) Mean error for 10000 mm linear dimension

Fig. 4.9: The effect of Tinuvin®327 concentration on the linear dimensions

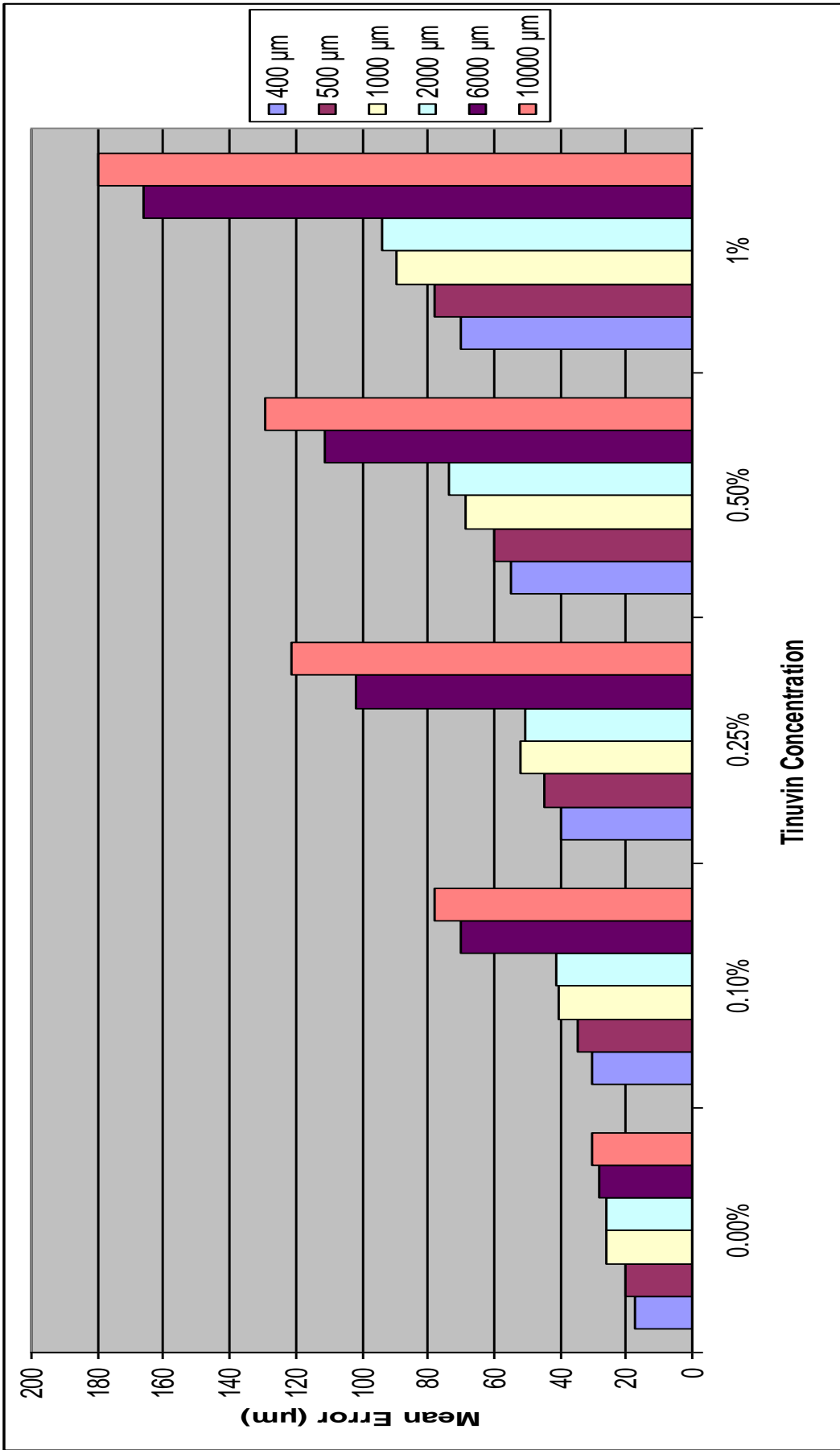


Fig 4.10: comparison of the effect of Tinuvin®327 concentration on the linear dimension.

### 4.3.2 Circularity and Position Error

The results for circularity and position measurement mean errors are shown in Figs 4.11, 4.12 and 4.13. The mean circularity error for Tinuvin concentrations of 0.0, 0.1, and 0.25 % ranges between 19 and 22  $\mu\text{m}$ , which increases to 55  $\mu\text{m}$  at 1% concentration. For position error the minimum mean error was 6 $\mu\text{m}$  for 0% Tinuvin concentration and a maximum mean error of 16  $\mu\text{m}$  for 1.0% Tinuvin. Below 0.25% concentration, change in the Tinuvin@327 concentration causes no significant change in roundness or position error, **Fig 4.13** shows measured micro cylinders.

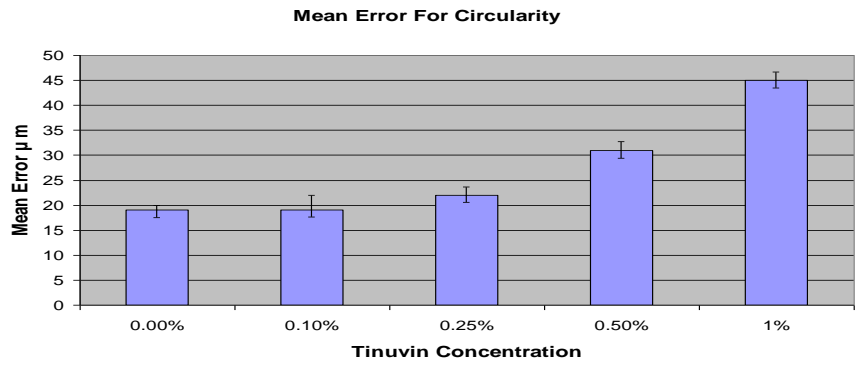


Fig. 4.11: Circularity measurement errors

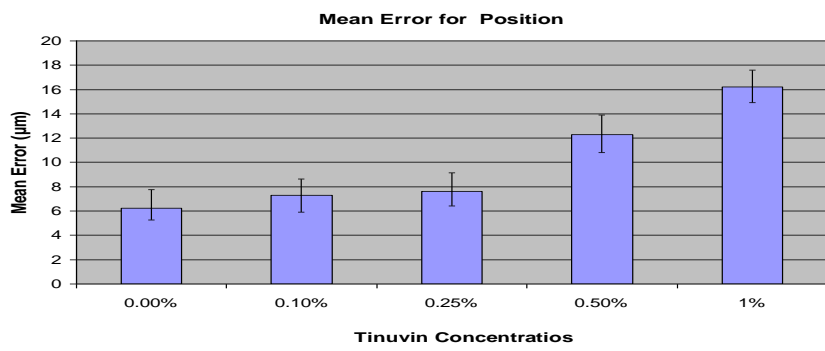


Fig. 4.12: Position measurement errors

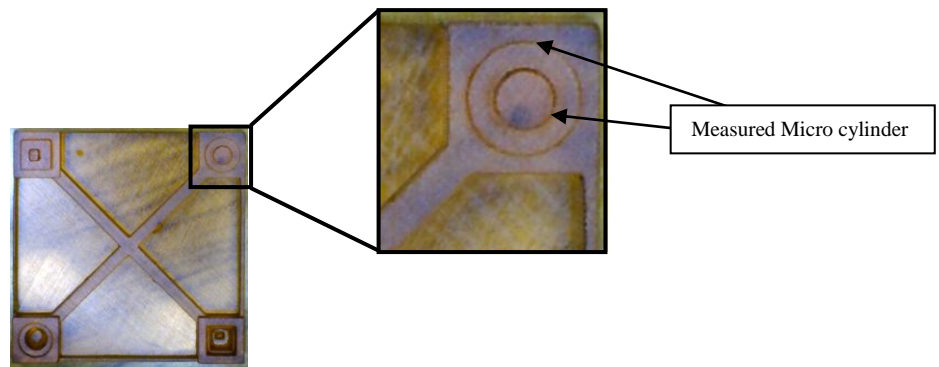


Fig. 4.13: Measured micro cylinders

### 4.3.3 Cantilever Curl Distortion

When a hanged feature is being created, a fresh layer is solidified without any contact with supports. The second layer adheres to the earlier solidified layer. The polymerisation shrinkage of the new layer is transmitted to the previously solidified layer causing its free end to curl upwards, see Fig. 4.14. As a result the final part is distorted in a complex manner depending on the nature of the resin (Venuvindo, *et al.*, 2004).

Fig. 4.15 shows the variation of the elevation ( $\Delta Z$ ) along the span of the cantilever for different concentrations of Tinuvin. It can be observed that the values of  $\Delta Z$ , and the corresponding cantilever curl distortion, increase with increase in Tinuvin concentration. The increase in curl distortion is due to the shrinkage induced by the presence of Tinuvin (Bugada, *et al.*, 1995). It is obvious that the when a later layer adheres to an earlier solidified layer, polymerisation shrinkage of the new layer is transmitted to the previous layer causing it to curl upwards.

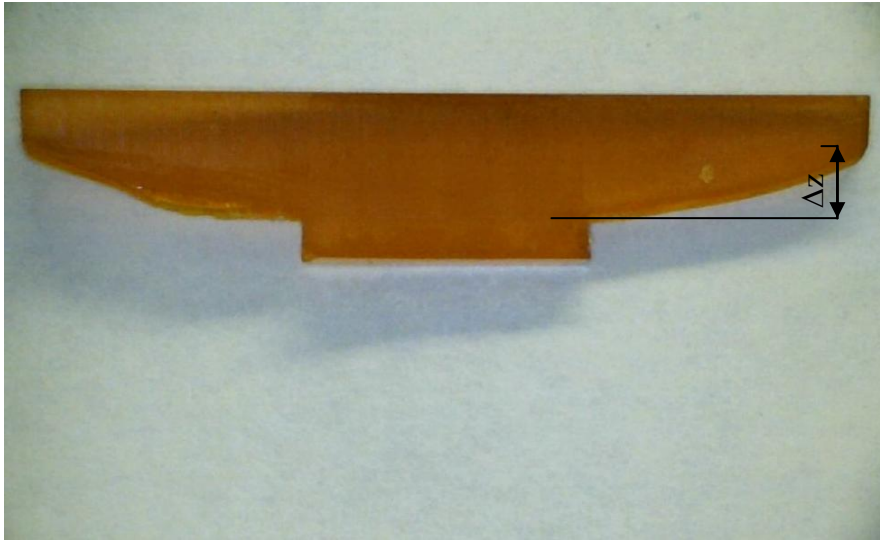


Fig. 4.14: Upwards curl of free end

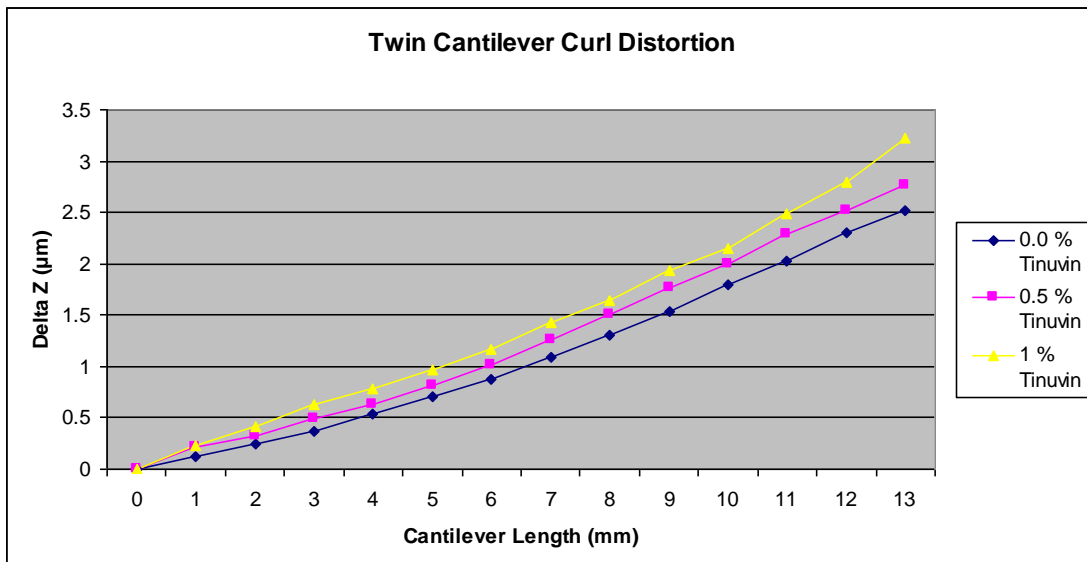


Fig. 4.15: Variation of the elevation ( $\Delta Z$ ) along the span of the cantilever

#### **4.3.4 Horizontal Slab Distortion**

In horizontal slab distortion, the distortion was assessed using the Quick Vision CMM on the upper surface of the test part, as shown in Figs 4.15 and 16. The maximum difference in readings occurs between the corners and the centre of the slab. Fig. 4.17 shows the result of the flatness test for five different Tinuvin concentrations (0.0, 0.1, 0.25, 0.5 and 1.0 % w/w) and it can be seen that the presence of Tinuvin has a significant influence on part flatness. It is also clear that distortion increased as the Tinuvin concentration increased.

When part is released from the platform and distortion measured immediately the distortion increased for all five values of Tinuvin. In the case of 1% Tinuvin the increase was from 0.25 mm to 0.6 mm. At this stage, the influence of Tinuvin is not yet strong probably because the influence of the adhesion force has had little effect on the part.

One day later, curing is advancing and it is clear that the presence of Tinuvin has a much greater influence on part flatness and the distortion has increases dramatically. After one week the shrinkage is more or less complete and maximum distortion is reached. The maximum distortion was measured as 2.7 mm with 1% Tinuvin concentration after one week. The distortion is due to the internal stress induced by shrinkage which increases with the proportion of Tinuvin is added.

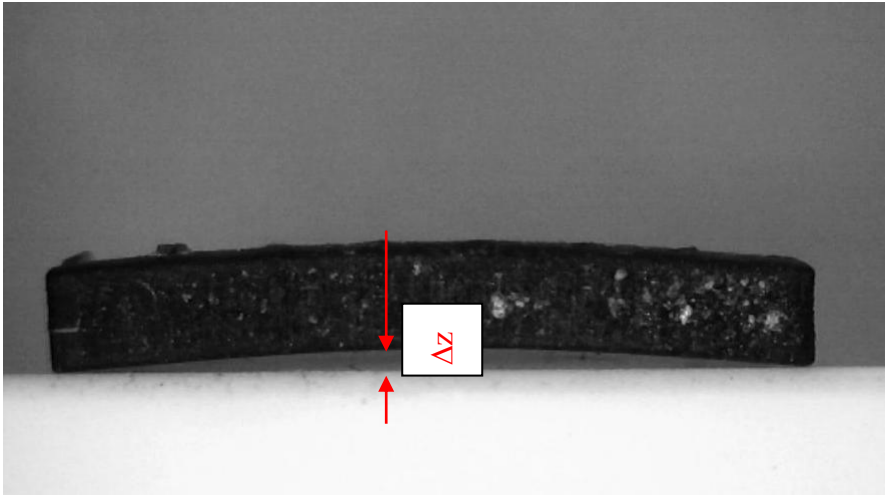


Fig. 4.16: Part flatness test

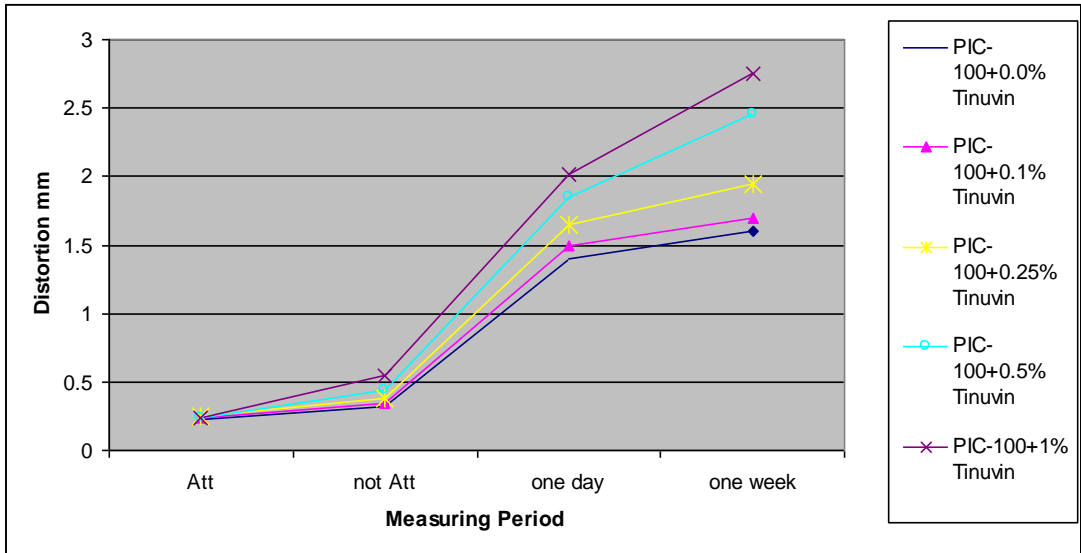


Fig. 4.17: Flatness test results Where, Att =Attached” and “not Att=not Attached

### 4.3.5 Surface Roughness

Fig. 4.18 shows average surface roughness,  $Ra$ , for the measured surface. In the X-Y plane the average surface roughness coefficient increased from  $0.53\mu\text{m}$  at 0.0% Tinuvin concentration to  $0.75\mu\text{m}$  at 1% Tinuvin concentration. In the Y-Z plane, Fig. 4.19, (layer thickness direction) the average surface roughness increased from  $2.25\mu\text{m}$  for zero added Tinuvin to  $3.35\mu\text{m}$  for 1% Tinuvin concentration.

### 4.3.6 Test of Significance

To assess whether the differences in mean surface roughnesses were significant a T-test was carried out using MiniTab 2010 software. In this test the software considering two hypotheses: null Hypothesis  $H_0$  where  $\mu_1 - \mu_2 = 0$  and the alternative Hypothesis  $H_1$  where  $\mu_1 - \mu_2 \neq 0$ . Then the software tests  $H_0$  against  $H_1$  for chosen  $\alpha$  level, where  $\alpha$  is user-defined level of significant. If the p-value, the smallest level of significance that would lead to rejection of the null hypothesis is below the  $\alpha$  level (which in this case has been chosen as 0.05 as this is a level commonly used), then  $H_0$  is probably wrong, the null hypothesis is rejected and it can be concluded that the difference is significant. The results in Tables 4.3 and 4.4 show that the p-value for both the X-Y and Y-Z planes is 0.000 which means the null hypothesis should be rejected and it should be accepted that Tinuvin has a significant effect on surface roughness (Montgomery 2011).

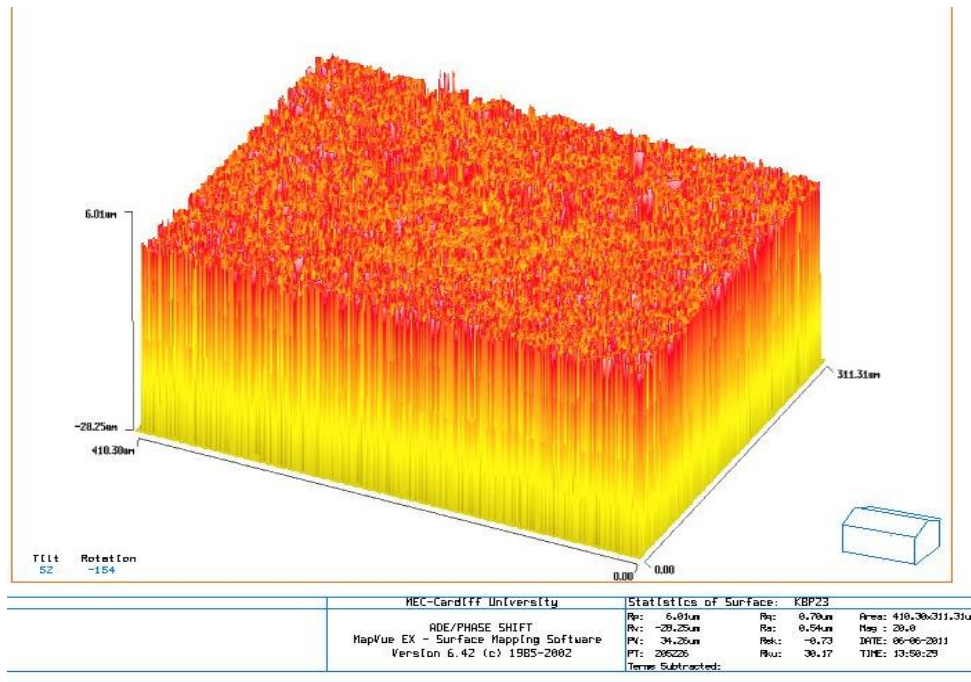


Fig. 4.18-a: Average surface roughness in X-Y Plane =  $0.54\mu\text{m}$  at 0.0% Tinuvin concentration

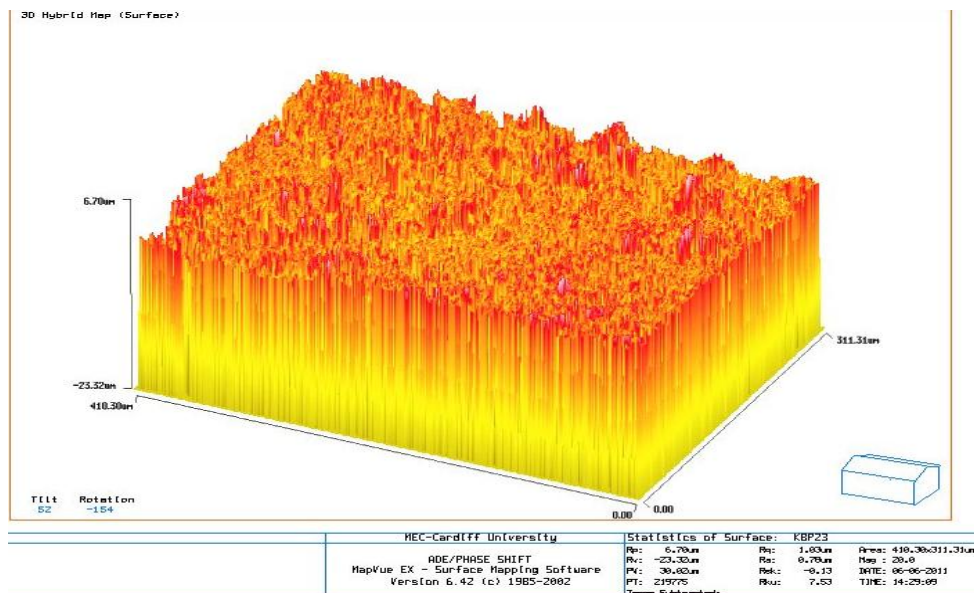


Fig. 4.18-b: Average surface roughness in X-Y Plane =  $0.75\mu\text{m}$  at 1% Tinuvin concentration

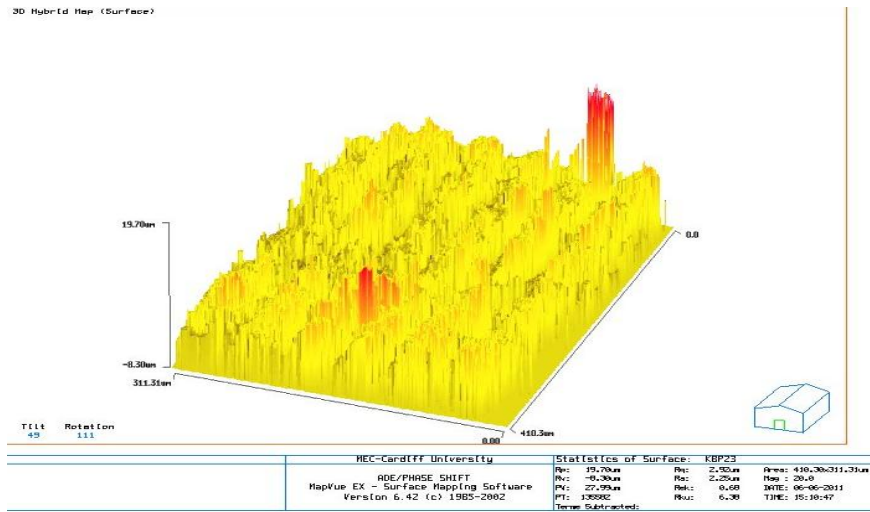


Fig. 4.19 a: Average surface roughness in Y-Z Plane = 2.25 $\mu$ m at 0.0% Tinuvin concentration

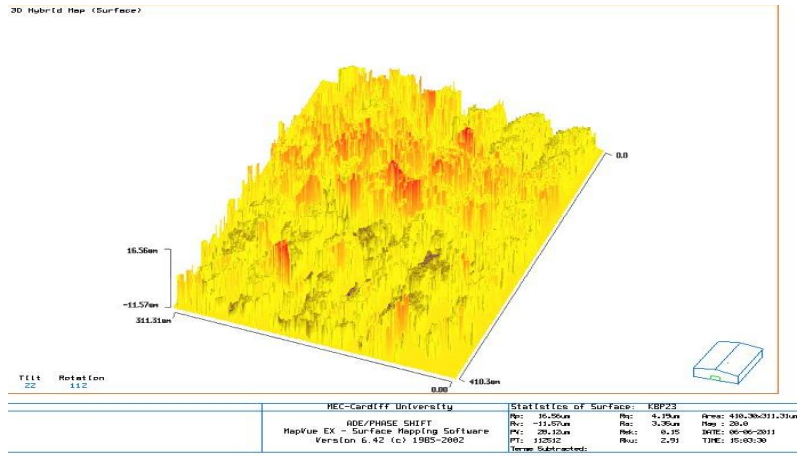


Fig. 4.19 b: Average surface roughness in Y-Z Plane = 3.35 $\mu$ m at 1% Tinuvin concentration

Table 4.3 Results of two sample test of significance for X-Y plane

Sample	N	Mean	StD	SE Mean
0.0%	6	0.53	0.0175	0.0071
1%	6	0.75	0.0172	0.0070
$\alpha = 0.05$		Estimate for difference: 0.2216	DF = 9	P-Value = 0.000
T-Value = 27.08		95% lower bound for difference: 0.1989		

Table 4.4 Results of two sample test of significance for Y-Z plane

Sample	N	Mean	StD	SE Mean
0.0%	6	3.3467	0.0361	0.015
1%	6	2.2600	0.0482	0.020
$\alpha = 0.05$		Estimate for difference: 1.0867	DF = 9	P-Value = 0.000
T-Value = 42.17		95% lower bound for difference: 1.0416		

#### **4.4 Effect of Tinuvin®327 on Green Part Shrinkage**

From the above results, one can conclude that Tinuvin®327 was a major factor contributing to undesired loss in part accuracy due to induced shrinkage. Thus an investigation of shrinkage induced by Tinuvin®327, and development of a possible shrinkage compensation factor (SCF) to overcome the changes which occur in the resin after the addition of Tinuvin®327 as a light absorber is important. The SCF and Christmas Tree Test are discussed in detail in the following section.

##### **4.4.1 Shrinkage Compensation Factor and Christmas Tree Test**

In order to study the relationship between Tinuvin®327 concentration and part shrinkage, a Christmas Tree diagnostic test from 3D systems was conducted using PIC-100 resin with different Tinuvin® 327 concentrations (0.0, 0.1, 0.5 and 1.0 %w/w). The test part consists of six slabs with X and Y dimensions which would fit in the EnvisionTEC machine, see Fig. 4.20. A simple 3D model of a Christmas Tree test part was designed using SolidWorks® software and fabricated using Mini Multi Lens Prefatory® machine from EnvisionTEC® described in Section 2.1.3.3 (EnvisionTEC 2008). The tree was a 50 µm thick layer of acrylate PIC-100 resin was polymerised with constant UV irradiance of 750 mW/dm<sup>2</sup> and 7 seconds exposure time.

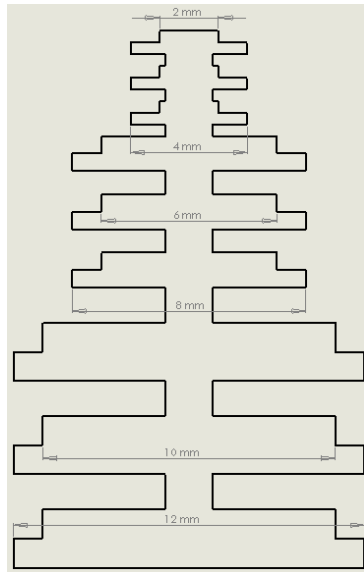


Fig. 4.20 Christmas Tree test part design



Fig. 4.21 Christmas tree test part after fabrication

Sixteen test parts were fabricated for each Tinuvin®327 concentration; eight aligned in the X direction, and eight in the Y direction. The completed test parts, see Fig. 4.21, were placed in an ultrasonic bath for two minutes to clean the part of non-polymerised resin, the parts were then further cleaned with isopropan solution and dried in ventilated incubator for 30 minutes at 37°C (EnvisionTEC, 2008). After that the X and Y dimensions of the parts were measured using the QuickVision® CMM machine. The PERFACTORY® machine does not have full control in the Z direction, its movement in the Z direction is restricted by a motor step, thus the shrinkage of the test part in the Z direction was not investigated here.

#### **4.4.2 Error and Measurement**

After careful visual inspection, the specimens were individually positioned on the QuickVision CMM table. All measurements were taken by single examiner. To minimise intra-examiner variation six readings of each linear measurements were taken and the mean value then calculated (so 6 reading for each of 8 samples = 48 readings). Statistical analyses were carried out using the MiniTab® version 16. The error was computed using Equation 4.3.

#### **4.4.3 Shrinkage Results**

The results shown in Figs 4.22 and 4.23 clearly demonstrates a strong relationship between Tinuvin concentration and shrinkage, the higher the Tinuvin concentration the higher the shrinkage. It is obvious that the presence of light absorber significantly increased the shrinkage of the material because of the reduced degree of polymerisation and cross-linking density of the thermoset resin when light absorber is introduced into the compound. It is also clear that no significant differences in shrinkage in X and Y direction and this is because the chain formation are equal in X and Y, however, for more accurate parts, shrinkage factors in X and Y directions is requested .It is well known that lowering the crosslinking density leads

to lowering the bulk mechanical properties (Pilkenton 2011). These changes in the material structure change the material's resilience and so it responds more extensively (after removal of supports) to the shrinkage stresses induced by the interaction between the polymerised material and the base.

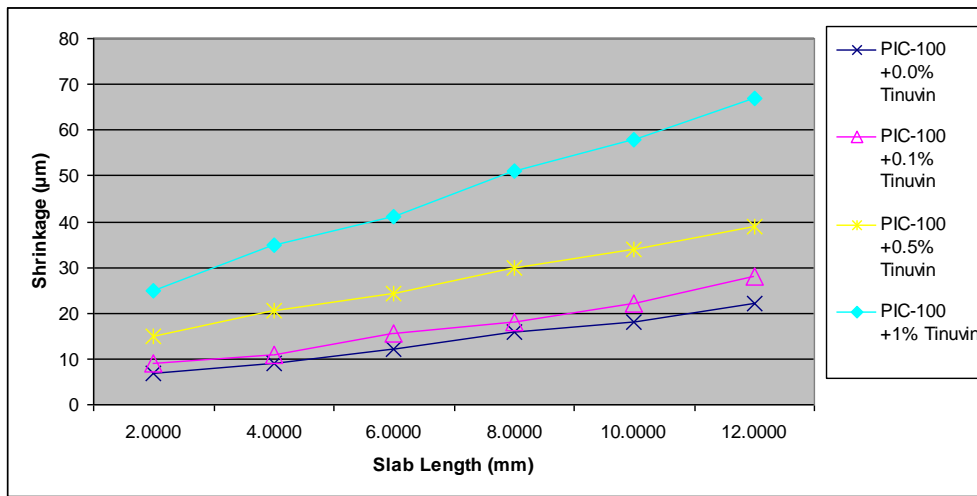


Fig. 4.22 Effect of Tinuvin concentration on test part shrinkage in X direction

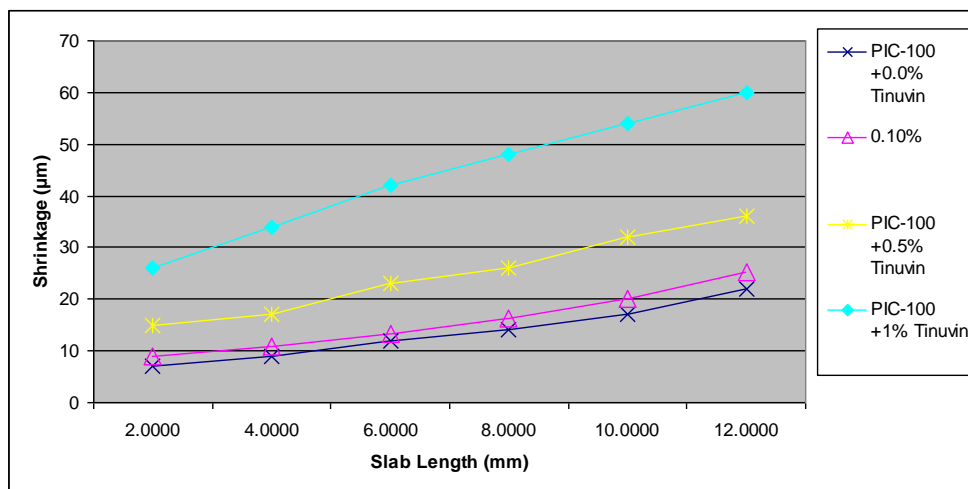


Fig. 4.23 Effect of Tinuvin concentration on test part shrinkage in Y direction

Table 4.5 Results of shrinkage of Christmas Tree test

Tinuvín Concentration	Shrinkage in X Direction	Shrinkage in Y Direction	SCF	
			X	Y
0.0%	$y = 0.00303X + 3.40$	$y = 0.00289X + 3.40$	1.00303	1.00288
0.1%	$y = 0.00318X + 3.6$	$y = 0.00375X + 4.24$	1.00318	1.00374
0.5%	$y = 0.00473X + 10.61$	$y = 0.00437X + 9.53$	1.00471	1.00437
1.0%	$y = 0.00814X + 18.25$	$y = 0.00674X + 20.40$	1.00842	1.00674

#### 4.4.4 Shrinkage Compensation Factor

In order to overcome problems caused by the shrinkage induced by the presence of Tinuvin, a compensation factor (SCF) was applied. A straight line was fitted to the points plotted in Figs 4.22 and 4.23, and the SCF is equal to  $(1 + \text{the gradient of the line})$  (Tang 2004), see Table 4.5. The SCF was input into the Perfactory software, and all dimensions of the designed parts were compensated before polymerisation started, thus the parts built by direct  $\mu$ SL should have the desired accuracy.

An experiment was carried out to build the same part as shown in Fig. 4.2 using the SCFs in Table 4.5. Sixteen parts were fabricated using PIC-100 resin with the five Tinuvin®327 concentrations as previously, using the SCF (eight in the X direction and eight in the Y direction). The model part built by Perfactory® machine is shown in Fig. 4.27.

Fig. 4.24 shows the results of using the SCF on mean error for the linear dimensions. Direct comparison can be made with Fig. 4.10 and it is immediately obvious that there has been a considerable improvement in part accuracy. As expected the improvement is proportional to the amount of Tinuvin® 327 added to the resin, but at 0.0% Tinuvin the error is half that without using the SCF and at 1% Tinuvin the error less than one third that without using the SCF.

Fig. 4.25 shows the results of using the SCF on mean error for the circularity errors and can be compared directly with Fig. 4.11. The mean errors are reduced at every Tinuvin concentration typically by about a half; less at zero concentration more at 1%. Fig. 4.26 shows the results of using the SCF on position error and can be compared directly with Fig. 4.12. The errors are reduced at every Tinuvin concentration but not by as much as for either the linear dimension or position errors.

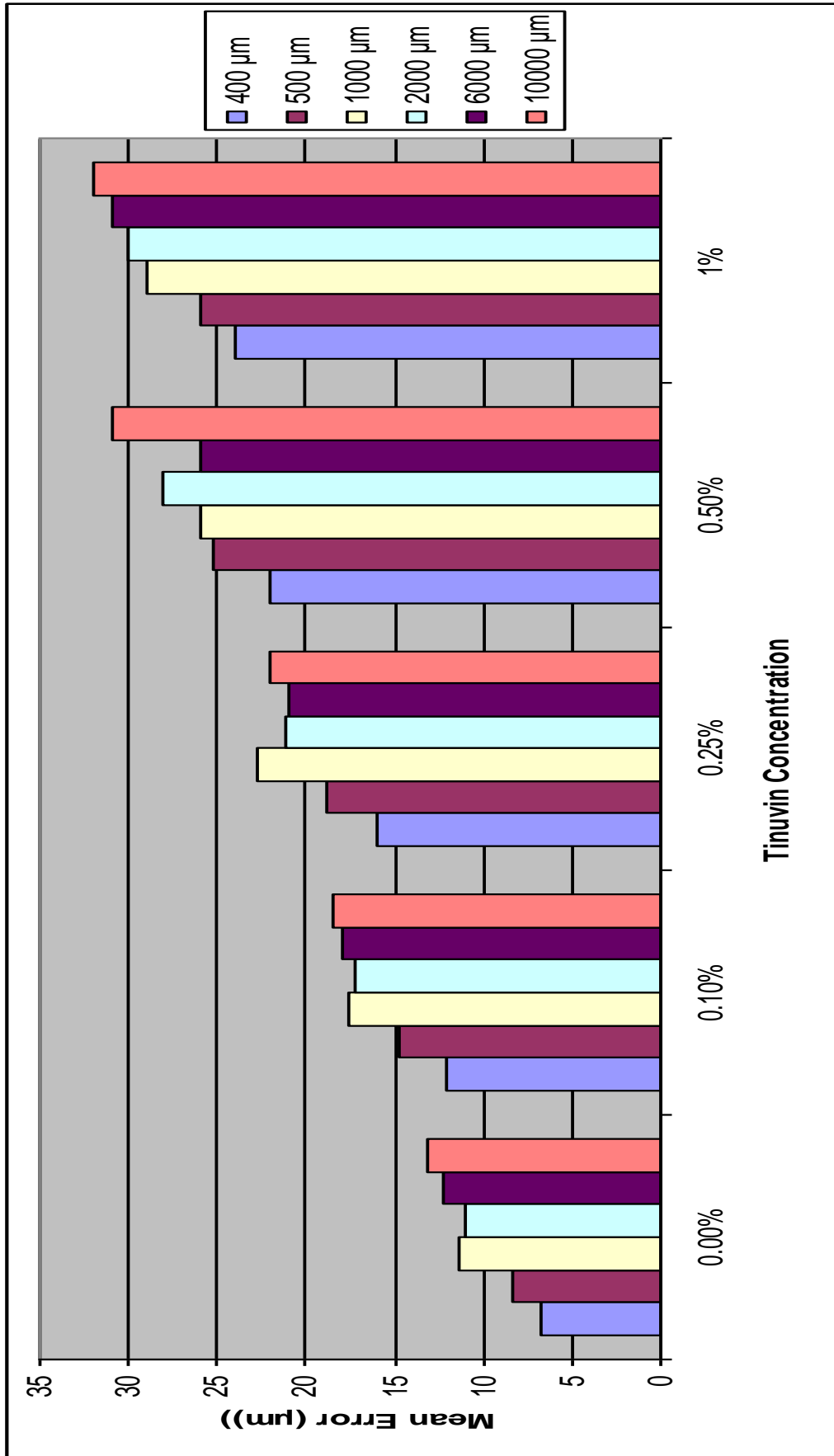


Fig 4.24 Results of shrinkage compensation factor in linear dimensions.

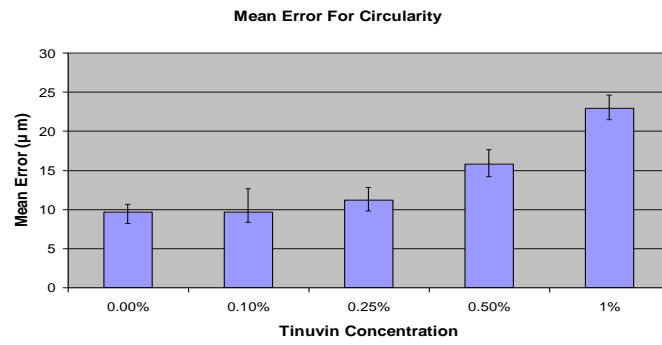


Fig. 4.25 Results for circularity errors after using SCF

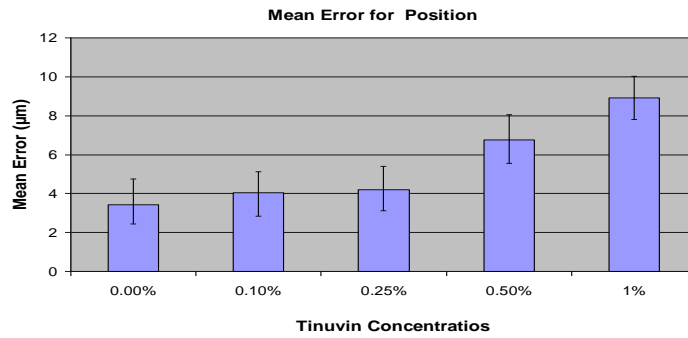


Fig. 4.26 Results for position errors after using SCF

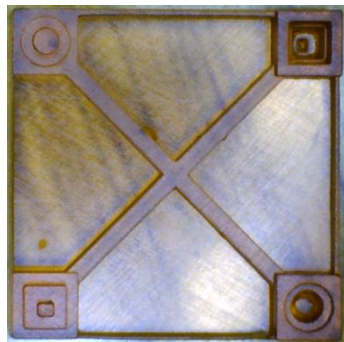


Fig. 4.27: Test part built using Shrinkage Compensation Factor

## 4.5 Summary

This chapter has investigated the effect of Tinuvin®327 concentration on part accuracy in  $\mu$ SL. PIC-100 acrylate resin with different Tinuvin concentrations was used to study the relationship between light absorber concentration and part accuracy in terms of linear dimensions, form, and position. All solidification processes in this chapter were conducted using a Mini Multi Lens Perfactory® machine. Results show that Tinuvin®327 has significant effect on dimension accuracy. For linear dimensions the error increased with length of part and amount of Tinuvin added, due to the shrinkage associated with adding Tinuvin® 327 to acrylate resin. Tinuvin®327 has no significant effect on either roundness and position error when the concentration was less than 0.25% but the error becomes obvious at 0.5% Tinuvin concentration.

Results of twin cantilever curl distortion show that the variation  $\Delta Z$  along the cantilever span increased with the increase of Tinuvin concentration. This increase in curl distortion is due to stress associated with the shrinkage induced by Tinuvin (Pilkenton *et al.*, 2011). Horizontal slab distortion was greater the greater the Tinuvin concentration and was also time dependent; it increased dramatically after one day and grew to a maximum after one week. This distortion is due to the internal stress induced by shrinkage when Tinuvin is added.

Tinuvin concentration affected on surface roughness, results show that the average surface roughness  $Ra$  for measured surface increased significantly in both the X-Y plane and Y-Z plane when concentration of Tinuvin increased from zero to 1%. The Results of this part of the investigation will be used in Chapter Five in parametric optimisation.

Finally, in an attempt to reduce dimensional errors induced by shrinkage, a Christmas Tree test piece was used to assess the effectiveness of using a SCF. The results show that dimensional errors could be reduced by a factor of up to three.

## Chapter 5

### Modified Cure Model

#### 5.1 Preliminaries

Mask projection based  $\mu$ SL is a modern rapid prototyping and tooling manufacturing process that builds 3-D parts by projecting a UV light onto a resin surface, where the UV energy induces photopolymerisation in the resin. In mask projection  $\mu$ SL the cross-section of the part being fabricated is projected on the resin surface, and a Digital Micromirror Device (DMD) is used as a mask generator. Hanged features or down-facing surfaces are vital challenges in  $\mu$ SL as it is not easy to predict the cure depth of fabricated parts that contain hanged features. Thus, different researchers such as Zissi et al. (1996) and Choi *et al.*, (2009) have used different light absorbers or polymerisation inhibitors in attempts to control cure depth in  $\mu$ SL and accurately fabricate 3D parts with down-facing surfaces. Based on the results obtained in Chapter Three, PIC-100 acrylate resin with 1% Tinuvin concentration was chosen for the investigation in this chapter due to the best results in cure depth reduction when 1% Tinuvin is used. This investigation will be presented as follows: the chapter starts with a brief review of the theoretical background and Jacobs' exposure model. The second section describes the light intensity measurement and experiments undertaken in order to calibrate Jacobs' exposure model, and the results are analysed in the third section. The last section describes the multi objective function optimisation process to gain the optimum set of parameters to be used.

### 5.1.1 Jacobs' Model

According to the Beer-Lambert law of absorption the relationship between SL cure depth,  $C_d$  ( $\mu\text{m}$ ), and exposure energy at the surface of the resin,  $E_{max}$ , is exponential - see Jacobs' equation (Jacobs 1992):

$$\frac{C_d = D_p \ln E_{max}}{E_c} \quad (5.1)$$

Where  $D_p$  is the penetration depth at the given wavelength and  $E_c$  is the threshold value that is required to start polymerisation process. Based on results obtained from Chapter Two, Tinuvin®327 has significant effects on acrylate resin in terms of reduction in  $E_c$  and  $D_p$ .

### 5.1.2 Limaye's Model

To consider the penetration of the liquid resin and the cured layer, Limaye and Rosen, (2007) modified Jacobs' equation as follows:

$$C_d = D_{pS} \ln \left( 1 + \frac{D_{pL}}{D_{pS}} \cdot \frac{E}{E_c} - \frac{D_{pL}}{D_{pS}} \right) \quad (5.2)$$

Where  $D_{pL}$  is the penetration depth of liquid resin,  $E$  is the exposure time and  $D_{pS}$  is the penetration depth of the cured layer.

Experimentally, the curing process does not progress after a certain limiting cure depth because the exposure falls below the critical energy value ( $E_c$ ). This is due mainly to oxygen inhibition or energy absorption. Although this model directly connects the exposure to the properties of the resin and the final solid part cure depth, it doesn't consider changes due to the addition of any light absorber which reduces cure depth and/or increases part accuracy. Therefore, these models' capability to accurately predict cured part depth in  $\mu$ SL parts needs further investigation, especially when part accuracy is demanded.

Available cure depth models presented in the literature focus only on predicting part height with no consideration of light absorber, and none of them present any method to predict the cure depth of the acrylate resin after adding UV light absorber. Based on a comparison between cure depth experimental results and Jacobs' cure depth model, this chapter proposes a calibration method for Jacobs' model by considering changes in  $E_c$  and  $D_p$  due to the changed properties of PIC-100 after adding Tinuvin®327. An investigation into the influence of exposure energy on surface roughness and mechanical properties for PIC-100 acrylate resin with 1% Tinuvin concentration was carried out using multi-objective function optimisation to obtain the optimal process parameters to minimise cure depth and surface roughness, and to maximise mechanical properties.

## **5.2 Experimental Work**

The experimental work was to determine the effect of addition of Tinuvin®327 on the accuracy of the theoretical exposure model; to investigate whether changes in the exponential relationship between the exposure time and the cure depth occurred after the addition of Tinuvin®327. To achieve this cure depth as a response to exposure time was investigated experimentally and the results and compared with predictions of Jacobs' cure depth model which allowed a calibration of Jacobs' cure depth model. Then, the effect of exposure time

on surface roughness and mechanical properties was studied. After that, multi objective function optimisation was performed in an attempt to find the optimum exposure time to minimise surface roughness while optimising Young's modules of the fabricated part.

### **5.2.1 Light Intensity Measurement**

To accurately test the model the UV intensity of the  $\mu$ SL image, needs to be precisely measured. The method of measurement is described in the following section.

### **5.2.2 Beam Intensity and Profile**

To input the correct values of light intensity into the cure depth model, the light intensity and beam profile were measured using a M12 10-30VDC P86 Photo Sensor from EnvisionTEC®. The sensor lens was 12mm in diameter and was mounted on measuring slider, Fig. 5.1, perpendicular to the beam spot. As specified by EnvisionTEC® (the PIC-100 supplier) irradiance was tuned at 750 mW/dm<sup>2</sup>. To ensure that the centre of the sensor was across the centre of the beam spot, centre to centre alignment was performed by the slider, then the sensor was drawn back to the non-light zone before starting to read the light intensity. Then the slider was moved forward manually across the beam diameter using the slider micrometer. Readings were taken as the slider was moved across the beam centre in increments of 0.5mm. These measurements were repeated six times and the average then plotted as shown in Fig. 5.2. The centre of the beam was taken to be the peak irradiance, this was taken as the maximum light intensity,  $E_{max}$ , used in the cure depth model.

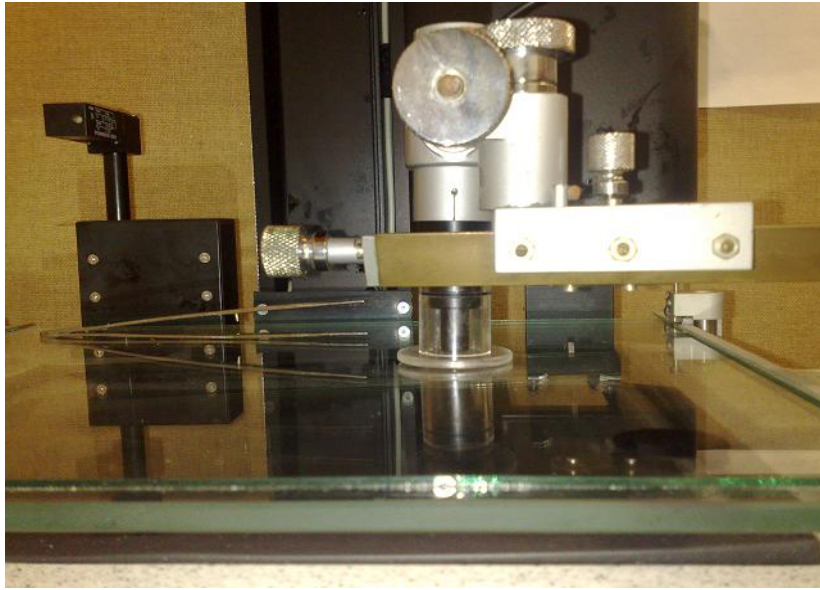


Fig. 5.1 M12 10-30VDC P86 photo sensor mounted on measuring slider

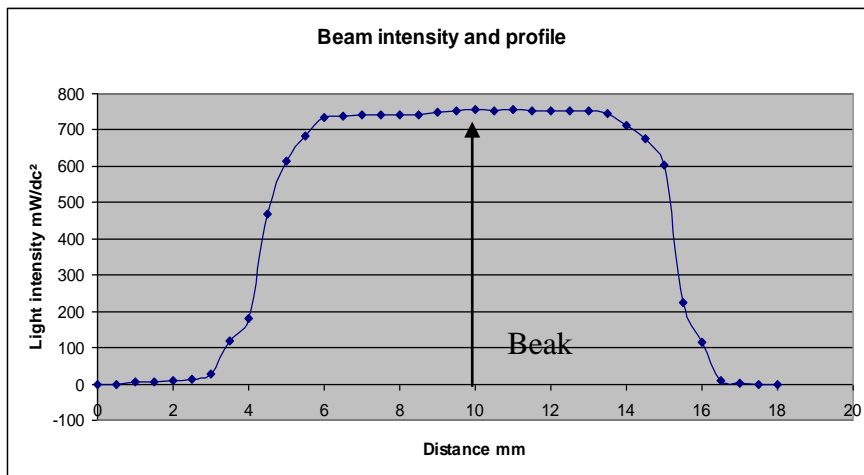


Fig. 5.2 Beam intensity and profile

### 5.3 Exposure Time Model

The exposure energy ( $E_{max}$ , mJ/dm<sup>2</sup>) that the resin surface receives is equal to the irradiance (H, mW/dm<sup>2</sup>) multiplied by exposure time (t, s) (Jacobs 1993). Hence,

$$C_d = D_p \ln\left(\frac{H * t}{E_c}\right) \quad (5.3)$$

This equation can be re-arranged to give the exposure time required for a given cure depth as in Equation 5.4.

$$t = \left(\frac{E_c}{H}\right) \exp\left(\frac{C_d}{D_p}\right) \quad (5.4)$$

where  $E_c$  is in mJ/dm<sup>2</sup>, H is in mW/dm<sup>2</sup>,  $D_p$  and  $C_d$  are in  $\mu\text{m}$  and t is in seconds. The exposure time Equation 5.4 will be used to simulate the cure depth response for increased exposure time. Cure depth experiments are discussed in the following section.

#### 5.3.1 Cure Depth Experiments

To study the response of cure depth to exposure time a PIC-100 acrylate resin with 1% (w/w) Tinuvin®327 concentration was prepared as described in section (3.2.1). A total of 132 circular shape with 12mm diameter were cured with the EnvisionTEC  $\mu\text{SL}$ . The exposure time was varied from 2 seconds to 12 seconds in incremental steps of 500ms. Irradiance was 750 mW/dm<sup>2</sup>, as suggested by the supplier. A transparent glass plate with twenty-four circular cavities of depth 1mm and diameter of 15 mm was cleaned and dried. Results obtained from cure depth experiments in Chapter Three show that the depth of 1 mm is more than the maximum cure depth expected. The resin was dropped into each cavity in turn until it reached the level of the top of the cavity, Fig. 5.3

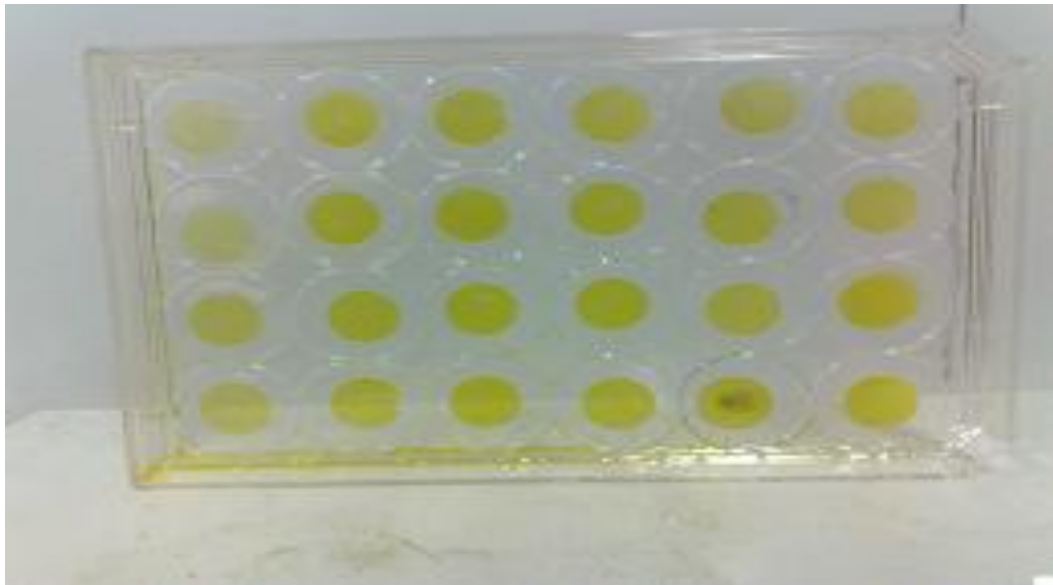


Fig. 5.3 Resin drops on the top of transparent glass



(a) Cured spot before drying



(b) Dry cured spot

Fig. 5.4 Cured spots

After solidification, the samples were put in ultrasonic vat at 20°C for cleaning from residual non solidified resin. Using compressed air with special care the samples were dried. After air drying, the samples were put in an incubator for 30 minutes at 37°C to allow the isopropan to evaporate. The thickness of the cured spots Fig. 5.4 were then measured using a Mitutoyo digital micrometer with an accuracy of  $\pm 0.005\text{mm}$ . Six readings were taken for each exposure time then averaged, and used to plot the graph shown in Fig 5.5.

To compare the experimental results for cure depth with Jacobs' cure depth model, Matlab2010 was utilised to simulate the Jacobs' cure depth model (Equation 5.4), with penetration depth ( $D_p = 34 \mu\text{m}$ ) and critical energy ( $E_c = 1132 \text{ mJ/dm}^2$ ) for the acrylate resin containing 1% Tinuvin concentration. These figures were obtained from the experimental results presented in Chapter Three Section 3.3.2 for PIC-100 resin containing 1% Tinuvin concentration. The irradiance used in the simulation was  $750 \text{ mW/dm}^2$  the same irradiance used in the cure depth experiments. Fig. 5.6 shows both sets of results and it can be seen that there is an increasing discrepancy between the two sets of results with the increase of exposure time. Thus, to better predict the precise cure depth for more accurate part dimensions, Jacobs' cure depth model needs to be calibrated.

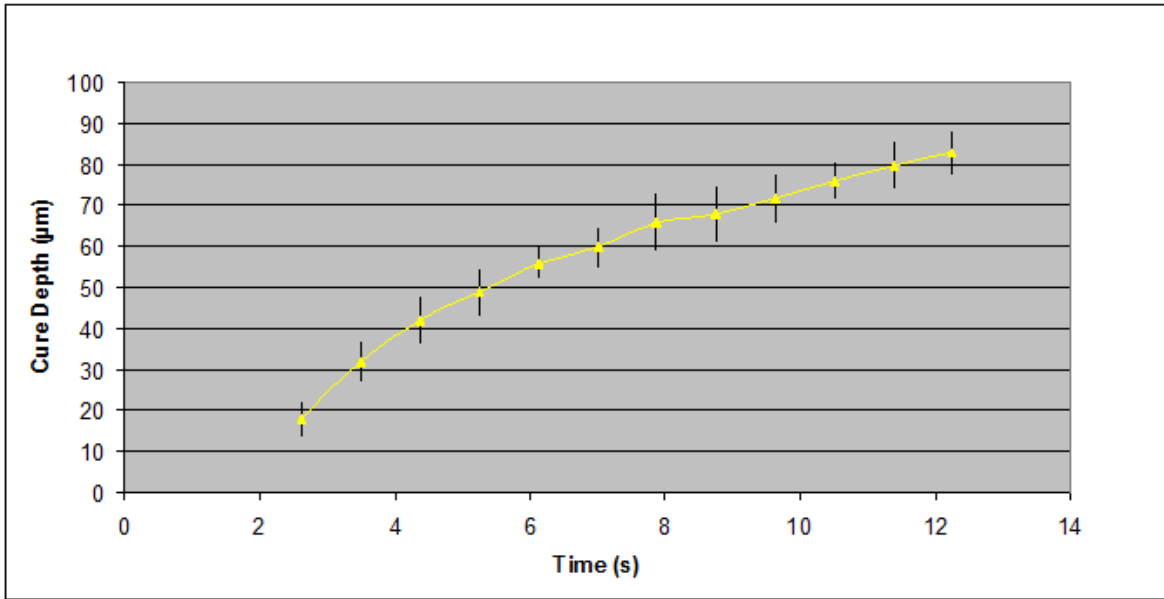


Fig. 5.5 Cure depth as a function of exposure time for irradiance of 750 mW/dm<sup>2</sup>

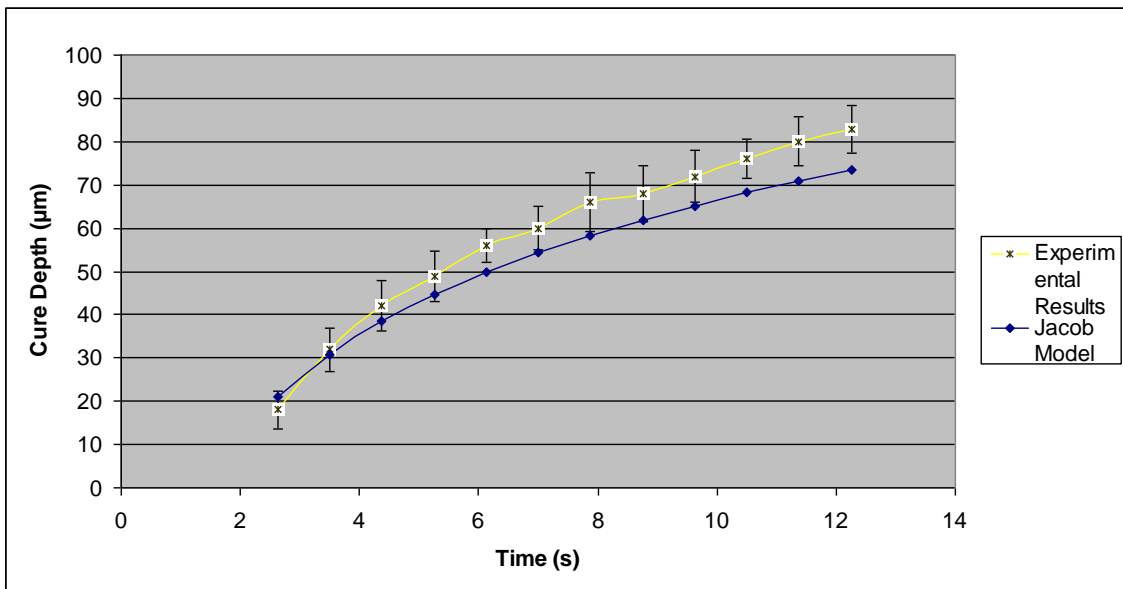


Fig. 5.6 Cure depth as a function of exposure time for irradiance of 750 mW/dm<sup>2</sup> Comparison of results obtained by experiment and simulation.

### 5.3.2 Adaptation of Cure Depth Model

To compensate for the discrepancies between experimental and simulated results shown in Fig. 5.6 and get greater agreement, Jacobs' equation (Equation 5.1) can be modified. To minimise the discrepancies between the experimental results and those obtained from Jacobs' model, Equation 5.1 is modified by adding two dummy constants, A and B, as shown in Equation (5.5).

$$C_d = A * D_p \ln \left( \frac{E_{max}}{E_c} \right) + B \quad (5.5)$$

To find the values of A and B simply requires the solution of two simultaneous equations which contain two different sets of experimental results. including the inputs and their corresponding outputs, were used to calibrate the model as shown in Fig 5.7. In particular, the values that were used are shown in table 5.1. The two equations produced are shown below in equations 5.6 and 5.7.

$$80.0 = 70.865A + B \quad (5.6)$$

$$60.0 = 54.539A + B \quad (5.7)$$

From which A = 1.225 and B = -6.810

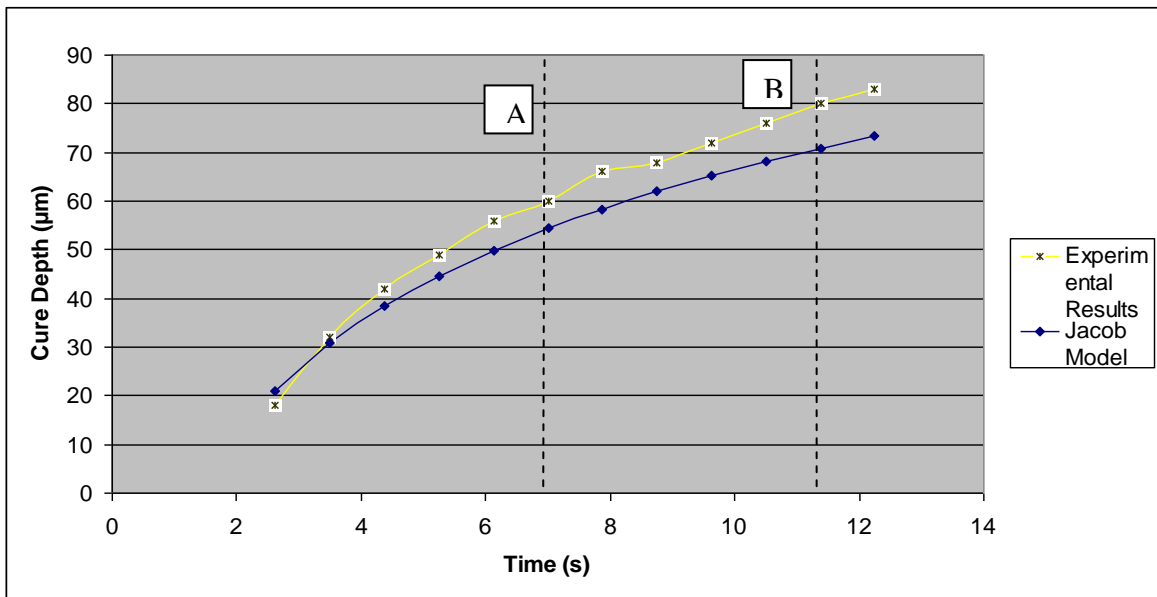


Fig. 5.7 Values selected to calibrate the model.

Table 5.1 Exposure times and corresponded cure depths used to calibrate the model.

Point	A	B
Time (s)	7	11.37
Cure depth Cd ( $\mu\text{m}$ )	60	80

After that, the two equations were solved together as a normal two linear equations. As a result, the values of A and B can be identified and the modified equation that represents the adapted model can be presented as shown in Equation 5.8.

$$C_d = 1.225 * D_p \ln\left(\frac{E_{max}}{E_c}\right) - 6.810$$

(5.8)

This function will be used later in the optimisation section. Fig. 5.8 shows the experimental results and those predicted by the adapted model. There is excellent agreement between both sets of results.

The calibration techniques utilised in this chapter can be used generally to modify any analytical model based on experimental data in order to acquire more accurate predictions. In SL, the underlying chemical reaction takes a place during the experiment and has a dominant effect on the performance of the process but is extremely difficult to take into account in a quantifiable manner. The technique use here offers a reliable method to enhance the available models and provides a simple way to improve them.

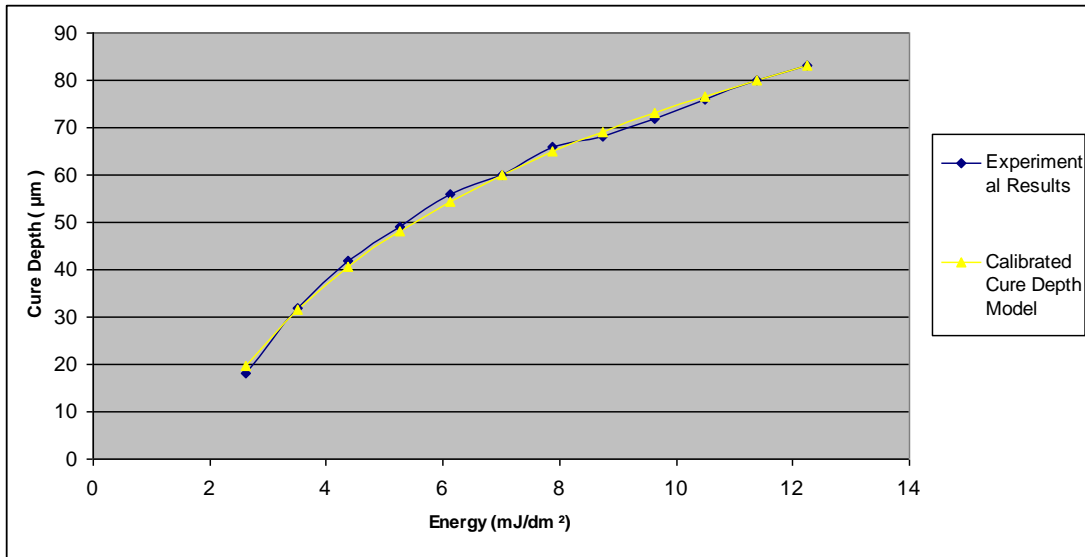


Fig. 5.8 Cure depth as a function of exposure time for irradiance of 750 mW/dm<sup>2</sup>

Excellent agreement between experimental and simulated results using the modified equation.

## **5.4 Mechanical Experiments**

The effect of Tinuvin on the mechanical properties for PIC-100 acrylate resin was studied in Chapter Three, and it was found that adding Tinuvin327 reduced the tensile strength from 16 MPa for the resin without Tinuvin to 5.5 MPa when 1% Tinuvin concentration was added. As explained in Chapter Three the tensile strength was reduced due to the energy absorbed by Tinuvin led to cross-linking density reduction and significant reduction in the mechanical properties of the material.

In this experiment the effect of exposure time on the tensile strength is investigated in attempt to enhance the tensile strength. The tensile tests were carried out using Testometric M500 machine, see Fig. 4.10. The tests were performed at room temperature in Cardiff University MEC laboratory using D638-08 standard V type specimens as shown in Fig. 4.9. The specimens were cured using an EnvisionTEC  $\mu$ SL. The exposure times used to produce sets of six tensile test specimens ranged from 6 seconds to 12 seconds in incremental steps of 500ms, giving a total of 78 specimens for use in the experiments. In the tensile tests, stretching of the specimens was performed at a constant speed rate equal to 10 mm/min according to ASTM D 638-(1991) standard.

## **5.5 Surface Roughness Measurements**

In SLA, the two important phenomena that adversely affect the resulting cure profile shape are over cure, and print-through. Over cure is where the cure depth of the laser is greater than the layer thickness but, of course, some over cure is necessary to ensure bonding to the previously built layer. Print-through is the result of additional exposure that a downfacing feature may receive from layers lying above that feature. This is because succeeding layers add exposure to the downfacing layers, which causes the exposure energy reaching the liquid

resin below the downfacing layer (previously partially exposed) to equal or go above  $E_c$  (Rosen 2004; Limaye 2007).

To measure the influence of exposure time on surface roughness for downfacing features of parts containing 1% Tinuvin concentration, six test parts were fabricated with downfacing feature as shown in Fig. 5.9. A layer thickness of 25 $\mu$ m and irradiance of 800 mW/dm<sup>2</sup> were used for all fabricated parts. By varying the exposure time from 2 sec to 12 sec in incremental steps of 500 ms, the total number test parts used in this experiment was 126. Surface roughness measurements were conducted using a scanning white light interferometer, Micro-XAM from Phase Shift Inc, see Fig. 4.24, Section 4.2.6.6. The average surface roughness of the measured part,  $Ra_{av}$ , was defined as:

$$Ra_{av} = \frac{1}{n} \sum_{i=1}^n Ra_i \quad (5.9)$$

Where n is the total number of readings taken and  $Ra_i$  is the value of the  $i^{\text{th}}$  reading.

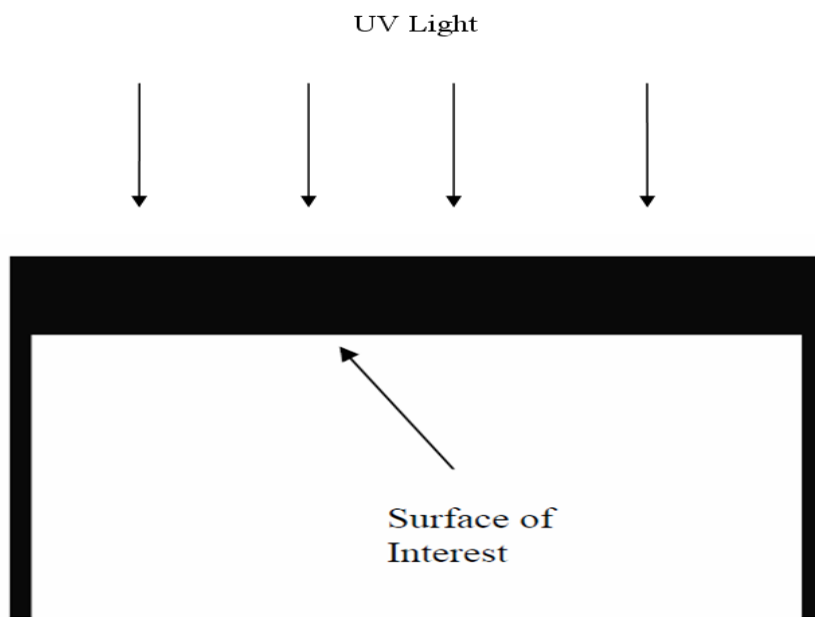


Fig. 5.9 Down-facing feature test part

## **5.6 Results and Discussion**

The mechanical properties and surface roughness of PIC-100 acrylate resin with 1% Tinuvin concentration were investigated. In particular, the effect of exposure energy on surface roughness, mechanical properties and cure depth were examined, and then optimisation process carried out to optimise the best set of parameters to use.

### **5.6.1 Mechanical Properties Results**

This section examines the loss in tensile strength of PIC-100 resin with 1% Tinuvin concentration with incremental increase in exposure time. Fig. 5.10 shows the stress-strain results for 6, 8, 10, 12 seconds exposure. Two main observations can be made; first, the specimens show that the resin with additive behaves in a manner similar to a brittle solid the stress rises linearly with strain followed by sudden fracture. Second, with increased exposure time there is decreased elongation for the same stress – the greater the exposure the greater the strength exhibited by the specimens. The maximum stress that the specimen could withstand before breaking was 10.5 MPa at the maximum 12 seconds exposure time.

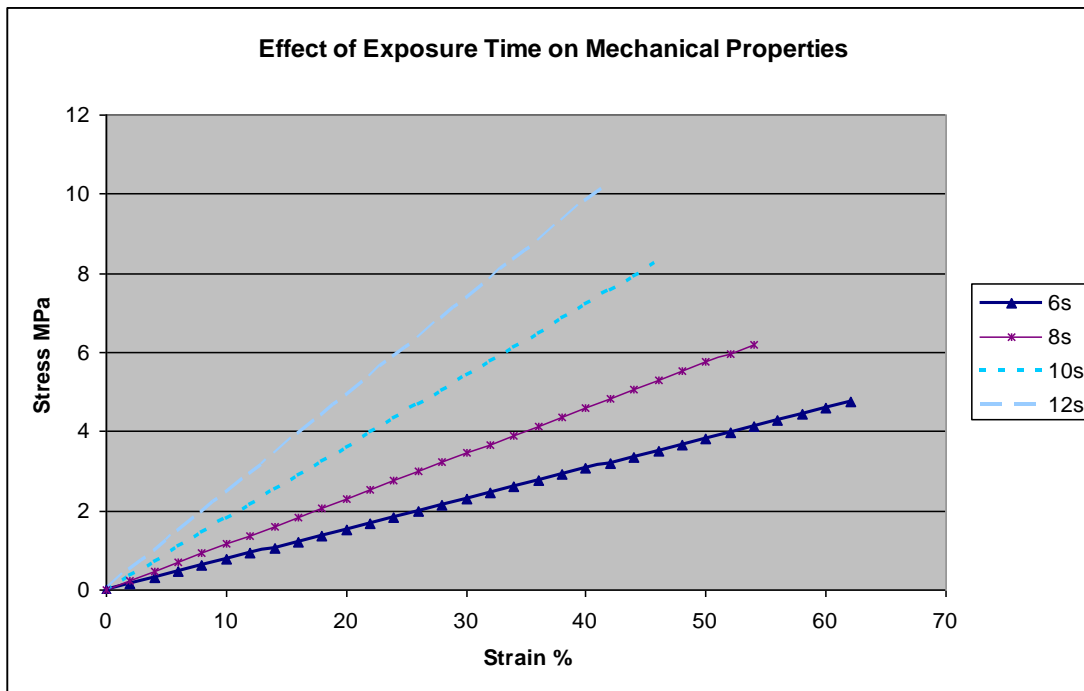


Fig. 5.10 Stress strain curve for PIC-100 + 1% Tinuvin concentration with different exposure times.

The elastic modulus was determined by measuring the slope of the linear stress-strain curves, which gave a range of values for the elastic modulus from 7.7 to 24.5 MPa depending on Tinuvin concentration. Fig. 5.11 shows the relation between the exposure time and Young's modulus; clearly the higher the exposure time the higher the Young's modulus. The reason for this behaviour is the reduced degree of polymerisation and cross-linking density of the PIC-100 with lower irradiation exposure, increasing exposure increases the cross-linking density. It is well known that lowering exposure leads to lowering the mechanical properties such as tensile strength and Young's modulus and turns the properties of the material from elastic towards viscoelastic (Pilkenton *et al.*, 2011). These changes in the material structure change the material's resilience. This behaviour has to be taken into account when light absorber is introduced to the material to control the layer thickness. Using the Young's modulus experimental results the best fit equation for modelling the Young's modulus ( $Y$ , MPa) in terms of exposure time ( $t$  seconds) is:

$$Y = 2.422 \exp(0.1972t)$$

(5.10)

This equation will be used later in the optimisation section.

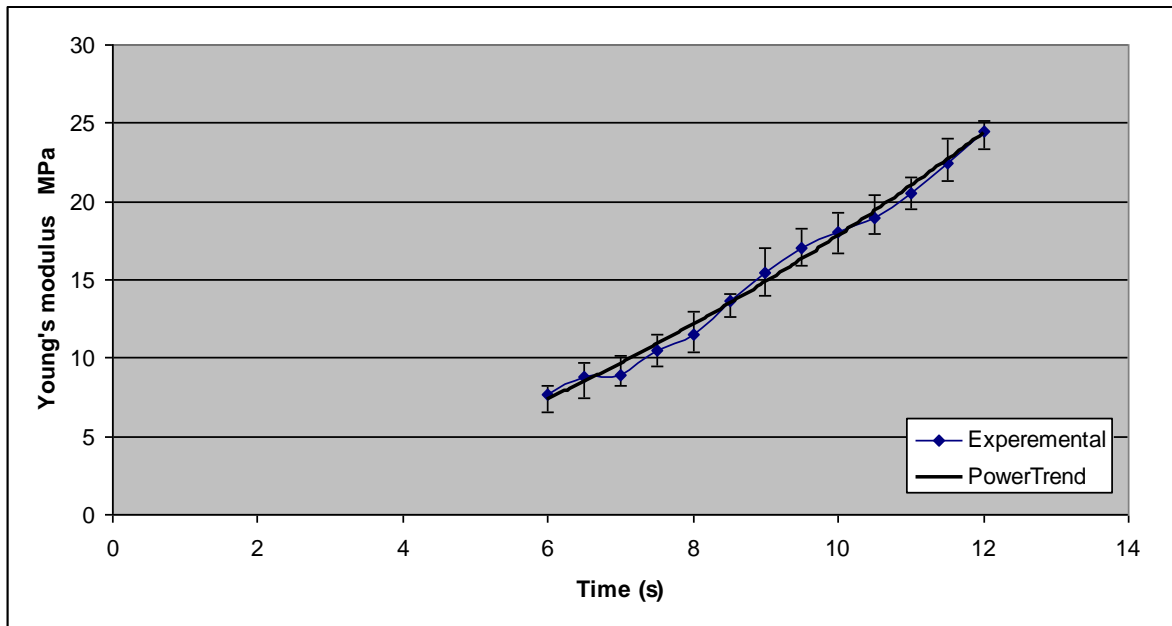


Fig. 5.11 Young's modulus values vs exposure time for PIC-100 with 1% Tinuvin concentration

### 5.6.2 Surface Roughness Results

Average Surface roughness results plotted versus exposure time are shown in Fig. 5.12. The maximum and minimum values of  $Ra$  are  $0.42 \mu\text{m}$  and  $0.15\mu\text{m}$  respectively. The results of the tests undertaken in this study show an increase in surface roughness with exposure time up to about 8 sec, for exposure times greater than 8 seconds the relation is reversed and surface roughness decreases with increase of exposure time (exposure energy). Using the experimental surface roughness results the equation for modelling the average surface roughness ( $Ra$ ,  $\mu\text{m}$ ) in terms of exposure time ( $t$ , seconds) can be accurately presented as the cubic expression:

$$Ra = 0.0113t^3 - 0.3229t^2 + 2.9495t - 8.3362 \quad (5.11)$$

This function will be used later in the optimisation section.

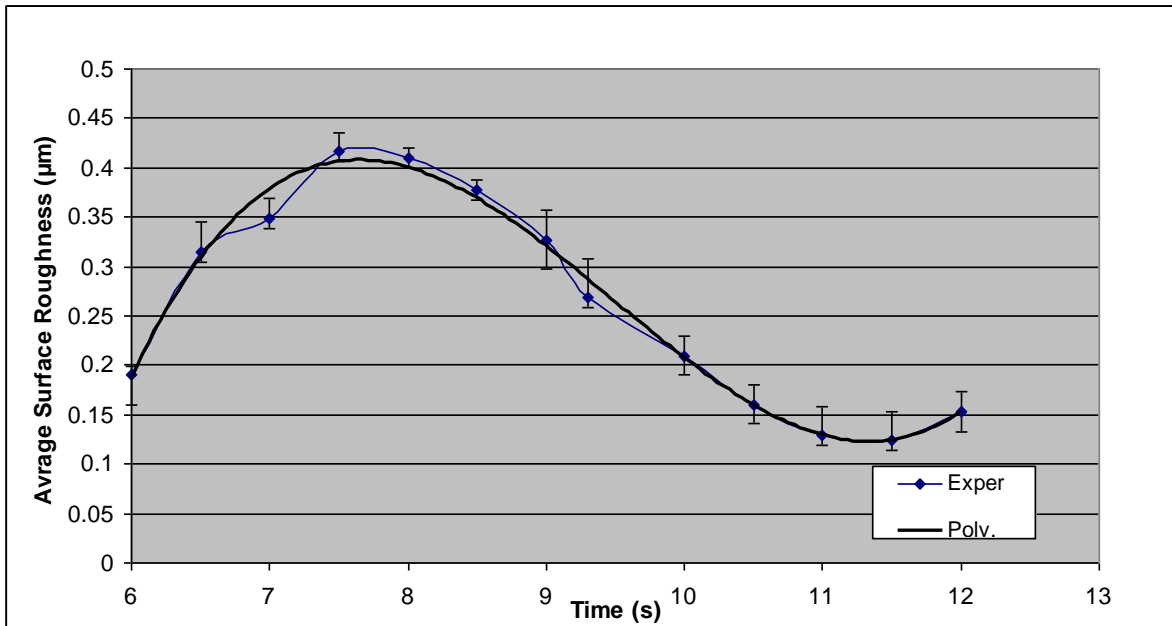


Fig. 5.12 Average Surface roughness vs exposure time for PIC-100 with 1% Tinuvin concentration

## 5.7 Optimisation

Optimisation is a mathematical technique to find the fittest value based on the performance measurement function called, Objective Function (Rao, 1996). There are several types of classification approach for optimisation problems. One of these classification techniques is based on the number of objective function. If an optimisation problem has one objective function, it's called Single objective optimisation problem, if the objective numbers are more than one, then its called Multi-objective problem. There are several techniques proposed to solve Multi-objective optimisation, one of them is Pareto based Multi-objective function. In this study Pareto based Multi-objective function was employed to solve the optimisation problem using Matlab 2010 tool box. The problem has three objective functions. The goal is to find the optimum exposure time value by minimising the cure depth ( $Cd$ ), surface roughness ( $Ra$ ) and maximising the mechanical strength ( $y$ )

Equal weight was given to all three criteria. The given Multi-objective optimisation problem is shown in equation (5.14).

$$\lambda = w_1 Cd + w_2 Ra + w_3 y \quad (5.14)$$

Where  $w_1$ ,  $w_2$ ,  $w_3$  are the weight mass function, and  $Cd$ ,  $Ra$  and  $y$  were as given below.

$$C_d = 1.225 * D_p \ln \left( \frac{E_{max}}{E_c} \right) - 6.810 \quad (5.8)$$

$$Y = 2.422 \exp(0.1972t) \quad (5.10)$$

$$Ra = 0.0113t^3 - 0.3229t^2 + 2.9495t - 8.3362 \quad (5.11)$$

The minimum of cure depth  $C_d$ , surface roughness  $R_a$ , and the maximum mechanical strength were graphically determined from Fig. 5.13, and shown in table 5.2.

Fig. 5.14 shows the graphs of Fig. 5.13 normalised to their maximum values, to unify the ranges of all three objectives of the optimisation process.

The boundary conditions chosen for cure depth, surface roughness and mechanical strength are, respectively:

$$14.8 \leq C_d \leq 85 \mu\text{m} \quad (5.15)$$

$$0.12 \leq R_a \leq 0.41 \mu\text{m} \quad (5.16)$$

$$7.65 \leq (Y) \leq 24.5 \text{ MPa} \quad (5.17)$$

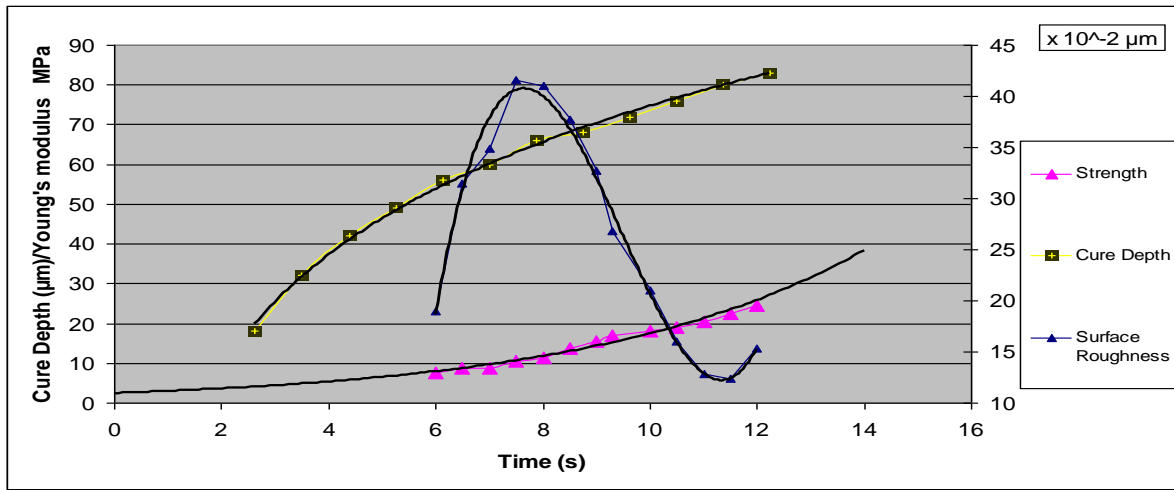


Fig. 5.13 Cure depth, Young's modulus and average surface roughness vs exposure time for PIC-100 with 1% Tinuvin concentration

Table 5.2 Optimisation Boundary Conditions

Minimum cure depth $C_d$ µm	Minimum average surface roughness $R_a$ µm	Maximum mechanical strength $Y$
14.8	<b>0.12</b>	24.5

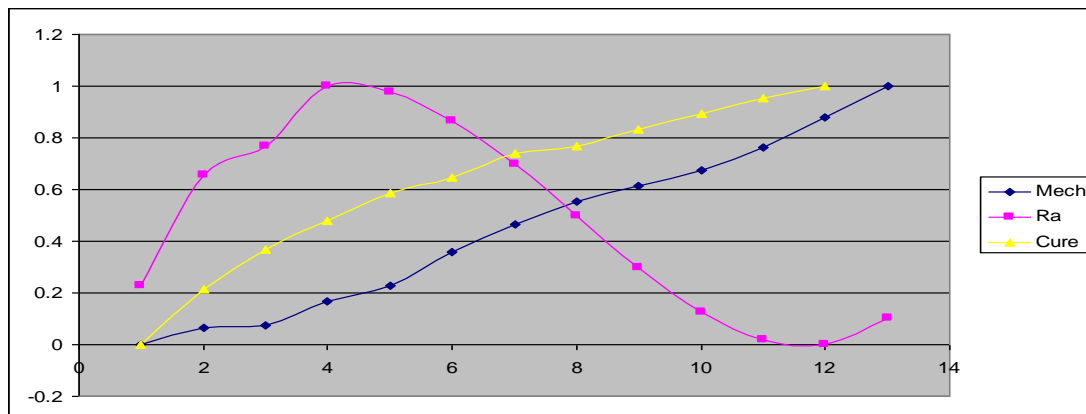


Fig. 5.14 Normalised graph to unify the ranges of all the three objectives for the optimisation process.

Table 5.3 Results for 10 second exposure time

Cure depth $Cd$ ( $\mu\text{m}$ )	Average Surface roughness $Ra$ ( $\mu\text{m}$ )	Mechanical strength $Y$ (MPa)
72	<b>0.21</b>	17

The results of Multiobjective Functions optimisation are shown in Table 5.3. With the weightings given this analysis suggests that an exposure time of 10 seconds will give the optimum match of cure depth, average surface roughness and mechanical strength: with  $C_d = 72 \mu\text{m}$ ,  $R_a = 0.21\mu\text{m}$  and  $Y = 17 \text{ MPa}$ .

The cure depth of  $72 \mu\text{m}$  is high but still acceptable as the cure depth should be greater than the layer thickness to ensure sufficient bonding force between layers (Takada K et al 2005). The average surface roughness  $R_a$  for 10 second exposure was  $0.21\mu\text{m}$ . A reasonable explanation for this phenomenon involves “optical scattering” where micro defects such as cavities and blockages work as scattering centres. These scattering centres, act to trim down the peak exposure at  $y = 0$ , and  $z = C_d$ , compared with that calculated from Jacobs’ model. This will then reduce the real cure depth and voxel size, consequently, the effect will appear on the surface as a small voxel size (Pal. et al., 2008). The mechanical strength of PIC-100 resin with 1% Tinuvin concentration increases from about  $7.5 \text{ MPa}$  at six seconds exposure to  $17 \text{ MPa}$  at 10 seconds exposure due to more chain cross-linking in the polymerisation process.

## 5.8 Summary

This chapter presented an approach to the experimental calibration (modification) of Jacobs' cure depth model to better predict the cured thickness for down facing and hanging features. Using acrylate PIC-100 resin with 1% concentration of Tinuvin®327 it was found that the results predicted by Jacobs' cure model exhibited a different trend from the experimental observations of part height. It is suggested that the reason why the results predicted by Jacobs' model do not keep pace with the changes that actually occur to PIC-100 with added Tinuvin during the photopolymerisation process is because of the changes in material characteristics due to the addition of Tinuvin®327.

The addition of Tinuvin®327 has a significant positive effect as reported in Chapters Three and Four but it also has some disadvantages, particularly lowering the mechanical properties and increasing surface roughness of the fabricated parts. These negative features can be offset to an extent by increasing the exposure time. Founded on experimental results of the effect of exposure time on cure depth, surface roughness and mechanical properties, a parametric optimisation process (Multi objective function from Matlab2010) was applied to simultaneously minimise cure depth and surface roughness, and to maximise the mechanical properties.

## Chapter 6

### Conclusions

This chapter summarises the main contributions of this research and the conclusions reached. It also provides suggestions for future work.

#### 6.1 Contributions

This research investigated the influence of different concentrations of Tinuvin®327 as a light absorber on cure depth, and final part accuracy and mechanical properties (in particular tensile strength, Young's modulus and surface roughness). The effect of different Tinuvin concentrations on final part shrinkage was also examined. These investigations were used to optimise exposure time for the best possible combination of mechanical properties, cure depth and surface roughness.

The contributions of this work include:

##### **Effects of Tinuvin®327 on properties of PIC-100 acrylate resin.**

###### ***a. Relationship between Tinuvin concentration and minimum cure depth.***

A thorough investigation of the effects of Tinuvin concentration on the cure depth has been carried out, especially on overhanging features and the resulting thickness. The experimental study investigated the cure depth response to five different Tinuvin concentrations in the acrylate resin. One resin was “as received” PIC-100, and the other four samples were mixed with 0.1, 0.25, 0.5 and 1.0 % w/w Tinuvin®327.

###### ***b. Relationship between Tinuvin concentration and critical energy.***

An investigation of the effects of Tinuvin concentration on the critical exposure energy has been conducted. In particular, critical energy results obtained from the PIC-100 resin working curve were compared with results obtained from experimental work on Gel spots.

***c. Correlation between Tinuvin concentration and penetration depth.***

The relation between Tinuvin®327 concentration and penetration depth for PIC-100 resin was determined.

***d. Relationship between the Tinuvin concentration and tensile strength.***

A methodical investigation has been carried out on the effects of Tinuvin concentration in PIC-100 resin on the mechanical properties of fabricated parts, in particular, tensile strength, elongation and Young's modulus.

***e. Correlation between Tinuvin concentration and final part density.***

An experimental investigation into the effect of Tinuvin concentration on final part density has been carried out, and the relationship between the final part density and Tinuvin concentration determined.

***f. Effects of Tinuvin concentration on final part accuracy.***

An experimental investigation on the effects of Tinuvin concentration on final part shrinkage has been conducted. In particular, dimensional accuracy in the X-Y plane in terms of linear dimensions, form, and position has been investigated and suitable shrinkage factors determined for each Tinuvin concentration.

***Adaptation/Calibration of Jacobs' model to better reflect experimental results.***

g. An experimental approach has been presented of a possible method of adapting Jacobs' cure depth model to the experimental results obtained for PIC-100 resin after the addition of Tinuvin.

**Optimisation of exposure time to minimise cure depth and surface roughness and maximise tensile strength of the final part.**

h. The results obtained for responses of the PIC-100 resin with 1% Tinuvin added have been used to optimise the exposure time to produce simultaneously minimum cure depth and average surface roughness while maximising mechanical strength.

## **6.2 Conclusions**

Based on this research work, the following conclusions can be drawn for the  $\mu$ SL process:

**Effects of Tinuvin®327 on PIC-100 acrylate resin properties.**

The investigation has shown the importance of even very small changes in light absorber additive (such as Tinuvin®327) concentrations for the structure and properties of the material: reduction in cure depth and penetration depth and significant increase in critical energy.

In particular, the following conclusions can be drawn from this investigation:

- The measured average cure depth at 800 mW/dm<sup>2</sup> irradiance was 60 μm at 1% Tinuvin®327 concentration, and 116 μm at 0.1% Tinuvin®327 concentration. Tinuvin®327 concentration has a significant effect on cure depth for PIC-100 acrylate resin, the higher the Tinuvin®327 concentrations the lower the cure depth, see Fig. 3.7.
- Addition of Tinuvin®327 affected the resin's critical energy. The critical energy for the PIC-100 acrylate resin increased from 820mJ/dm<sup>2</sup> for zero Tinuvin to 1132mJ/dm<sup>2</sup> for 1% Tinuvin concentration, see Table 3.3. This means that, after the addition of Tinuvin, extra exposure time is needed to achieve the same cure depth as before the addition.
- The high absorption of energy by Tinuvin®327 also affected the penetration depth of the resin. The penetration depth for the PIC-100 acrylate resin decreases from 65μm at 0.1% Tinuvin concentration to 34μm at 1% Tinuvin concentration, see Table 3.2. These results were calculated from the cure depth working curve and were confirmed by the experimental work in critical energy.

**Effects of Tinuvin®327 concentration on PIC-100 mechanical and physical properties**

- The experimental results show that the resin behaved similarly to a brittle solid and that stress increased linearly with strain followed by sudden fracture. For resin with no Tinuvin added, fracture occurred when the stress reached 16 MPa, but for resin with 1% Tinuvin concentration fracture occurred at 5 MPa, see Fig. 3.12. Correspondingly the elastic modulus decreased from 20 to 8 MPa as the Tinuvin concentration increased, see Table 3.4.

- The density of the resin decreased sharply with the proportion of Tinuvin®327 added, see Fig. 3.13. The change in the density of the material is in proportion to the change in the mechanical properties and demonstrates the hypothesis that the structural changes are induced by the addition of Tinuvin®327; the decrease in density of about 20% led to a decrease in strength and increase in elasticity with more than 20% which shifts the properties of the photo-polymer towards being more ‘elastomer-like’.
- The results show that tensile strength could be improved for the resin with 1% by the increase of exposure time, see Table 3.5. The reason proposed for this behaviour is the increased degree of polymerisation and cross-linking density of the thermoset resin when extra energy is introduced into the compound. It is well known that increasing the crosslinking density leads to increase the mechanical properties.

**Effects of Tinuvin®327 concentration on PIC-100 final part accuracy.**

- Increasing Tinuvin®327 concentration increased shrinkage of the acrylate resin with significant consequent effect on linear dimension error, cantilever curl distortion and horizontal slab distortion see, for example, Figs. 4.22 and 4.23. Tinuvin®327 has no significant effect on roundness and position error when the concentration is less than 0.25% while the error becomes obvious at Tinuvin concentrations of 0.5% and above see, for example, Fig. 4.12.
- Results from surface roughness investigation show that when Tinuvin concentration was increased from zero to 1% the average surface roughness measured in X-Y plane increased from 0.53µm to 0.75µm, while in Y-Z plane (layer thickness direction) the

average surface roughness dramatically increased from 2.25 $\mu\text{m}$  to 3.35 $\mu\text{m}$ , see Tables 4.3 and 4.4 respectively. The difference in the X-Y plane may be small, but the difference in the Y- Z plane is substantial.

- As a result from the addition of Tinuvin and subsequently changes in the resin properties, Jacobs' model no longer accurately describes the behaviour of the resin cure depth. Jacobs' model was adapted by the addition of two dummy constants (Section 5.3.2) and model then showed an excellent agreement with experimental results, see Fig. 5.8. This calibration technique can be used generally to modify any analytical model based on experimental data to give more accurate results. The new model equation was successfully used in the optimisation process.
- Multi-objective function optimisation was used to determine the exposure level (for PIC-100 with 1% Tinuvin concentration) that would give minimum cure depth and surface roughness but maximise mechanical strength. The predicted optimum exposure time was 10 seconds. At this exposure mechanical strength of PIC-100 resin with 1% Tinuvin concentration was 17 MPa, the cure depth was 72  $\mu\text{m}$  and the average surface roughness Ra was 0.21 $\mu\text{m}$ , see Section 5.7.

It can be concluded that the results of this research confirm the initial hypothesis that, in micro stereolithography ( $\mu\text{SL}$ ), the light absorbers added to the resin play a significant role in the properties of the produced part. This effect is even more important when micro parts are being fabricated. The results of this research clearly demonstrate that Tinuvin®327 concentration needs careful consideration especially when part strength and final part accuracy are important.

### 6.3 Future Work

Based on the work presented here, some areas of future research efforts have been identified as follows:

- Expanding Jacobs' model for the cure depth, via deterministic approach modelling. This would enable cure depth to be more accurately estimated.
- The influence of post-cure treatment on the resulting mechanical properties should be studied and compares with those before post-curing.
- PIC-100 resin is slightly transparent so it would be of interest to study the influence of adding different concentrations of Tinuvin®327 (an organic pigment) to micro stereolithography resins such as R11 and other dark resins.
- Expanding the optimisation work by changing the Tinuvin concentration and get one line for each Tinuvin concentration, over the range 0% to 1% in very small steps. This will lead to optimising the exposure time for every Tinuvin concentration.

## References

ASTM D 638-1991. *Standard Method for Tensile Properties of Plastic* (1991).

Atkins, P. and de Paula, J. (2005) *“Elements of Physical Chemistry”* (4th Ed) W. H. Freeman, USA.

Azari, A., and Nikzad, S. (2009) *“The evolution of rapid prototyping in dentistry: a review”* Rapid Prototyping Journal Vol.15, No.3, pp 216–225.

Bartolo, P.J, (2006) *“Computer simulation of stereolithographic curing reactions: phenomenological versus mechanistic approaches”* Annals of the CIRP Vol. 55/1/2006.

Bartolo. P. J, (2011) *“Stereolithography: Materials, Processes and Applications”* Springer London. ISBN 978-0-387-92903-3.

Bertsch, A., Zissi, S., Jezequel, J.Y., Corbel, S. and Andre, J.C., *“Microstereolithography: concepts and applications,”* Proceedings of 8th IEEE International conference on Emerging Technologies and Factory Automation, 2001, pp. 289~298.

Bertsch, A., Jiguet, S., Bernhard, P., and Renaud, P. (2003) *“Micro stereolithography: a review”*. Symposium on Rapid Prototyping Technologies, *Materials Research Society Symposium Proceedings*, December 3-5, 2002. Boston.

Bertsch, A., Jiguet, S., and Renaud, P. (2004) *“Microfabrication of ceramic components by micro stereolithography”*, Journal of Micromechanics and Microengineering, Vol. 14, pp. 197-203.

Boddapati, A. (2010) *“Modeling cure depth during photopolymerization of multifunctional acrylates”*, MS thesis, School of Chemical and Biomolecular Engineering, Georgia Institute of Technology, Atlanta, GA.

Boddapati, A., Rahane, S., Slopek, R., Breedveld, V., Henderson, C., and Grover, M., (2011) "*Gel time prediction of multifunctional acrylates using a kinetic model*", Polymer 52 pp866-873.

Bolgar, M., Hubball, J., Groeger, J., and Meronek, S. (2008) "*For the Chemical Analysis of Plastic and Polymer Additives*", Taylor & Francis Group, LLC, No:13: 978-1-4200-4487-4.

Broer, D., Mol, G., and Challa, G. (1991) "*Temperature effects on the kinetics of photoinitiated polymerization of dimethacrylates*". Polymer, 32(4), 690-695.

Bugeda, G., and Cervera, M. (1995) "*Numerical analysis of stereolithography processes using the finite element method*", Rapid Prototyping Journal, Vol. 1 Iss: 2, pp.13 – 23

Chartoff, R., Priore, B., Klosterman, D., and Pak, S. (1996) "*Composite tooling via laminated object manufacturing, a rapid and affordable method*", The 28th International SAMPE Technical Conference, Seattle, WA, November 4-7.

Childs, T.H.C., and Juster, N.P. (1994) "*Linear and geometric accuracies from layer manufacturing*", Annals of the CIRP, Vol. 43 No. 1, pp. 163-6.

Chockalingam, K., Chandrasekhar, U., and Jawahar. N, (2006) "*Influence of layer thickness on mechanical properties in stereolithography*", Rapid Prototyping Journal Volume 12 · Number 2 · pp106–113.

Chua, C., Leong, K., Lim, C. (2003) *Rapid Prototyping: Principles and Applications*, World Scientific Publishing, Singapore.

Chui, S-H., Pong, S-H., Wu, D-C., and Lin, C-H. (2008) "*A study of photomask correction method in area-forming rapid prototyping system*" Rapid Prototyping Journal Volume 14 · Number 5 pp. 285–292.

Ciba, Special Chem. (2008) “*Plastic & Elastomers formulation*” [Online]. Available from <http://www.specialchemipolymers.com/index.aspx>. [Accessed: 1/Des/2011].

Ciba, Special Chem. (2012) “*Light Stabilizers For Polyolefins*” [Online] Available from [http://www.mufong.com.tw/Ciba/ciba\\_guid/additives\\_polyurethane.pdf](http://www.mufong.com.tw/Ciba/ciba_guid/additives_polyurethane.pdf). [Accessed: 15/March/2012].

EnvisionTEC®. (2008) “*Computer-aided Modelling Devices*” [Online] Available from [www.envisiontec.com/index.php](http://www.envisiontec.com/index.php). [Accessed: 12/jun/2010].

Eyers, D., and Dotchev, K. (2010) “*Technology review for mass customisation using rapid manufacturing*” *Assembly Automation*. V- 30 · N- 1 · 2010 · pp 39–46.

Fadel, G., and Kirschman, C. (1996) “*Accuracy issues in CAD to RP translations*” *Prototyping Journal* Volume 2 . Number 2 . 1996 . pp. 4-17.

Fuh, J., Lu, L., Tan, C., Shen, Z., and Chew, S. (1999) “*Curing characteristics of acrylic photopolymer used in stereolithography process*”, *Rapid Prototyping Journal* Volume 5 · Number 1 · pp. 27–34.

Gupta, R. (2010) “*Theory and Laboratory Experiments in Ferrous Metallurgy*”, PHI Learning Private Limited, New Delhi.

Gebhardt, A. (2000) “*Industrielle rapid prototyping systeme*. *Rapid Prototyping*, 2nd ed., Hanser, Berlin, pp. 81-235.

Gebhardt, A. (2003) “*Rapid Prototyping*”. *Carl Hanser Verlag*, Munich ISBN 156990-281.

Gregorian, A., Elliott, B., Navarro, R., Ochoa, F., Singh, H., Monge, E., Foyos, J., Noorani, R., Fritz, B., and Jayanthi, S. (2001) “*Accuracy Improvement In Rapid Prototyping Machine (FDM-1650)*”, *Solid Freeform Fabrication Proceedings*, 2001, pp 77-84.

Grimm, T. (2004) “*User's guide to rapid prototyping*” *Society of Manufacturing Engineering*, USA.

Hackney, P., Arulraj, A., Chinnaswamy, G., and Nair, B. (2005) “*Investigation into the Perfactory Process for Production of Accurate and Strong Functional Parts*” 6th National Conference on Rapid Prototyping, Buckinghamshire Chilterns University College, UK.

Hackney, P., Chinnaswamy, G., Arulraj, A. and Nair, B. (2005) “*Investigation into urface Finish of Parts Built by the EnvisionTec PerFactory® Rapid Prototyping Process*”. 6th National Conference on Rapid Prototyping, Rapid Tooling and Rapid Manufacturing, Buckinghamshire Chilterns University College, UK.

Han, L., Mapili, S., Chen, K., and Roy, J. (2008) “*Projection Microfabrication of Three-Dimensional Scaffolds for Tissue Engineering*” Journal of Manufacturing Science and Engineering, Vol. 130 No.2, 021005-3.

Heller, C., Schwentenwein, M., Russmueller, G., Varga, F., Stampfl, J., and Liska, R. (2009) “*Vinyl Esters: Low Cytotoxicity Monomers for the Fabrication of Biocompatible 3D Scaffolds by Lithography Based Additive Manufacturing*” Journal of Polymer Science: Part A: Polymer Chemistry, Vol. 47, 6941–6954.

International Standard ISO 1101(1983) “*Technical Drawings - Geometrical Tolerancing*”, ISO 1101 (1983) 12-01.2.

Jacobs, P. (1993) *Rapid Prototyping and Manufacturing: Fundamentals of Stereolithography*, McGraw-Hill, New York.

Jacobs, P. (1996) “*Stereolithography and other RP&M Technologies - from Rapid Prototyping to Rapid Tooling*”. Dearborn, Society of Manufacturing Engineers.

Choi, J-W., Wicker, R., Cho, S-H., Ha, C-S., and Lee, S-H. (2009) “*Cure depth control for complex 3D microstructure fabrication in dynamic mask projection micro stereolithography*”, Rapid Prototyping Journal, Vol. 15 No.1, pp.59-70.

Jariwala, A., and Ding, F. (2011) "*Modeling effects of oxygen inhibition in mask-based stereolithography*" Rapid Prototyping Journal V.17 · N. 3 · pp · 168–175

Jensen, C., Helsel, J., and Espin, E. (2011) "*Interpreting Engineering Drawings*" 6th Canadian edition.

Lee, J.H., Prud'homme, R.K., and Aksay, I.A. (2001) "*Cure depth in photopolymerization: Experimental and theory*", J Mater Res 16 (2001), pp. 3536–3544.

Kim, G., and Lee, J. (2005) "*Prediction of Curl Distortion using Classical Lamination Theory in Stereolithography*", Korean Soc of Precision Eng J, Vol. 22, No.11.

Kirkup, L., and Frenkel, B., (2006) "*An Introduction to Uncertainty in Measurement*," Cambridge: Cambridge University Press.

Kruth, J-P. (1991) "*Material increase manufacturing by rapid prototyping techniques*", Annals of the CIRP, Vol. 40 No. 2, pp. 603-14.

Limaye, A. (2004) "*Design and Analysis of A Mask Projection Micro stereolithography*" MS Thesis, Georgia Institute of Technology, GA.

Limaye, A., and Rosen, D. (2007) "*Process planning method for mask projection micro stereolithography*" Rapid Prototyping Journal, Vol. 13 No.2, pp.76-84.

Lovell, L., and Bowman, C. (2003) "*The effect of kinetic chain length on the mechanical relaxation of cross linked photopolymers*". Polymer 44 , 39-47.

Manias, E., Chen, J., Fang, N., and Zhang, X. (2001) "*Polymeric micromechanical components with tunable stiffness*" Appl. Phys. Lett., Vol. 79, No. 11, 10 September 2001.

Minev, E., Popov, K., Minev, R., Dimov, S., and Packianather, M. (2010) "*Utilising a grid method for accuracy study of micro SLA parts*", Proc. Of 4M Conference, Plastipolis, Oyonnax, France, Nov 2010, pp.257-260.

Mitutoyo 2010 <http://www.mitutoyo.co.uk/Mit/downloads/vision/QVElf.pdf>

[Accessed:1/Dec/2010]

Montgomery, D., and Runger, G. (2011). *Applied Statistics and Probability for Engineers*, John Wiley & Sons, New York.

Pan, Y., Chen, Y., and Zhou, C. (2012) "*Fabrication of Smooth Surfaces based on Mask Projection Stereolithography*" Proceeding of 40<sup>th</sup> SME-North American Manufacturing Research Conference, NAMRC40-7715, Notre Dame, Indiana, June 4-8, 2012.

Pal, A., Bruce, R., Weilmboeck, F., Engelmann, S., Lin, T., Kuo, M-S., and Phaneuf, R. (2008) "*Real-time studies of surface roughness development and reticulation mechanism of advanced photoresist materials during plasma processing*" J. Appl. Phys. 105, 013311  
\_2009\_

Park, J., Tari, M., and Hahn, H. (2000) "*Characterization of the laminated object manufacturing (LOM) process*" Rapid Prototyping Journal Volume 6 . Number 1. 2000. pp. 36-49.

Pham, D.T., and Dimov, S.S. "*Rapid prototyping and rapid tooling-the key enablers for rapid manufacturing*" Proc Instn Mech Eng Part C, 217 (2003), pp. 1–23.

Pilkenton, M., Lewman, J., and Chartoff, R. (2011) “*Effect of oxygen on the crosslinking and mechanical properties of a thermoset formed by free-radical photocuring* “ *Journal of Applied Polymer Science*, Volume 119, Issue 4, pages 2359–2370, 15 February 2011,.

Puncochar D E. (1997) “*Interpretation of Geometric Dimensioning and Tolerancing*”, Industrial Press Inc, New York .

Rosen, D.W. (2004) *Rapid Prototyping in Engineering*. Atlanta, GA, Georgia Institute of Technology ME 7227.

Salmoria, G., Ahrens, C., Fredel, M., Soldi, V., and Pires. A. (2005) “*Stereolithography somos 7110 resin: mechanical behavior and fractography of parts post-cured by different methods*” *Polymer Testing* 24 (2005) 157–162.

Scherzer, T., and Decker, U. (1999). “*Kinetic investigations on the UV-induced photopolymerization of a diacrylate by time-resolved FTIR spectroscopy: the influence of photoinitiator concentration, light intensity and temperature*” *Radiation Physics and Chemistry*, 55, 615-619.

Stopp, S. (2008) “*A new method for printer calibration and contour accuracy manufacturing with 3D-print technology*” *Rapid Prototyping Journal*. V: 14 · N: 3 · PP · 167–172.

Stratasys (2012) [Online]. Available from <http://www.stratasys.com/>

Accessed: 3/Feb/2012]

Sun, C., Fang, N., Wu, D., and Zhang, X. (2005) "*Projection micro-stereolithography using digital micromirror dynamic mask*", *Sensors and Actuators A: Physical*, Vol. 121 No. 1, pp. 113-20.

Takada, K., Sun, H.B., and Kawata, S. (2005) "*Improved spatial resolution and surface roughness in photopolymerization-based laser nanowriting*" *Appl. Phys. Lett.*, vol. 86, no. 7, pp. 071122-1–071122-3,.

Tang, Y. (2004) "*Accuracy analysis and improvement for direct laser sintering*", *Proc. SMA Annu. Symp.*, 2004.

Texas Instruments Inc. (2005) "*How DLP Technology Works*" [Online]. Available from [http://www.dlp.com/dlp\\_technology/dlp\\_technology\\_overview.asp](http://www.dlp.com/dlp_technology/dlp_technology_overview.asp). [Accessed: 3/Feb/2012],

Varadan, V., Kalarickaparambil, J., and Jose, K. (2003) "*RF MEMS and their applications*" John Wiley, ISBN 0-470-84308-X, England.

Vatani, M., Barazandeh, F., Rahimi, A., and Nezhad, A. (2012) "*Distortion Modelling of SL Parts by Classical lamination Theory*", *Rapid Prototyping Journal* Volume 18 . Number 3 . 2012 . pp. 36-49.

Venuvindo, P., and Weiyin, Ma. (2004), *Rapid Prototyping-Laser based and other technologies*, Kluwer Academic Publisher, New York.

Wan Yusoff. (2007) “*An investigation of the "orange peel" phenomenon*” PhD thesis at Cardiff University.

Wang, W., Cheah, C., Fuh, J., and Lu, L. (1997) “*Influence of process parameters on stereolithography part shrinkage*” *Materials & Design*. Vol. 17, No. 4, pp. 205-213.

Wohlers, T. (2005) *Wohlers Report (2005)* Wohlers Associates, Fort Collins, CO.

Wohlers, T. (2008) *Wohlers Report (2008)* Wohlers Associates, Fort Collins, CO.

Wu, S., Serbin, J., Gu, M. (2006) “*Two-photon polymerisation for three-dimensional Microfabrication*”, *Journal of Photochemistry and Photobiology A: Chemistry*, 191, 1-11.

Yang, H., Tsiklos, G., Ronaldo, R., Ratchev, S., (2008) *Micro-Assembly Technologies and Applications* IFIP, Volume 260, , eds. Ratchev, S., Koelemeijer, S., (Boston: Springer), pp. 171-176.”

Yan, M, P. Gu, X. Huang and X. Zhang,(1996) “*Analysis of machine accuracy for rapid prototyping of quality components*”, *Proceedings-of-SPIE, The-International-Society-for-Optical-Engineering*, V3517, pp 91-101

Z Corporation. (2012) *Spectrum Z510* [Online]. Available from <http://www.zcorp.com/en/Products/3D-Printers/spage.aspx> [Accessed: 8/Feb/2012]

Zissi, et al (1996) "*Stereolithography and microtechniques*", Microsystem Technologies, Vol. 2 No.2, pp.97-102.

Zizalo, J. (2008) "*Masked Projection Stereolithography: Improvement of the Limaye Model for Curing Single Layer Medium Sized Parts*" PhD thesis Massey University, New Zealand.

Zhou, J., Herscovici, D., and Chen, C. (2001) "*Parametric Process Optimization to Improve the Accuracy of Rapid Prototyping Stereolithography Parts*" International Journal of Machine Tools and Manufacture, No.40, 1-17.

Zhou, C., Chen, Y., and Waltz, R. (2009) "*Optimized Mask Image Projection for Solid Freeform Fabrication*" Proc. ASME 2009 International Design Engineering Technical Conferences & Computers and Information in Engineering Conference San Diego, California, USA

3d Systems (2012) [Online]. Available from  
[http://www.3dsystems.com/products/datafiles/sinterstation\\_hiq/datasheets/DS\\_Sinterstation\\_HiQ\\_rev0606.pdf](http://www.3dsystems.com/products/datafiles/sinterstation_hiq/datasheets/DS_Sinterstation_HiQ_rev0606.pdf) [Accessed: 2/Feb/2012]